

Simulation of the global beam line alignment of the KATRIN experiment

Masterarbeit
von

Marco Deffert

am Institut für Experimentelle Kernphysik

Referent:	Prof. Dr. Guido Drexlin
Korreferent:	Prof. Dr. Ulrich Husemann
Betreuender Mitarbeiter:	Dr. Fabian Harms

Bearbeitungszeit: 02.05.2016 – 28.04.2017

Erklärung zur Selbstständigkeit

Ich versichere, dass ich diese Arbeit selbstständig verfasst habe und keine anderen als die angegebenen Quellen und Hilfsmittel benutzt habe, die wörtlich oder inhaltlich übernommenen Stellen als solche kenntlich gemacht und die Satzung des KIT zur Sicherung guter wissenschaftlicher Praxis in der gültigen Fassung vom 17.05.2010 beachtet habe.

Karlsruhe, den 28.04.2017, _____
Marco Deffert

Als Ansichtsexemplar genehmigt von

Karlsruhe, den 28.04.2017, _____
Prof. Dr. Guido Drexlin

Contents

1. Introduction	1
2. Neutrino Physics	3
2.1. History of Neutrino Physics	3
2.2. Neutrino Oscillations	4
2.2.1. Historical Experiments	4
2.2.2. Theory of Neutrino Oscillation	6
2.2.3. Measurement of Neutrino Oscillation Parameters	6
2.3. Neutrino Sources	6
2.4. Measurement of the Neutrino Mass	9
2.4.1. Cosmology	9
2.4.2. Supernovae	10
2.4.3. Neutrinoless Double Beta Decay	10
2.4.4. Single Beta Decay	10
3. The KATRIN Experiment	13
3.1. Measurement Principle	13
3.2. Components of the KATRIN Experiment	14
3.2.1. Rear Section	14
3.2.2. Windowless Gaseous Tritium Source	15
3.2.3. Differential Pumping Section	16
3.2.4. Cryogenic Pumping Section	16
3.2.5. Pre-Spectrometer	17
3.2.6. Main Spectrometer	17
3.2.7. Focal Plane Detector	18
3.2.8. Monitor Spectrometer	20
4. Simulations with Kassiopeia	21
4.1. Kassiopeia	21
4.2. Implementation of the Global KATRIN Beamline into Kassiopeia	22
4.2.1. Alignment Implementations	22
4.2.2. Global Geometry	23
4.2.3. Access to Alignment Data	28
4.2.4. Ongoing and Future Work	31
5. Preparatory Alignment Measurements	33
5.1. Mechanical Beamline Alignment	33
5.1.1. FaroArm and Laser Tracker Measurements	33
5.1.2. Magnetic Field Measurements	34
5.1.3. WGTS Beamtube Alignment	35
5.2. FPD Alignment	36

5.3.	MS-FPD Alignment	37
5.3.1.	MS-FPD Alignment Measurement	37
5.3.2.	MS-FPD Alignment Simulations	39
5.4.	PS-FPD Alignment	42
5.4.1.	PS-FPD Alignment Measurement	42
5.4.2.	PS-FPD Alignment Simulations	43
5.5.	Discussion of Uncertainties	45
6.	Global Beamline Alignment	47
6.1.	First Light Measurement Campaign	47
6.1.1.	Rear Wall Illumination	47
6.1.2.	Eliott as an e-Gun	49
6.1.3.	Dipole coils	51
6.2.	Global Alignment	54
6.2.1.	RS-FPD Alignment	54
6.2.2.	RS-WGTS Alignment	54
6.2.3.	WGTS-FPD Alignment	55
6.2.4.	WGTS alignment simulations	55
6.3.	Low-Energy Blocking	56
7.	Summary and Outlook	59
	Appendix	61
A.	Pinch Magnet Field Measurements	61
	Bibliography	67

List of Figures

2.1.	Energy spectrum of β -electrons from decay of radium E	4
2.2.	Results of the Super Kamiokande experiment	5
2.3.	Energy spectrum of solar neutrinos	8
2.4.	Normal and inverted neutrino mass hierarchy	9
2.5.	Electron energy spectrum of neutrinoless double beta decay	11
2.6.	Electron energy spectrum from tritium decay	11
3.1.	The MAC-E filter principle	14
3.2.	The KATRIN experimental beamline	15
3.3.	The windowless gaseous tritium source	15
3.4.	Geometry of the differential pumping section	16
3.5.	Geometry of the cryogenic pumping section	17
3.6.	Geometry of the pre-spectrometer	18
3.7.	The detector wafer	19
3.8.	Overview of the Focal-Plane Detector system	19
4.1.	WGTS geometry as implemented in Kassiopeia	23
4.2.	Visualization of the dipole coils with the MeshViewer	24
4.3.	DPS geometry as implemented in Kassiopeia	25
4.4.	Geometry of the DPS pump ports in the MashViewer.	25
4.5.	Geometry of the DPS dipole electrodes	26
4.6.	CPS geometry as implemented in Kassiopeia	26
4.7.	PS geometry as implemented in Kassiopeia	27
4.8.	Geometry of the ILBV flapper	27
4.9.	Geometry of the new PS ILBV as implemented in Kassiopeia	28
4.10.	MS geometry as implemented in Kassiopeia	29
4.11.	FPD geometry as implemented in Kassiopeia	29
4.12.	Access to alignment data	30
5.1.	Hall probe on rotatable PVC disk	35
5.2.	Exemplary sine fit to pinch magnet alignment data	35
5.3.	WGTS beamtube alignment data for the x-direction	36
5.4.	WGTS beamtube alignment data for the y-direction	36
5.5.	Pixel view of the FPD alignment measurement with the americium source	38
5.6.	Analysis of the FPD alignment measurement with the americium source	38
5.7.	Magnetic field configuration as used in the MS-FPD-alignment measurements	39
5.8.	Pixel view of the MS-FPD-alignment	40
5.9.	Pixel view of the MS-FPD alignment simulation	41
5.10.	MS-FPD-alignment simulation analysis after correction of the wafer position	41
5.11.	Magnetic field configuration as used in the PS-FPD-alignment measurements	42
5.12.	Pixel view of the PS-FPD alignment	43
5.13.	Ring fits for the measurement of the PS-FPD-alignment	44
5.14.	PS-FPD-alignment simulation	44

6.1. Measurement of electrons from rear wall illumination	48
6.2. Pixel view for the simulation of electrons genetated on the rear	48
6.3. Final z-positions from rear wall illumination simulation	49
6.4. Measurement of the electron pencil beam from ELIOTT	50
6.5. Pixel view of the simulated pencil beam from ELIOTT	51
6.6. Simulated fieldlines of shifted electron beam from pin hole	52
6.7. Analysis of the shift of the pencil beam with dipole coil in x-direction . . .	53
6.8. Analysis of the shift of the pencil beam with dipole coil in y-direction . . .	53
6.9. Field lines inside the WGTS	55
6.10. Pixel view with low energy electrons from UV illumination	56

List of Tables

2.1. Experimental results for neutrino oscillation parameters	7
5.1. Results of FaroArm and Laser Tracker measurements	34
5.2. WGTS beamtube alignment	37
5.3. MS-FPD-alignment results	40
5.4. PS-FPD alignment results	45
6.1. Increasing count rates after ramping up CPS and DPS magnets	49
6.2. Analysis of pencil beam movement	54
A.1. Pinch Magnet: 0 T; Detector Magnet: 1.8 T; upstream	62
A.2. Pinch Magnet: 0 T; Detector Magnet: 1.8 T; downstream	62
A.3. Pinch Magnet: 3 T; Detector Magnet: 1.8 T; upstream	63
A.4. Pinch Magnet: 3 T; Detector Magnet: 1.8 T; downstream	63
A.5. Pinch Magnet: 3 T; Detector Magnet: 0 T; upstream	64
A.6. Pinch Magnet: 3 T; Detector Magnet: 0 T; downstream	64
A.7. Pinch Magnet: 0 T; Detector Magnet: 0 T; upstream	65
A.8. Pinch Magnet: 0 T; Detector Magnet: 0 T; downstream	65

1. Introduction

Neutrinos play an important role in several subsections of physics. Even though they were postulated as early as in 1930 and first observed in 1956, some properties of these ghost-like particles like for example their mass are still unknown. With the groundbreaking findings of neutrino oscillation experiments like Super-Kamiokande or SNO in the late 90's and early 2000's it is proven that neutrinos must have a non-zero rest mass. Due to their large natural abundance and their weak interaction with matter they play an important role in the structure formation in the early universe. In the last decades several experiments tried to measure the neutrino mass, most of which highly relied on the underlying model. Nevertheless, up until today only upper limits could be stated on the neutrino mass. The basics of neutrino physics, the theory of neutrino oscillation and important historical and modern experiments will be introduced in chapter 2.

The model independent Karlsruhe TRitium Neutrino (KATRIN) experiment aims to exceed its predecessor experiments by one order of magnitude by measuring the effective mass of the electron anti-neutrino $\bar{\nu}_e$ with a sensitivity of

$$m_{\bar{\nu}_e} = 0.2 \text{ eV}/c^2 \text{ (90 \% C.L.)}. \quad (1.1)$$

To reach this ambitious goal the KATRIN experiment will measure the energy spectrum of β electrons from tritium decay near the endpoint energy of $E_0 = 18.6 \text{ keV}$ where a non-zero neutrino mass influences the shape of the spectrum. Electrons from the tritium β decay are guided adiabatically by a magnetic field from a windowless source to two electrostatic spectrometers, where their energy is analyzed. To reach its goals in terms of sensitivity the KATRIN experiment must combine a high luminosity β^- source with a very good energy resolution. For this purpose it uses spectrometers based on the well-established MAC-E filter principle. The measurement principle and the main components of the KATRIN experiment will be described in chapter 3.

For this thesis the geometry of the full KATRIN beamline was implemented within the simulation software framework Kassiopeia which will be introduced in chapter 4. With this model it is possible to perform simulations with the full beamline for the first time. This allows for studies of the fluxtube from the source to detector. To form the model as accurate as possible the alignment of all components was measured with different methods that will be presented in chapter 5 and the results were included into the Kassiopeia geometry.

In Oktober 2016 the installation of the KATRIN experimental beamline at the Karlsruhe Institute of Technology got finished. On Oktober 14th 2016 the experiment celebrated its First Light event where the first electrons were guided through the full 70 m long beamline. This First Light event was followed by the First Light measurement campaign including among others detailed alignment measurements with the global KATRIN beamline.

In this thesis the detailed geometry model in Kassiopeia is used to compare simulations on the beamline alignment to data gained during the First Light campaign, as shown in chapter 6.

2. Neutrino Physics

Neutrinos are elementary particles first detected in 1956 but to this day the mass of the neutrinos remains unknown. Various current experiments aim to determine the mass of the neutrinos since it has a big influence e.g. on the structure formation in the early universe and therefor on theories in cosmology.

In this chapter fundamentals of neutrino physics will be described from historical experiments in section 2.1 to modern theories like neutrino oscillation (section 2.2) and up-to-date experimental concepts (section 2.4). In section 2.3 important neutrino sources for previous and current experiments are highlighted.

2.1. History of Neutrino Physics

As early as in 1930 Wolfgang Pauli wrote his famous letter to the “radioactive ladies and gentlemen” where he postulated the existence of a “neutron” to explain the continuous electron energy spectrum of the beta decay [Pau30]. The latter was measured for the first time by James Chadwick in 1914 when he investigated the beta decay of radium [Cha14] which is shown in figure 2.1. Without the postulated “neutron” the beta decay of a nucleus ${}^A_Z X$ into a nucleus ${}^A_{Z+1} Y$ would result in a constant energy of the emitted electron. If there was an additional electrically neutral particle with little mass and spin- $\frac{1}{2}$ emitted in the beta decay sharing the decay energy with the electron, the continuous spectrum of the electron would be explained.

Since the name “neutron” had been established for the baryon, the neutral particle postulated by Pauli was now called neutrino, what means *the little neutral one* with the Italian diminutive. In 1934 Enrico Fermi formulated a coherent theory for a weak point-like decay of a neutron into a proton, an electron and a neutrino [Fer34].

Pauli called his theory a “desperate resort” [Pau30] but in the year 1956 the neutrino was detected by Clyde L. Cowan and Frederick Reines [Cow56]. By using a nuclear reactor as a source of anti electron neutrinos $\bar{\nu}_e$, they were able to detect inverse beta decays of protons p in water



The positron e^+ annihilates with an electron emitting two photons, and the neutron n gets absorbed by ${}^{108}\text{Cd}$ dissolved in the water emitting another photon. The photons could be detected by photo multiplier tubes in a coincidence measurement. For this discovery Reines was honored with the Nobel Prize in 1995.

In the year 1962 Leon Max Lederman, Melvin Schwartz and Jack Steinberger discovered a second type of neutrinos, the muon neutrino ν_μ [Dan62]. Protons accelerated with the Alternating Gradient Synchrotron (AGS) were shot on a beryllium target. They thereby generated pions decay as



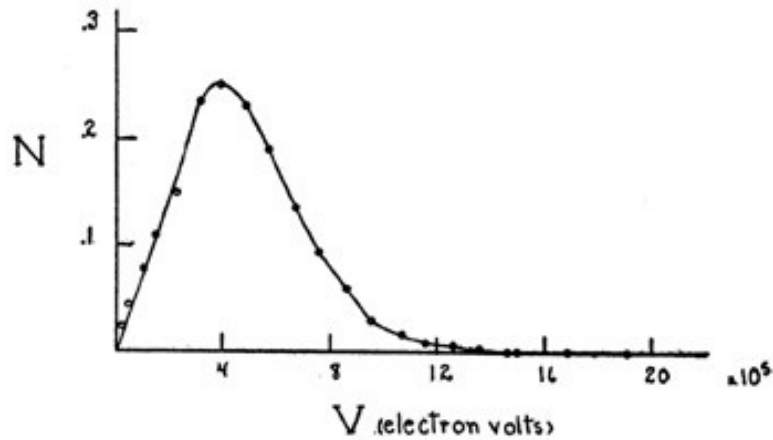


Figure 2.1.: Energy spectrum of β -electrons from decay of radium E. Figure adapted from [Sco35]

The neutrinos from π^+ decays can interact with a neutron in matter by neutrino induced beta decay

$$\nu_{\mu} + n \rightarrow \mu^{-} + p . \quad (2.3)$$

The muons were discriminated from electrons or positrons in an aluminum spark chamber, where a muon signal was a straight line and e^+ and e^- developed showers. Lederman, Schwartz and Steinberger received the Nobel Prize in 1988.

After the discovery of the third generation lepton, the tau lepton τ in 1975 [Per75] the existence of a third generation neutrino was expected. However it took 26 years until in the year 2001 the tau neutrino ν_{τ} could be discovered. By interactions of high-energy protons from Tevatron with a tungsten target amongst others D_s mesons were produced which decayed into a tau lepton and a tau neutrino. In the DONOT¹ detector, composed by alternating layers of stainless steel and emulsion plates, the tau leptons could be discriminated by their decay after a short distance which caused a kink in the particle trajectory [DON01].

2.2. Neutrino Oscillations

The measurement of neutrino oscillations was the first proof of a non-zero neutrino mass. In this section historical and modern experiments will be described and the theory of neutrino oscillations will be introduced.

2.2.1. Historical Experiments

In 1970 the Homestake experiment headed by Ray Davis, Jr. [Dav64, DHH68] started its measurements of the solar neutrino flux to confirm the standard solar model established by John Bahcall [Bah64a] [Bah64b]. In the experiment located in the Homestake mine in South Dakota 615 tons of tetrachloroethylene C_2Cl_4 were used as a target for solar neutrino interactions. Argon atoms created in a neutrino induced beta decay of chlorine atoms

$$\nu_e + {}^{37}\text{Cl} \rightarrow e^{-} + {}^{37}\text{Ar} \quad (2.4)$$

could be counted in a radiochemical process. The measurement results displayed only a quarter to a third of the expected rate calculated in the standard solar model [BD76, DEC79]. This anomaly was from then on called the ‘‘Solar Neutrino Problem’’.

¹Direct Observation of the NU Tau

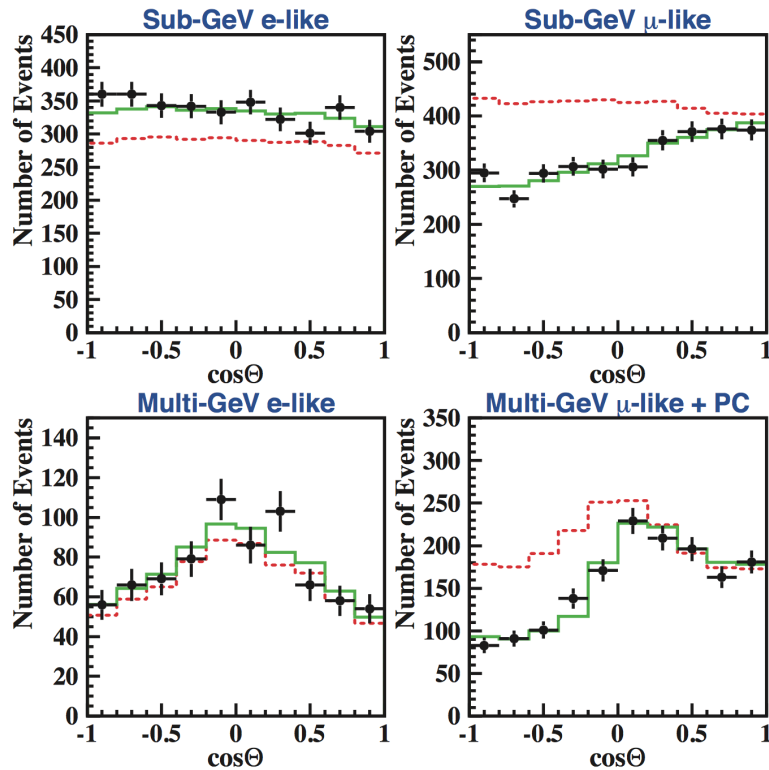


Figure 2.2.: Results of the Super Kamiokande experiment for e-like (left) and μ -like neutrinos (right). Up-going muon neutrinos show a lack of events for energies in the Sub-GeV and Multi-GeV range compared to simulations (red dashed line). But calculations with a neutrino oscillation (green solid line) fit the data well (see also section 2.2.2). Figure adapted from [Oli14].

This “Solar Neutrino Problem” could be solved in 2001 by the Sudbury Neutrino Observatory (SNO) in Canada headed by Arthur McDonald [Zub11]. The experiment used 1 000 tons of heavy water (D_2O) surrounded by 9 600 PMTs. The advantage of heavy water is the possibility to detect incoming neutrinos via charged current (CC) and neutral current (NC) reactions:

$$\begin{aligned} \text{CC} : \quad \nu_e + D &\rightarrow p + p + e^- \\ \text{NC} : \quad \nu_\alpha + D &\rightarrow p + n + \nu_\alpha \end{aligned} \tag{2.5}$$

with $\alpha \in [e; \mu; \tau]$. The charged current reaction is only allowed for electron neutrinos due to the limited energy of solar neutrinos and the higher mass of μ and τ leptons, whereas the NC takes place for all neutrino flavors.

The results of SNO showed that the total neutrino flux is consistent with the calculated flux from the standard solar model. The flux of electron neutrinos detected in CC reactions, however, was found to be only about a third of the expected flux [Ahm02].

Another case with a lack of one neutrino flavor was observed by the Super-Kamiokande experiment located near Kamioka in Japan [Fuk96, Fuk98]. The neutrino observatory detected neutrinos with a tank filled with 50 000 tons of ultra-pure water surrounded by 11 146 photo multiplier tubes (PMT). Neutrinos that interact with the water produce a high-energy lepton that causes Cherenkov radiation due to its velocity being larger than the speed of light in matter. The results that can be seen in figure 2.2 showed that there is a lack of up-going muon neutrinos compared to down-going ones and to Monte Carlo simulations of almost 50 percent.

The lack of neutrinos in the Homestake and Super-Kamiokande experiment as well as in

the CC reaction at SNO can be explained by neutrino flavour oscillations [Zub11].

2.2.2. Theory of Neutrino Oscillation

The first theory of neutrino oscillation was introduced in 1957 by Bruno Pontecorvo [Pon57a] [Pon57b]. Further developments were done by Ziro Maki, Masami Nakagawa and Shoichi Sakata [MNS62] and Pontecorvo in 1967 [Pon67].

The flavor eigenstates $|\nu_\alpha\rangle$ with $\alpha \in [e; \mu; \tau]$ are eigenstates of the weak interaction and can be described by superposition of mass eigenstates $|\nu_i\rangle$ with $i \in [1; 2; 3]$ with masses m_i connected through

$$|\nu_\alpha\rangle = \sum_i U_{\alpha i} |\nu_i\rangle \quad \text{and} \quad |\nu_i\rangle = \sum_\alpha U_{\alpha i}^* |\nu_\alpha\rangle \quad (2.6)$$

where U is the unitary mixing matrix

$$U = \begin{pmatrix} c_{12}c_{13} & s_{12}c_{13} & s_{13}e^{-i\delta} \\ -s_{12}c_{23} - c_{12}s_{23}s_{13}e^{i\delta} & c_{12}c_{23} - s_{12}s_{23}s_{13}e^{i\delta} & s_{23}c_{13} \\ s_{12}s_{23} - c_{12}c_{23}s_{13}e^{i\delta} & -c_{12}s_{23} - s_{12}c_{23}s_{13}e^{i\delta} & c_{23}c_{13} \end{pmatrix} \cdot \begin{pmatrix} 1 & 0 & 0 \\ 0 & e^{\frac{i\alpha_{21}}{2}} & 0 \\ 0 & 0 & e^{\frac{i\alpha_{31}}{2}} \end{pmatrix} \quad (2.7)$$

with $s_{ij} = \sin(\theta_{ij})$, $c_{ij} = \cos(\theta_{ij})$, the weak mixing angles θ_{ij} , the Dirac CP violation phase $\delta = [0, 2\pi]$, and two Majorana CP violation phases α_{21} and α_{31} . U is called PMNS matrix named after the developers of the neutrino oscillation theory Pontecorvo, Maki, Nakagawa and Sakata.

Neutrino oscillation is only possible if at least two of three neutrino mass eigenstates have a mass. The transition probability for a two state oscillation is

$$P(\nu_e \rightarrow \nu_\mu) \approx \sin^2(2\theta_{12}) \cdot \sin^2\left(\frac{\Delta m_{12}^2 L c^3}{4\hbar E}\right) \quad (2.8)$$

with the difference of the squared masses $\Delta m_{12}^2 = m_1^2 - m_2^2$, the baseline length L and the neutrino energy E .

For the discovery of neutrino oscillations and the indirect evidence for a non-zero neutrino rest mass, Takaaki Kajita of the Kamiokande collaboration and Arthur McDonald of the SNO collaboration were honored with the Nobel Prize in physics in 2015.

2.2.3. Measurement of Neutrino Oscillation Parameters

The parameters that describe the neutrino oscillation are the mass differences Δm_{ij}^2 and the mixing angles Θ_{ij} . Various experiments investigated neutrino oscillation parameters in the last years. Amongst others, scintillator experiments like Daya Bay [An 13], Double Chooz [Abe12] and RENO [Ahn12] measured the mixing angle Θ_{13} with reactor neutrinos, the water-cherencov experiment Super-Kamiokande [Fuk01] measured Θ_{23} and Δm_{23} and KamLAND [Abe08] Θ_{12} and Δm_{12} . Current values for the measured parameters are listed in table 2.1.

2.3. Neutrino Sources

Several sources are available for neutrino research. Some have a natural origin and can also give information about the source, others are man-made.

Table 2.1.: Experimental results for neutrino oscillation parameters [Pat16]

parameter	result
$\sin^2(\theta_{12})$	$0.304^{+0.014}_{-0.013}$
$\sin^2(2\theta_{23})$	0.50 ± 0.05 (inverted mass hierarchy) 0.51 ± 0.05 (normal mass hierarchy)
$\sin^2(2\theta_{13})$	$(2.19 \pm 0.12) \cdot 10^{-2}$
Δm_{21}^2	$7.53 \pm 0.18 \cdot 10^{-5} \text{eV}^2$
Δm_{32}^2	$(2.51 \pm 0.06) \cdot 10^{-3} \text{eV}^2$ (inverted mass hierarchy) $(2.44 \pm 0.06) \cdot 10^{-3} \text{eV}^2$ (normal mass hierarchy)

Cosmic Neutrino Background

The cosmic neutrino background (CνB) is a relic of the freeze-out of the weak interaction in the early universe [Sli15, Lun24, HH31, LP12]. Their properties offer valuable clues to the development of the universe from the radiation dominated era over the matter dominated era to now, the era of dark energy (Λ) [Lid03, BG06], i.e. it can also give a hint to the properties of dark matter.

In the first split second ($t \ll 0.01 \text{ s}$) after the Big Bang at high temperatures ($T \gg 1 \text{ MeV}$) the universe was dominated by radiation with all particles in a thermodynamic equilibrium. Neutrinos could be created and destroyed in weak interaction processes such as

$$\nu_l + \bar{\nu}_l \leftrightarrow l^+ + l^- \quad (2.9)$$

where $l \in [e; \mu; \tau]$ stands for a lepton.

When the universe expanded its temperature decreased ($T \approx 1 \text{ MeV}$) and the energy became too low to keep the only weakly interacting neutrinos in an equilibrium. The neutrinos froze-out. Due to the expansion of the universe after the freeze-out the neutrino energy kept falling to its today's theoretical value of $T_\nu \approx 1.95 \text{ K}$.

Supernova Neutrinos

Supernovae are astrophysical events that occur in the end phase of a massive star's evolution. Several types of supernova explosions are differentiated by the light curves and spectral analysis.

Core collapse supernovae are of importance for neutrino physics. In its later life the fusion processes in a massive star with $M > 8 \cdot M_\odot$ have burnt the hydrogen and helium atoms to heavier elements. In the final fusion state silicon in the core is fused to iron, cobalt and nickel, elements with the highest binding energies. Since these elements can not be fused to heavier elements, the thermonuclear reactions stop. When the mass of the core reaches the Chandrasekhar mass $M_{\text{Ch}} \approx 1.44 \cdot M_\odot$ the radiation pressure loses to the gravitation pressure and the core collapses leading to a neutron star or a black hole depending on the mass. During the collapse neutrinos are generated by neutronization

$$p + e^- \rightarrow n + \nu_e \quad (2.10)$$

and can escape the core [WJ05, Jan07]. Up to 10^{58} neutrinos with a mean energy of $\langle E_\nu \rangle = (10 - 15) \text{ MeV}$ carry 99 % of the energy released during that collapse [BDP87].

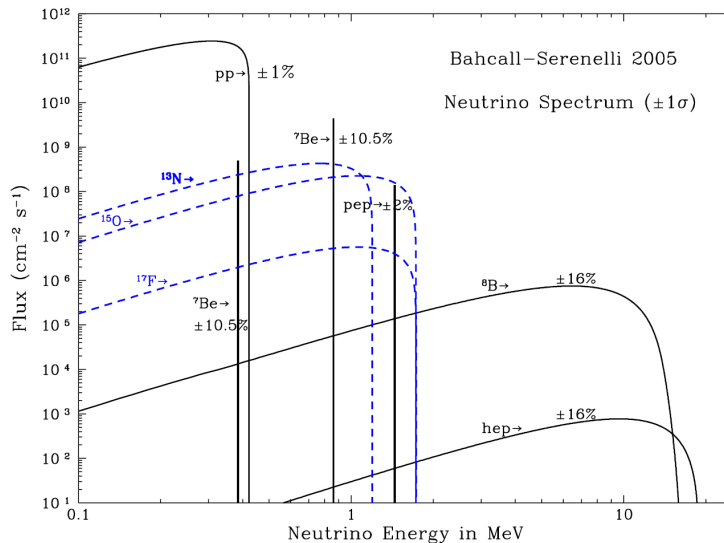
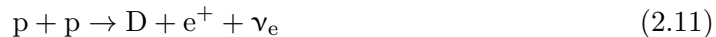


Figure 2.3.: Energy spectrum of solar neutrinos calculated from the standard solar model. Figure adapted from [Bah05].

Solar Neutrinos

Due to the high neutrino production rate and its close distance the sun represents the strongest natural neutrino source for experiments on earth. In the sun neutrinos are generated in several reactions such as proton-proton fusion



or the so called carbon-nitrogen-oxygen (CNO) cycle. The energy spectrum of solar neutrinos as calculated from the standard solar model is given in figure 2.3. Solar neutrinos are ideal messenger particles to study processes inside the sun. By investigating the flux of solar neutrinos, the SNO experiment could in this way confirm the standard solar model as described in section 2.2.3.

Atmospheric Neutrinos

Earth's atmosphere gets permanently hit by high-energy particles, mostly protons, from space. Interactions of these particles within the atmosphere lead to particle showers consisting of elementary particles like electrons, positrons, muons or photons, but also of composite particles like pions or kaons.

Pions and kaons in the atmosphere decay into muons and muon neutrinos, cf. equation 2.2. Since the muon subsequently decays into a muon neutrino ν_μ , an electron e^- and an electron neutrino ν_e , the $\frac{\nu_\mu}{\nu_e}$ ratio of atmospheric neutrinos is $\frac{2}{1}$.

Reactor Neutrinos

In nuclear reactors besides the heat used to produce electric current, the nuclear fission of isotopes like $^{233}_{92}\text{U}$, $^{235}_{92}\text{U}$, $^{239}_{94}\text{Pu}$ or $^{241}_{94}\text{Pu}$ always produces neutrinos. With an average of about six neutrinos per fission a typical nuclear power plant produces 10^{21} neutrinos per second with a maximum neutrino energy of 10 MeV. That makes nuclear power plants the strongest non-natural source of neutrinos on earth.

artificial neutrino source with the highest flux. Reactor neutrinos are used to investigate neutrino oscillations as described in section 2.2.3.

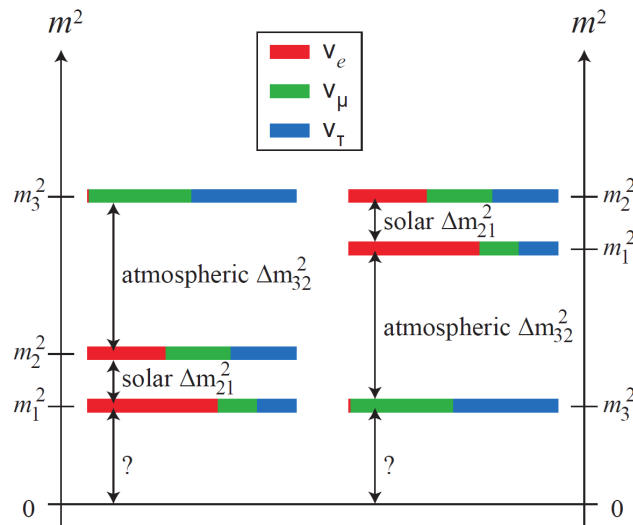


Figure 2.4.: The normal (left) and the inverted (right) neutrino mass hierarchy. Figure adapted from [KL13].

Accelerator Neutrinos

To create neutrinos it is possible to shoot protons from a particle accelerator on a fixed target usually made of graphite or beryllium. In the target material among others pions and kaons are produced that are guided into a tunnel where they decay whereat neutrinos accrue. The muons from the decay can be shielded by a block of concrete or steel as the neutrinos can fly through. The neutrino beam with GeV-scale energies can be sent to detectors in a distance of up to hundreds of kilometers to analyze their oscillation behavior (see section 2.2.3) [Kop07].

2.4. Measurement of the Neutrino Mass

Neutrino oscillation measurements as described in section 2.2.3 only allow conclusions on differences of squared neutrino masses Δm_{ij}^2 , but not on the absolute neutrino mass or on the hierarchy of the mass eigenstates. Figure 2.4 shows a normal and an inverted hierarchy of the three neutrino mass eigenstates, which are both in accordance with the findings from the oscillation experiments.

In the following possible experimental approaches to determine the absolute mass of the neutrinos and/or assess the correct mass hierarchy are discussed.

2.4.1. Cosmology

Analyses of the cosmic microwave background (CMB) give information about the early universe. Before the CMB-Photons have decoupled from matter about 380,000 years after the Big Bang, the universe was in thermal equilibrium. Due to the expansion of the universe the temperature decreased and the CMB was emitted with a nearly ideal black-body spectrum.

Experiments like WMAP (Wilkinson Microwave Anisotropy Probe) [HLK13] or Planck [AAA16a] have measured the CMB with high precision and discovered temperature fluctuations in a scale of $\frac{\Delta T}{T} = 2 \cdot 10^{-6}$. The shape of the power spectrum of the cosmic microwave background radiation temperature anisotropy in terms of the angular scale is a strong evidence for dark matter and dark energy. Furthermore parameters like the Hubble

constant $H_0 = (67.8 \pm 0.9) \frac{\text{km}}{\text{s}\cdot\text{Mpc}}$, the number of neutrino generations $N_\nu = 3.15 \pm 0.23$ or the the sum of the neutrino masses

$$\sum m_\nu < 0.23 \text{ eV} \quad (2.12)$$

could be determined [AAA16b]. However, these values strongly depend on the cosmological model used.

2.4.2. Supernovae

Measuring the time-of-flight T of neutrinos from supernovae allows to determine the neutrino mass M_ν . For a distance L to the supernova it holds

$$T = \frac{L}{v} = \frac{L}{c} \cdot \frac{E_\nu}{p_\nu c} = \frac{L}{c} \cdot \frac{E_\nu}{\sqrt{E_\nu^2 - m_\nu^2 c^4}} \approx \frac{L}{c} \left(1 + \frac{m_\nu^2 c^4}{2E_\nu^2} \right), \quad (2.13)$$

with $m_\nu c^2 \ll E_\nu$ [Zub11].

Up to now only one supernova explosion could be detected in terms of a neutrino signal. Within 13 seconds, the water Cherenkov experiments IMB [Bio87] and Kamiokande [Hir88] measured 19 neutrinos from the type II supernova SN1987A in February 1987, what was the first direct observation in neutrino astronomy.

The analysis of the data set an upper limit to the neutrino mass of [LL02]

$$m_\nu < 5.7 \text{ eV} \quad (90 \% \text{ C.L.}). \quad (2.14)$$

This value is dependent on the underlying model for supernovae emission profile.

2.4.3. Neutrinoless Double Beta Decay

The neutrinoless double beta ($0\nu\beta\beta$) decay is a hypothetical simultaneous decay of two neutrons of one nucleus into two protons and two electrons without emitting neutrinos. This decay is only possible if the neutrino is not a Dirac like particle as in the standard model of particle physics but a Majorana like particle which means that it is its own anti-particle [DKT85]. The energy spectrum of the ordinary double beta decay with two emitted neutrinos ($2\nu\beta\beta$) and the neutrinoless decay ($0\nu\beta\beta$) is shown in figure 2.5.

The discovery of the $0\nu\beta\beta$ decay would also give information about the effective Majorana mass

$$m_{ee} = \left| \sum_{i=1}^3 U_{ei}^2 m_i \right| = \left| \sum_{i=1}^3 |U_{ei}|^2 e^{i\alpha_{i1}} m_i \right| \quad (2.15)$$

of the neutrino [EV02]. One example for various experiments is the GERDA experiment that investigated the decay ${}^{76}\text{Ge} \rightarrow {}^{76}\text{Se} + 2e^-$ and set an upper limit on the Majorana mass of $m_{\beta\beta} < (0.15 - 0.33) \text{ eV}$ (90% C.L.) [AAB17].

2.4.4. Single Beta Decay

To measure the neutrino mass from single β -decay two different types of experiments are dominating the field: Experiments using cryogenic bolometers and experiments using electrostatic spectrometers like in the KATRIN experiment.

The former mainly use ${}^{187}\text{Re}$ as β -source placed inside the detector such that the entire decay energy except the neutrino energy can be measured [Giu12]. With the lowest known endpoint energy of $E_0 = 2.47 \text{ keV}$ ${}^{187}\text{Re}$ has the advantage of a ... Examples for ${}^{187}\text{Re}$ -based experiments are MANU [Gat99] in Genoa, MiBeta [Sis04] in Milano, and MARE [Nuc08].

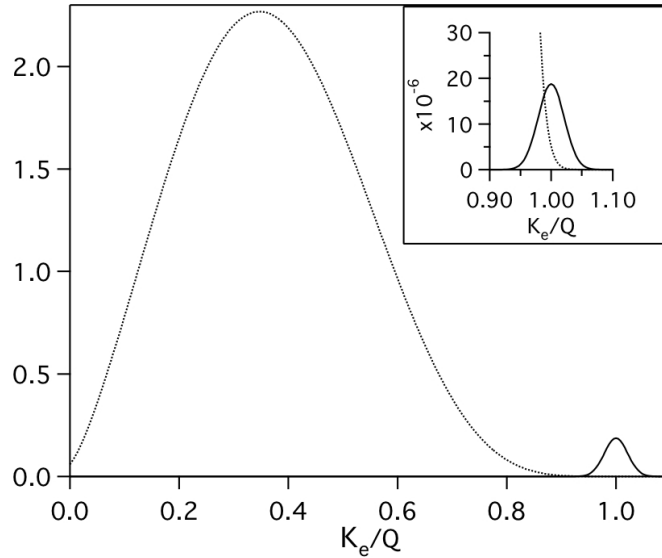


Figure 2.5.: Electron energy spectrum of neutrinoless double beta decay ($0\nu\beta\beta$). The dominant peak originates from the ordinary double beta decay ($2\nu\beta\beta$) emitting two neutrinos. The small peak at higher K_e/Q , which is shown magnified, comes from the $0\nu\beta\beta$ decay. Figure adapted from [EV02].

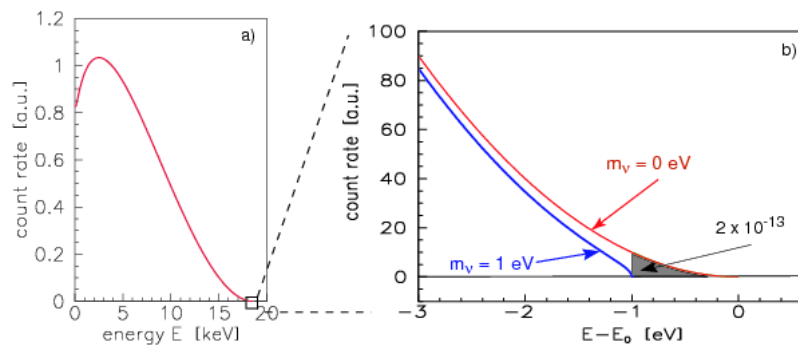


Figure 2.6.: Electron energy spectrum from tritium decay. Figure adapted from [Osi01].

In the last few years also the electron capture process in of holmium ^{163}Ho got into interest for low temperature calorimetry. Experiments like HOLMES [Gal12] and ECHO [Gas14] aim to achieve a sensitivity of a few eV on the neutrino mass.

Tritium experiments use the β -decay of tritium



to investigate the neutrino mass. Tritium has a half life of $\tau_{1/2} = (12.33 \pm 0.06)$ years and a Q -value of $Q = (18.591 \pm 0.001)$ keV what is the second lowest value known for β^- decay.

The energy spectrum has an end if neutrinos have a mass as shown in figure 2.6, since the β -decay releases a specific energy that is split among the kinetic and the mass energy of electron and antineutrino. Thus the electron energy gets its maximum energy if the antineutrino is produced at rest.

3. The KATRIN Experiment

The Karlsruhe Tritium Neutrino (KATRIN) experiment located at the Campus North of the Karlsruhe Institute of Technology (KIT), aims to determine the effective mass of the electron antineutrino $\bar{\nu}_e$ with a sensitivity of $m_\nu = 0.2 \text{ eV}$ (90 % C.L.) by investigating the kinematics of tritium β -decay [Ang05] [Dre13].

This chapter will give an overview of the KATRIN experiment. In section 3.1 the measurement principle is explained while section 3.2 gives an overview of the experiment's beamline including all main components.

3.1. Measurement Principle

To determine the neutrino mass, the KATRIN experiment will measure the total energy of β -electrons from tritium decay. As described in section 2.4.4, the endpoint of the energy spectrum ($E_0 = 18.6 \text{ keV}$) is investigated. To combine a high luminosity of the source with a very good energy resolution, electrons with lower energy, that are produced at much higher rates, have to be filtered out. For that purpose the KATRIN Main Spectrometer is designed as a MAC-E filter.

A MAC-E filter (Magnetic Adiabatic Collimation with an Electrostatic Filter) is a type of spectrometer that was first proposed by Kruit and Read in 1983 [KR83] basing on former works of Beamson, Porter and Turner [BPT80]. Figure 3.1 shows the working principle of such a filter.

The signal electrons that are emitted isotropically by the tritium β -decay in the source are guided via a magnetic field on a cyclotron motion to the spectrometer. Inside the spectrometer the magnetic field decreases by several orders of magnitude to a minimal value B_{\min} in the middle of the spectrometer, the so-called analyzing plane (AP). If the decrease in the B -field happens adiabatic (slowly enough) nearly all transverse momentum from the cyclotron motion of the electrons is converted into longitudinal momentum, as the magnetic orbital moment μ of the electrons is an invariant of motion:

$$\mu = \frac{E_\perp}{B} = \text{const.} \quad (3.1)$$

Simultaneously an electrostatic field is applied inside the spectrometer that has a maximum potential $U_{\max} \approx 18.6 \text{ keV}$ in the AP of the spectrometer. Only electrons with a longitudinal energy $E_\parallel > |q \cdot U_{\max}|$ can pass this potential wall, while electrons with lower energies are filtered out. By varying the retarding potential the integrated spectrum can be observed.

The filter width of the MAC-E filter depends on the magnetic fields:

$$\frac{\Delta E}{E} = \frac{B_{\min}}{B_{\max}}. \quad (3.2)$$

For the KATRIN Main Spectrometer the design filter width is $\Delta E = 0.93 \text{ eV}$.

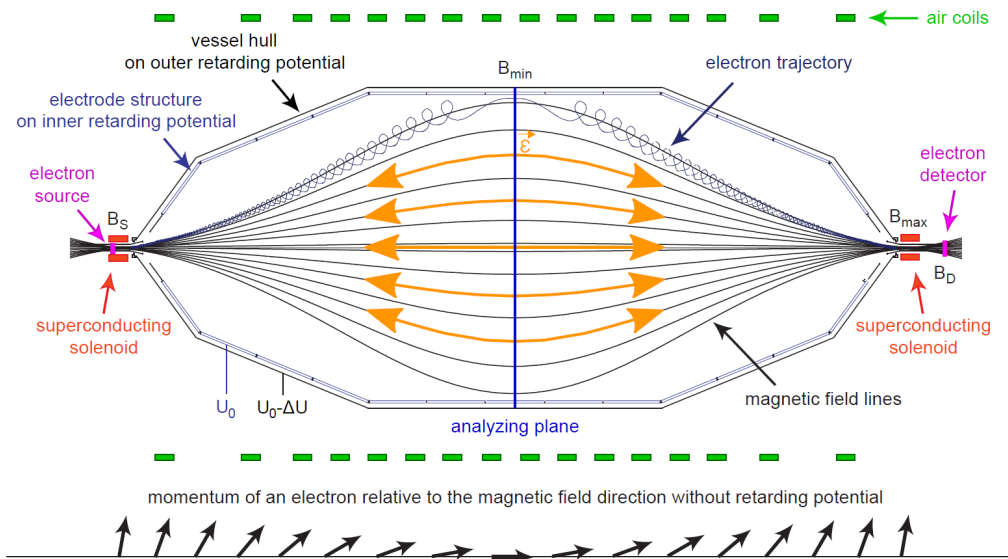


Figure 3.1.: The MAC-E filter principle. Figure adapted from [Zac09].

MAC-E filters were used by groups in Mainz [Pic92] and Troizk [Lob85] to measure the neutrino mass. Like KATRIN both experiments used a tritium source as emitter, but both could not determine the neutrino mass and only published upper limits for the electron (anti)neutrino mass:

$$\begin{aligned}
 \text{Mainz :} & \quad m_\nu < 2.3 \text{ eV (95 \% C.L.)} & [\text{Kra05}] , \\
 \text{Troizk :} & \quad m_\nu < 2.05 \text{ eV (95 \% C.L.)} & [\text{Ase11}] , \\
 \text{Combined :} & \quad m_\nu < 2.0 \text{ eV (95 \% C.L.)} & [\text{Ber13}] .
 \end{aligned} \tag{3.3}$$

The KATRIN experiment aims to exceed its predecessor experiments by a factor of 10 in sensitivity, to finally measure the neutrino mass.

3.2. Components of the KATRIN Experiment

The setup of the 70-m long KATRIN experiment is shown in figure 3.2. The experiment is subdivided in two main parts, on the one side the Source and Transport Section (STS) located in the Tritium Laboratory Karlsruhe (TLK) which is composed of the Rear Section (RS), the Windowless Gaseous Tritium Source (WGTS), the Differential Pumping Section (DPS) and the Cryogenic Pumping Section (CPS). On the other side the Spectrometer and Detector Section (SDS) that is composed of the Pre-Spectrometer (PS), the Main Spectrometer (MS) and the Focal Plane Detector (FPD). The TLK and the spectrometer hall are separated by a wall for reasons of radiation protection. Additional, the Monitor Spectrometer (MS), that is not included in figure 3.2, has to be mentioned.

3.2.1. Rear Section

The Rear Section (RS) is the back end of the experimental setup and has a couple of calibration and monitoring functions. A gilded beryllium plate called rear wall defines the potential inside the tritium source [Bab12]. An electron gun (e-gun) is mounted to the RS to shoot electrons through a small hole in the center of the rear wall, to e.g. determine the source column density ρ_D inside the WGTS (see section 3.2.2) [Hug10] [Val11]. By detecting X-rays generated by interaction of β -electrons from the tritium decay in the rear wall the activity of the tritium source can be monitored via the BIXS system [Mau09, Roe11, RP13].

Electrons from the e-gun and the rear wall illumination can be used to investigate the alignment of the full KATRIN beamline.

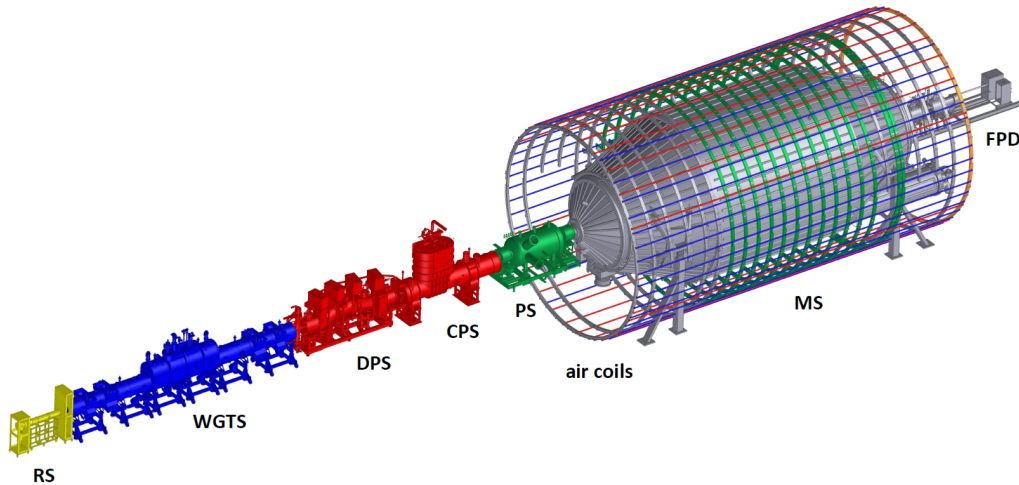


Figure 3.2.: The KATRIN experimental beamline consists of the following main components: the Rear Section (RS), the Windowless Gaseous Tritium Source (WGTS), the Differential Pumping Section (DPS), the Cryogenic Pumping Section (CPS), the Pre-Spectrometer (PS), the Main Spectrometer (MS) and the Focal Plane Detector (FPD). The Monitor Spectrometer which is not part of the main beamline is not shown. Figure adapted from [Sch14].

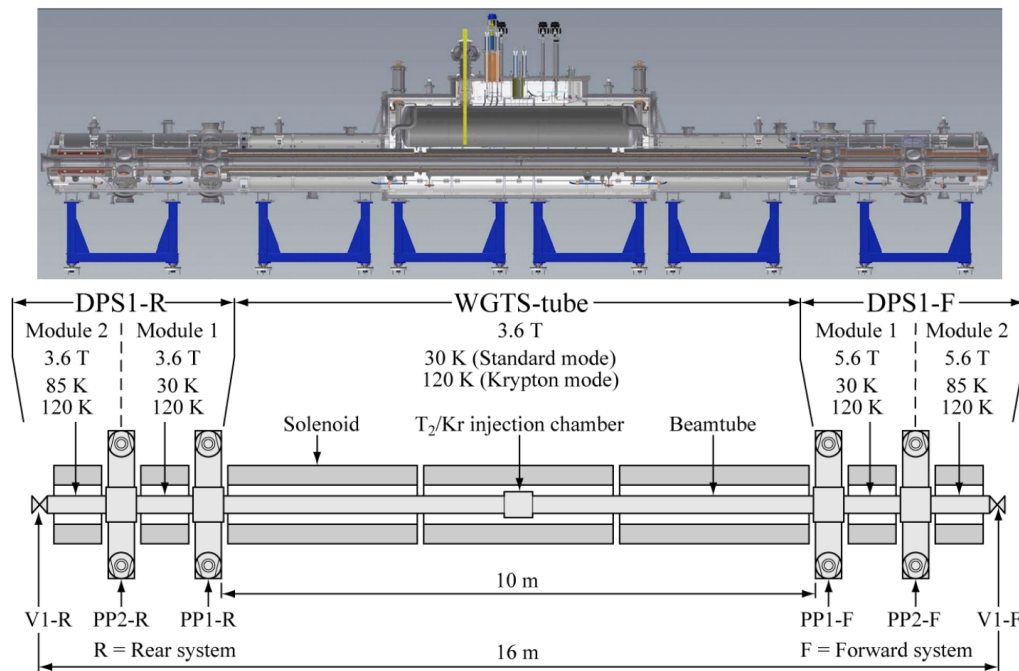


Figure 3.3.: The windowless gaseous tritium source (WGTS) as a CAD-model (top) and as schematic drawing (bottom). Figure adapted from [Hoe12].

3.2.2. Windowless Gaseous Tritium Source

The source of β electrons from tritium decay in the KATRIN experiment is the WGTS, which is shown in figure 3.3.

The center of the WGTS is a 10 m long cylindrical tube with a diameter of 90 mm [Ang05]. $5 \cdot 10^{19}$ tritium molecules per second are injected into the beam tube in the middle of the WGTS and extracted with turbo molecular pumps (TMP) at the differential pumping

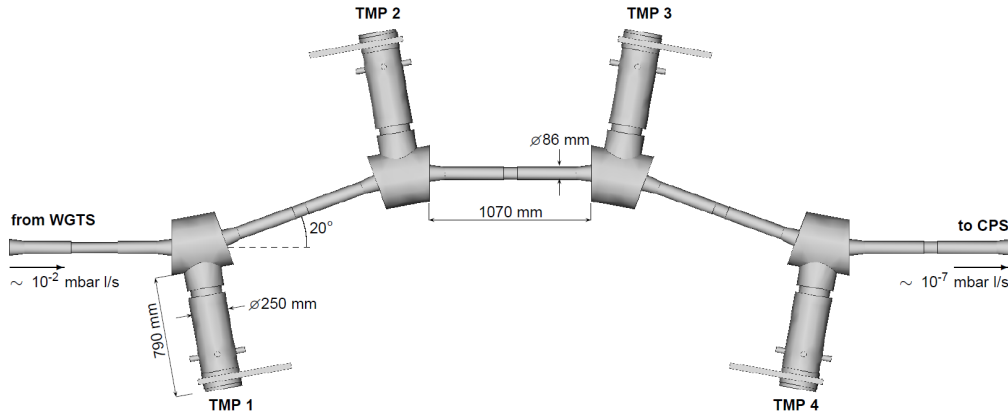


Figure 3.4.: Geometry of the DPS. Electrons from the WGTS are guided through a chicane in the beamline by a magnetic field, whereas neutral tritium molecules hit the wall and can be extracted by turbomolecular pumps (TMP). Figure adapted from [Luk12].

sections (DPS1-R and DPS1-F) on both sides of the source tube. The pressure at the injection point is on the scale of $p_{\text{in}} = 10^{-3}$ mbar at an operation temperature of $T = 27$ K which leads to a T_2 column density of $\rho d = 5 \cdot 10^{17}$ cm $^{-2}$. The resulting β -activity of the tritium gas is $A = 10^{11}$ s $^{-1}$. The β -electrons are guided by a magnetic field of $B_S = 3.6$ T that is generated by three superconducting magnets around the WGTS-tube. With a reserve of 4 mm in radial direction to compensate misalignments and a resultant accepted source area of $A_S = 53$ cm 2 it follows a magnetic flux tube of 191 T cm 2 .

Around the beam tube inside the WGTS there are seven superconducting solenoids, three surrounding the WGTS-tube and two in each, the DPS1-R and the DPS1-F. Additional dipole coils are mounted in the DPS1-R and DPS1-F that are able to shift the flux tube up and down (y-direction) or east and west (x-direction).

3.2.3. Differential Pumping Section

The differential pumping section (DPS) is the first part of the transport section. The DPS is about 6 m long and has a trapezoid like beam pipe with an inner diameter of about 100 mm and an angle of about 20°. A drawing of the DPS is shown in figure 3.4. Electrons are guided adiabatically through this chicane by a strong magnetic field of about 5.0 T generated by five superconducting magnets, one magnet surrounding each beam tube. Neutral tritium molecules (T_2) in contrast are not deflected and thus can not pass through the DPS but hit the wall. In four pump ports located between the magnets turbomolecular pumps reduce the flux of tritium molecules by five orders of magnitude [Luk12]. The tritium is fed back to the source by a loop system. Another duty of the DPS is the reduction of the ion flux from the source. Inside the WGTS about 10^{12} ions (mostly T_3^+) are produced per second by β -decay and secondary ionization. The ions get blocked by a ring electrode with a potential of +100 V, that is located in the beginning of the fifth beamtube, after TMP 4. To neutralize these ions dipole half-shells are arranged in beam tubes two, three and four, that lead the ions to the wall of the beam tube by $\vec{E} \times \vec{B}$ -drift [Rei09]. To analyze the ions coming from the source two FT-ICR (Fourier Transform - Ion Cyclotron Resonance) mass spectrometer are located in the first and fifth beamtube [UDRL09]. The FT-ICR modules are able to measure the number of ions and to discriminate the kind of the ions.

3.2.4. Cryogenic Pumping Section

The CPS is the second part of the transport section. It is composed of seven beam tubes and seven superconducting magnets. Similar to the DPS the beam line is arranged as a

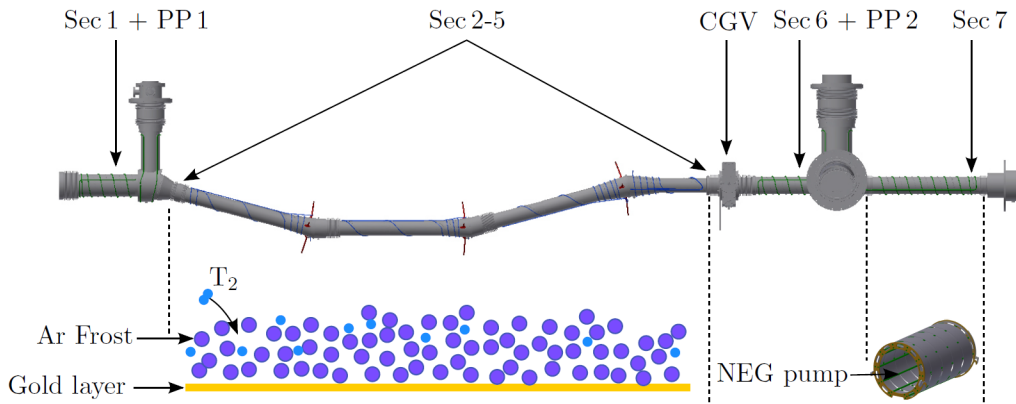


Figure 3.5.: Geometry of the CPS. The CPS is divided into seven beam tubes, here called Sec 1-7. The spiral structure around the beam tubes represents the cooling system. The capture of T_2 molecules in the argon frost in Sec 2-5 is illustrated. Figure adapted from [Jan15].

chicane through which the electrons are guided adiabatically by a strong magnetic field of up to 5.75 T. In contrast to the DPS the chicane has an angle of only 15° that is furthermore pointed in opposite direction. To reduce the flux of tritium the beam pipe in the chicane is cooled down to 3 K. On its surface a film of argon frost is created in which T_2 molecules get caught with a high probability [Gil10]. An illustration of the CPS and the capture of T_2 molecules in the argon frost is shown in figure 3.5.

At the end of the CPS in pump port two (PP 2) the forward beam monitor (FBM) is located. The FBM is a silicon detector with which the intensity of the electrons and thereby the tritium source activity can be monitored.

To calibrate the SDS a ^{83m}Kr source can be moved into the flux tube in PP 2. The source produces mono-energetic electrons with an energy of $E = (17824.3 \pm 0.5) \text{ eV}$.

3.2.5. Pre-Spectrometer

The PS is the first part of the SDS. The 3.38 m long vessel with an inner diameter of 1.68 m is located between the two superconducting magnets PS1 and PS2. Both magnets have a nominal magnetic field of $B = 4.5 \text{ T}$ in the center of their coils. The PS is electrically isolated from other components and can be set on high voltage. With a potential of 18.3 kV, 300 V under the endpoint energy, the flux of signal electrons that enter the MS can be reduced by up to seven orders of magnitude.

Figure 3.6 shows a the outer geometry and a view inside the PS.

On the inside of the vessel there are different types of electrodes: ground, shielding, cone and wire electrodes. The ground electrode is held at ground potential, while the others can be elevated to high voltage.

To generate a ultra high vacuum (UHV) of 10^{-11} mbar the PS is equipped with two TMPs and a SAES St707 getter pump with a total length of getter strips of 200 m and a width of 30 mm [ABB16].

3.2.6. Main Spectrometer

The MS is currently the largest ultra-high vacuum vessel in the world with a length of 23.3 m, an inner diameter of 9.8 m and an outer diameter of 10.0 m. It has a volume of

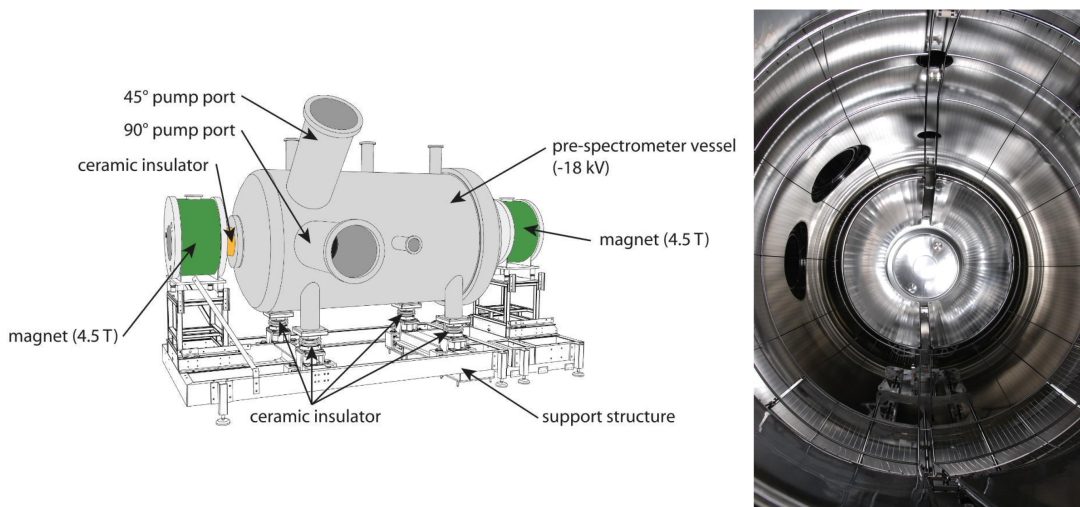


Figure 3.6.: Geometry of the pre-spectrometer (PS). Left: CAD model of the PS. Figure adapted from [Fra10]. Right: Look inside the PS showing the electrode system.

1240 m³, an inner surface of 690 m² respectively 1240 m² considering electrodes, baffles etc., and a weight of approximately 200 t.

As described in section 3.1, the MS is used as a MAC-E filter. The magnetic field is defined by the PS2, the Pinch Magnet and the air coil (AC) system. The latter also serves the purpose of compensating the earth magnetic field.

With a maximum of the magnetic field $B_{\max} = 6$ T in the Pinch Magnet bore and a minimum of $B_{\min} = 3 \cdot 10^{-4}$ T in the center of the MS, the MAC-E filter achieves a filter width of $\Delta E = 0.93$ eV according to equation 3.2.

Inside the MS a wire electrode system is installed to electrostatically shield the volume from electrons emitted from the inner surface of the vessel.

The UHV inside the MS is generated by three getter pumps, each with getter strip with a length of 1000 m and a width of 27 mm. Each of the getter pumps is located inside one of three pump ports with a diameter of 1.7 m. Since traces of radioactive Radon are emitted from the getter material, liquid N-2-cooled baffles are installed in front of the getter pumps cryosorb Radon. Two of the three pump ports are additionally equipped with three TMPs. With this cascaded pumping setup, a pressure of 10^{-11} mbar can be achieved [ABB16].

3.2.7. Focal Plane Detector

The FPD is a PIN diode detector on a silicon wafer. With a diameter of 90 mm it is segmented in 148 equal area pixels arranged in 12 concentric rings with 12 pixels each plus an additional four-pixel bulls-eye in its center (see figure 3.7).

The detector wafer is placed inside the warm bore of the Detector Magnet, a superconducting magnet with a nominal magnetic field of 3.6 T.

To accelerate electrons a post-acceleration electrode (PAE) is installed in the detector system. It can shift the detector region of interest (ROI) for the detection of the β -electrons to an energy region with a lower intrinsic detector background rate, accelerate low-energetic electrons to a level over the electronic noise, e.g. for background studies, and reduce the probability of backscattering [Ren11].

An illustration of the full detector system is shown in figure 3.8.



Figure 3.7.: The detector wafer. For spacial resolution it is segmented into 148 equal area pixels arranged in 12 concentric rings with 12 pixels each plus an additional four-pixel bulls eye in the center. Figure adapted from [Wal13].

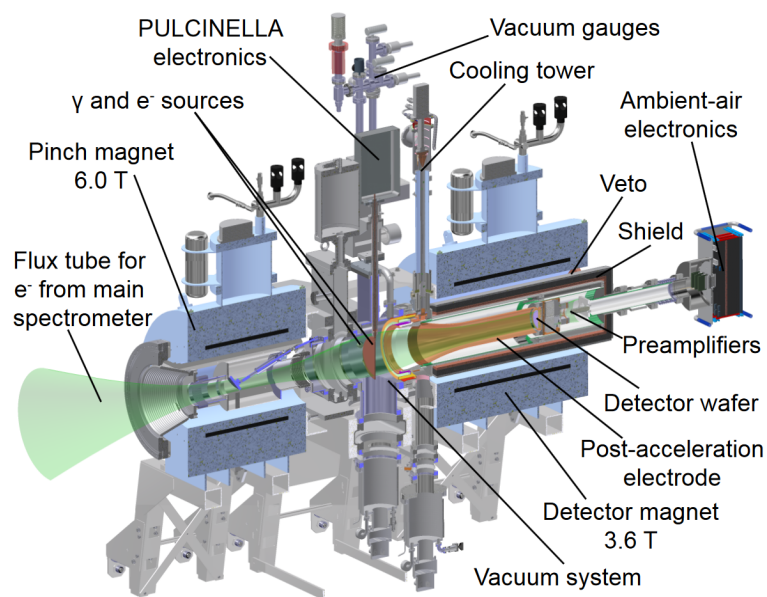


Figure 3.8.: Overview of the Focal-Plane Detector system. Figure adapted from [Ams15].

3.2.8. Monitor Spectrometer

The monitor spectrometer is the third MAC-E filter based spectrometer of the KATRIN experiment. The vessel, formerly used in the predecessor experiment in Mainz is 4 m long and 1 m in diameter. It is now used to monitor voltage fluctuations in the voltage system of the MS by monitoring mono-energetic electrons with an energy $E = (17824.3 \pm 0.5)$ eV emitted by a radioactive $^{83\text{m}}\text{Kr}$ source.

4. Simulations with Kassiopeia

Simulations for this thesis were performed with the Kassiopeia simulation software. In this chapter a basic overview of Kassiopeia is given in section 4.1 while a more detailed description of the implementations of the global KATRIN beamline into Kassiopeia in the context of the thesis in hand is given in section 4.2.2. More detailed information about Kassiopeia in general can be found in [FGT17].

4.1. Kassiopeia

Kassiopeia is a simulation software framework for field calculation, particle generation and particle tracking written in C++ and developed by the KATRIN collaboration starting in 2010. Different particles like electrons or ions can be created and tracked in electromagnetic fields including interactions with gas particles or geometry surfaces.

For each simulation the settings are defined in XML-files (Extensible Markup Language) including geometries, electromagnetic field calculation, generation, tracking and termination of particles.

After calculating the electromagnetic field from input values like magnet currents and electric potentials, particles are generated. A surface can be used as starting point particle tracking, as well as any arbitrary position by specifying the respective coordinates. Starting conditions like position, energy or direction can be set as a constant value, values from a formula, a set of values, or random values. To track particles an exact, adiabatic, or magnetic tracking can be chosen. An exact tracking of particles is only necessary if the particle movement is non-adiabatic. If this is not the case, the faster adiabatic tracking should be preferred. The magnetic tracking is used, if the field lines are to be visualized. In the following this will be called “field line simulation”.

The simulation itself is subdivided into runs, events, tracks, and steps. One run can have several events, an event can have several tracks, and each track is split into calculation steps. After each step, it is checked, if termination conditions have occurred. Conditions could be hitting a surface, or the excess of a defined maximum distance to a geometry in any direction. After every step a step output is written that can include information about the position of the particle or the magnetic field at that position. With the termination of a particle, the track ends. Afterwards a track output is written, that can contain information like the initial and final position or the creator and the terminator of the track. In case of the detector wafer as a terminator, the output can include the ID of the pixel that was hit.

Kassiopeia is able to visualize geometries and tracks in different ways. Three should be mentioned here, since they will be used in the following:

- The GeometryViewer shows a three dimensional model of the geometry,
- the GeometryViewerROOT opens a ROOT [BR96] window with a 2D lateral cut through the geometry, and

- the MeshViewer shows a three dimensional model of the meshed geometry.

Since some complex geometries are not yet supported by the GeometryViewer or the GeometryViewerROOT, some geometries will be presented in the MeshViewer visualization.

4.2. Implementation of the Global KATRIN Beamline into Kassiopeia

A good understanding of the geometry of the KATRIN beamline is needed to interpret the results of the measurements and to test changes for example of magnet orientations in advance. The latter is of big importance since a physical change of the experiment's hardware configuration can be time consuming.

To allow for simulations with the complete beamline of KATRIN, several components had to be implemented into Kassiopeia in the context of this thesis, while others had to be reworked, to allow for simulations that include misalignments of these geometries. The implementation of the global geometry is described in section 4.2.2, a preparatory overview of the alignment implementations and the user access via XML will be given in section 4.2.1

The right-handed coordinate system within Kassiopeia is defined by the MS. The axis from the upstream to the downstream flange of the MS defines the z-axis with the point of origin in the center of the MS vessel. The x-axis is set horizontally, and the y-axis points upwards.

To generate geometries within Kassiopeia an XML-file has to be created containing all necessary information. Different templates for basic and complex shapes can be used to form the desired structure. An example for a basic shape template is the rotated poly line surface. In this template, a line between any desired number of points, given by radius and z-position, is drawn in a two-dimensional plane. By rotating this line around the z-axis a three dimensional geometry is created. Complex shapes can be for example pump ports as described later. Multiple surfaces can be put into one space where they can be moved and rotated separately to combine them and create the desired composition.

4.2.1. Alignment Implementations

One important feature of the new geometry structure is the ability to shift and tilt every part of the beamtube and all magnet cryostats and coils separately. Experimentally determined alignment data from mechanical measurements that will be described in section 5.1 was implemented into the Kassiopeia geometry. Since a shift of a beam tube element in the experiment is compensated by bellows, the implementation in Kassiopeia was made such that the same appears within the simulation. Components with a fixed connection are shifted and tilted together up to the middle of the next bellow. Every part of the beamtube is shifted and tilted from bellow to bellow. The bellows compensate shifts by length adaptation, tilts are not compensated.

For each component six alignment values are needed, one shift per spatial direction (Δx , Δy , Δz) and three Euler angles (α , β , γ), to fully describe the new position. In Kassiopeia the z-x'-z''-convention for Euler rotation is used. That means that the component is tilted around the z-axis, afterwards around the new x-axis x', and finally around the new z-axis z''. Since for an axial symmetric object the third euler angel is irrelevant, for most components of the KATRIN experiment, five values are sufficient. In fact $\gamma \stackrel{!}{=} -\alpha$ in order to get correct results for nested geometries where components are rotated multiple times.

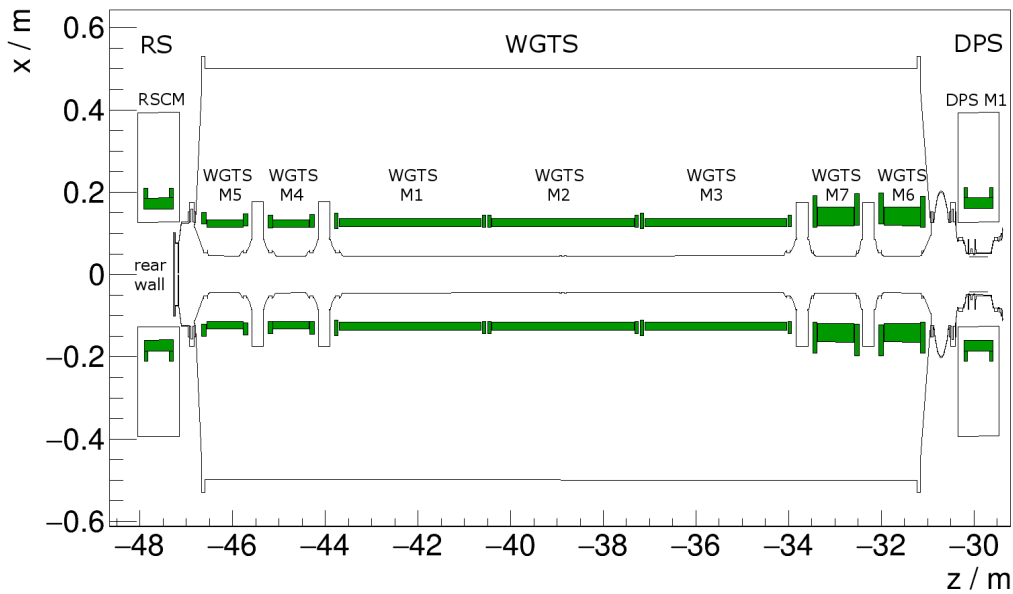


Figure 4.1.: WGTS geometry as implemented in Kassiopeia. Magnet coils are shown in green.

4.2.2. Global Geometry

Geometries for all main components of the KATRIN experiment were implemented by various members of the KATRIN collaboration. For this thesis it was necessary to combine all parts into a global geometry to simulate the magnetic fields and particle movement through the whole KATRIN beam line. In the following a tour through this now implemented full beamline will give a detailed view on every component, simplifications, and features.

RS and WGTS

The geometry of the RS and the WGTS as implemented in Kassiopeia is shown in figure 4.1. The RS geometry is up to now reduced to the part from the rear wall to the flange that connects it to the WGTS. The only magnet included is the superconducting re-condenser magnet (RSCM), all normal conducting magnets are not yet integrated. Since there are no bellows between the WGTS and the rear wall, the RS is tilted together with the WGTS cryostat.

The pump ports of the DPS1-R and DPS1-F are simplified as axial symmetric objects, since this is sufficient for electromagnetic tracking simulations.

In the experiment the WGTS beamtube is cooled down to about 30 K. This causes the beamtube elements to shrink. This is taken into account with a cooling factor, that reduces the length and the radius of the beamtube elements by a factor 0.997. The total length of the WGTS cryostat and the positions of the pump ports are constant, and the shrinkage of the individual components is compensated by bellows.

In principle the beamtubes of the WGTS can be tilted separately from the magnet coils. However, since there is no information available with regards to the relative alignment of the beamtubes to the magnets in Kassiopeia, both are tilted together. M1, M2 and M3 surround one long beamtube and are therefore tilted in common.

The dipole coils on both ends of the WGTS can not yet be visualized with the GeometryViewer. Therefore, they are shown in figure 4.2 in a MeshViewer visualization.

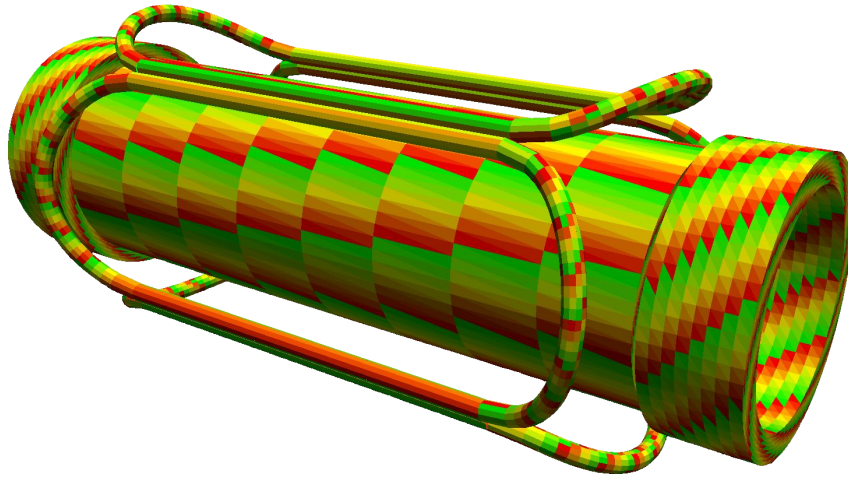


Figure 4.2.: Visualization of the WGTS M5 coil and the surrounding dipole coils with the MeshViewer.

DPS

Figure 4.3 shows the DPS geometry as implemented in Kassiopeia. The geometry of the four pump ports is available in a realistic and in a simplified model. Both are shown in figure 4.4 and both can not yet be visualized in the GeometryViewer. The DPS is connected to WGTS via PP0 and to the CPS via PP5. Beamtubes, PPs, magnet cryostats and magnet coils can all be tilted separately.

The magnets are available in an as-designed version and in an as-built version. The as-built version includes shifts and tilts of the coils inside the cryostat and the as-built number of coil windings.

The FT-ICR is included in BT1 and BT5. The dipole electrodes are included in BT2, BT3 and BT4 but can not be visualized with the GeometryViewerRoot. Figure 4.5 shows the Kassiopeia geometry of the dipole electrode alone and as installed inside BT3. In BT5 and PP5 ring electrodes are located, that can be put on potential to reduce the flux of positive ions. The ring electrode in PP5 is not yet included in the Kassiopeia geometries.

CPS

The geometry of the CPS is available as an as-built and an as-designed version as implemented by C. Röttele [Roe16]. The as-built version is shown in figure 4.6. As in the DPS, the CPS pump ports are implemented but can not be visualized by the geometry viewer. The same applies to the connections between the beam tubes. It was forgone to add the cryostat of the CPS since it has no impact on electromagnetic tracking simulations and could not be visualized in the geometry viewer either.

The as-built geometry only includes shifts and tilts of the beamtubes and the magnets, the tilt of the cryostat has to be added separately and is available for the as-designed model as well.

Inside the beamtube that connects the CPS to the PS another ring electrode for ion blocking is located.

PS

Figure 4.7 shows the pre-spectrometer and the two PS magnets. The electrode system as described in section 3.2.5 can be seen. PS1 surrounds the CPS-PS-beamtube that is the connection between the STS in the TLK and the SDS in the spectrometer hall and

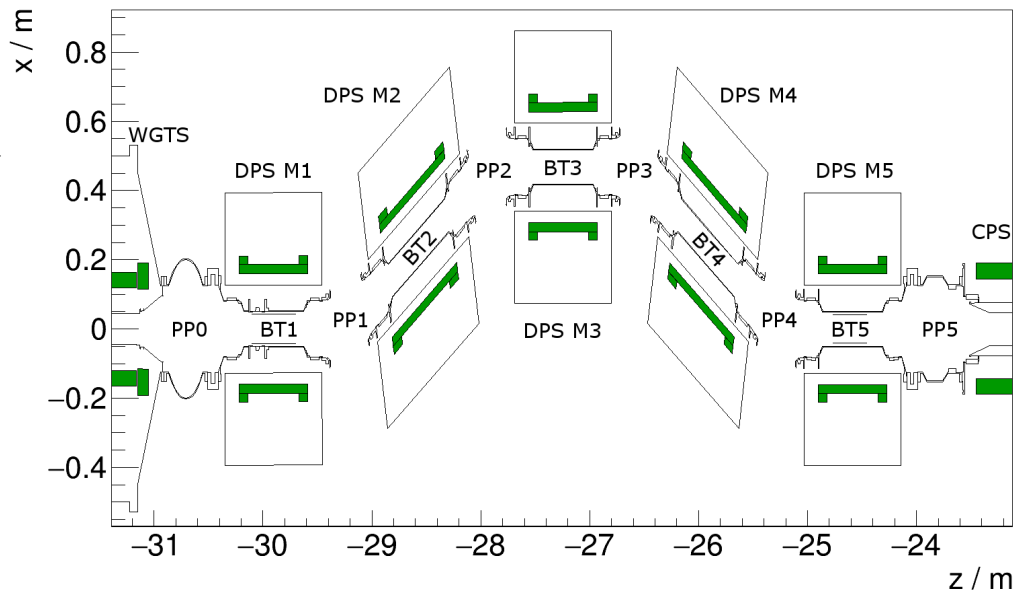


Figure 4.3.: DPS geometry as implemented in Kassiopeia.

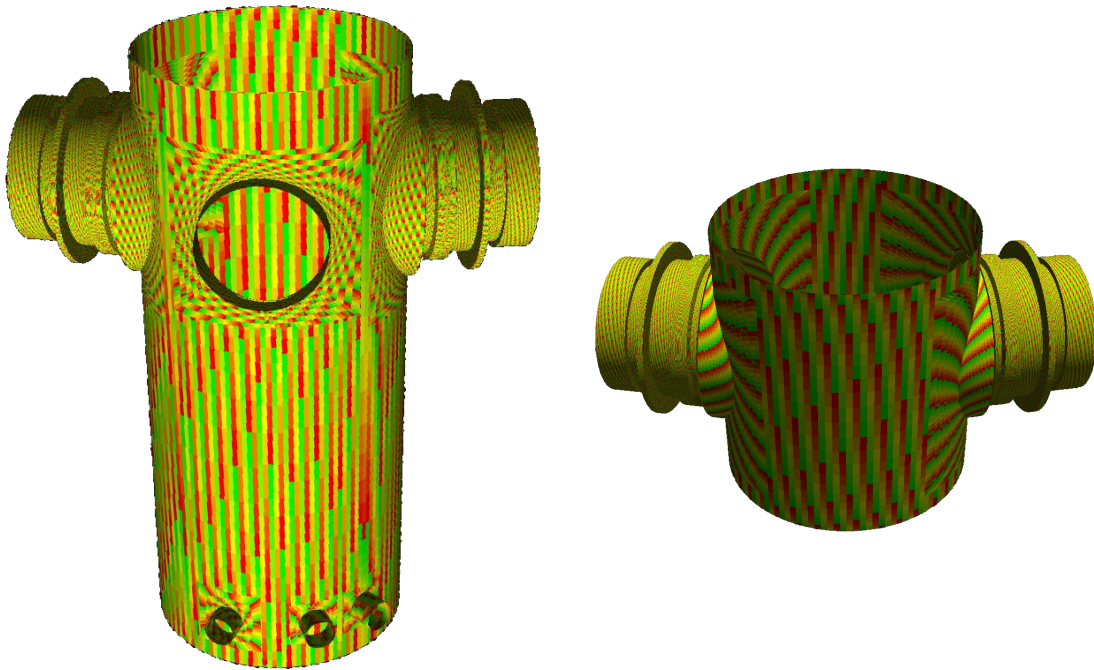


Figure 4.4.: Geometry of the DPS pump ports in the MeshViewer. Left: detailed geometry, right: simplified geometry.

goes through the wall of TLK that was added to the geometry as well. Inside of the PS2 magnet a flapper-based in-line beam valve (ILBV) is located. The flapper can be opened and closed by defining an opening angle. A view of the inside of the ILBV in real-life and in the simulation is shown in figure 4.8. The geometry of a new version of the PS ILBV as shown in figure 4.9 is available for later use. Inside the ILBV a ring electrode is located that is not yet included within the Kassiopeia geometries.

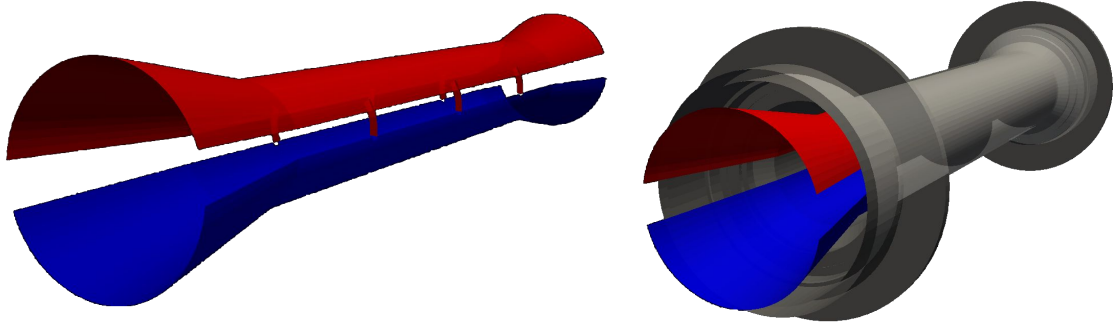


Figure 4.5.: Geometry of the DPS dipole electrodes alone (left) and as installed inside BT3 of the DPS (right).

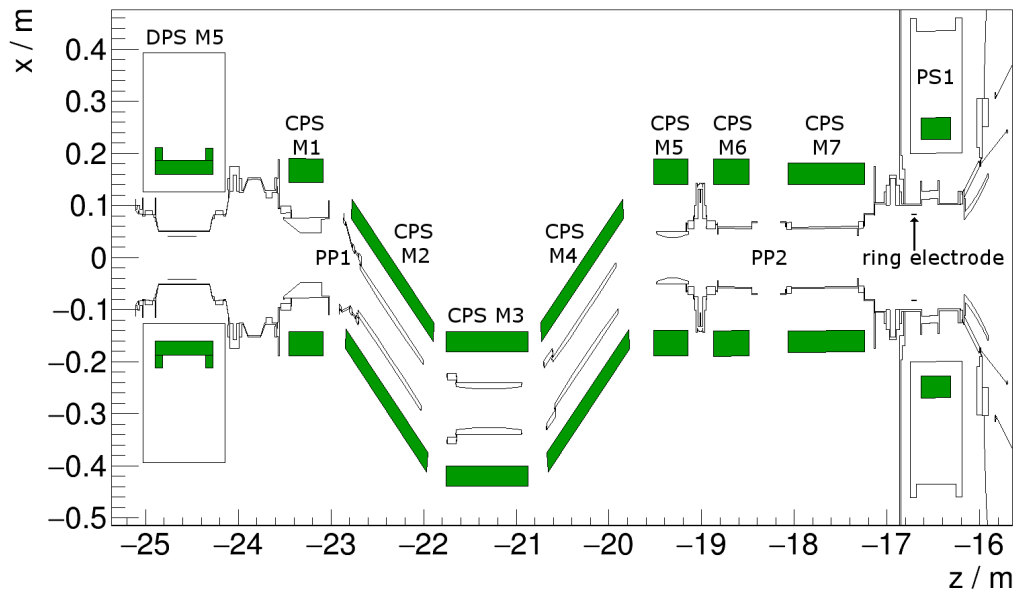


Figure 4.6.: CPS geometry as implemented in Kassiopeia.

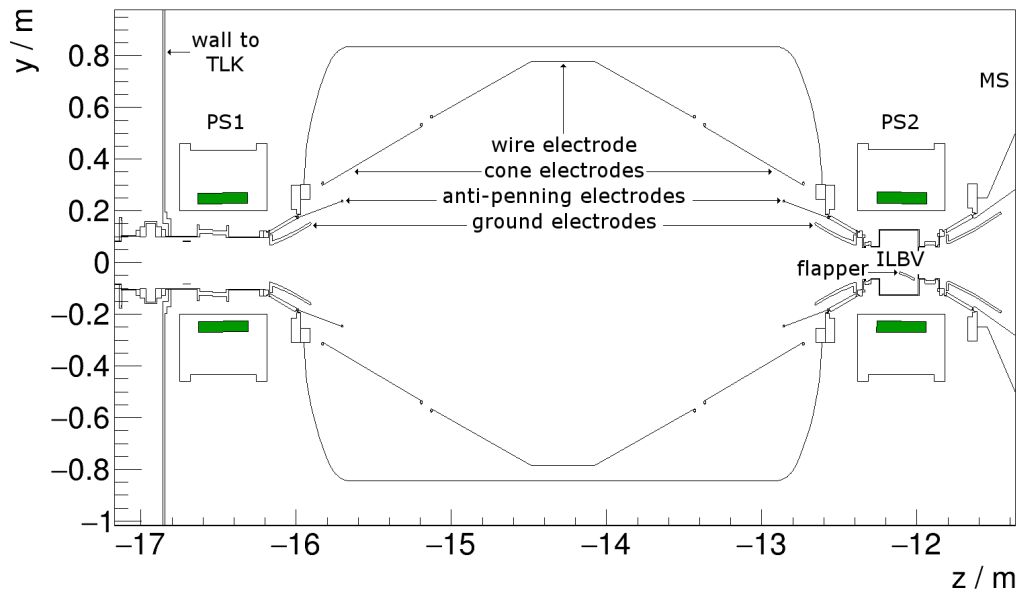


Figure 4.7.: PS geometry as implemented in Kassiopeia. At the bellow of the CPS-PS-beamtube inside PS1 the impact of the relative tilt between the components is well visible.

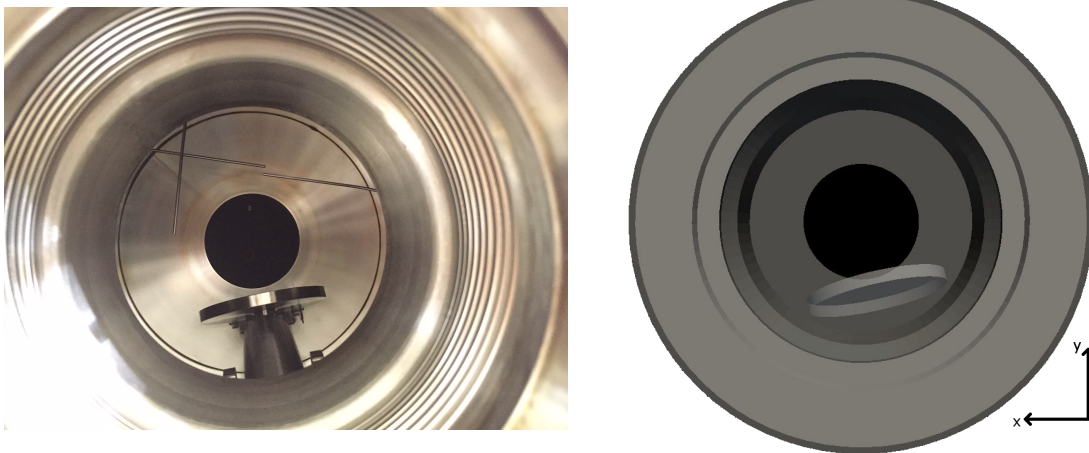


Figure 4.8.: Geometry of the ILBV Flapper. Left: Foto of the beam valve. Right: Beam valve geometry as implemented in Kassiopeia. The penning wipers are not yet included within the Kassiopeia geometry.

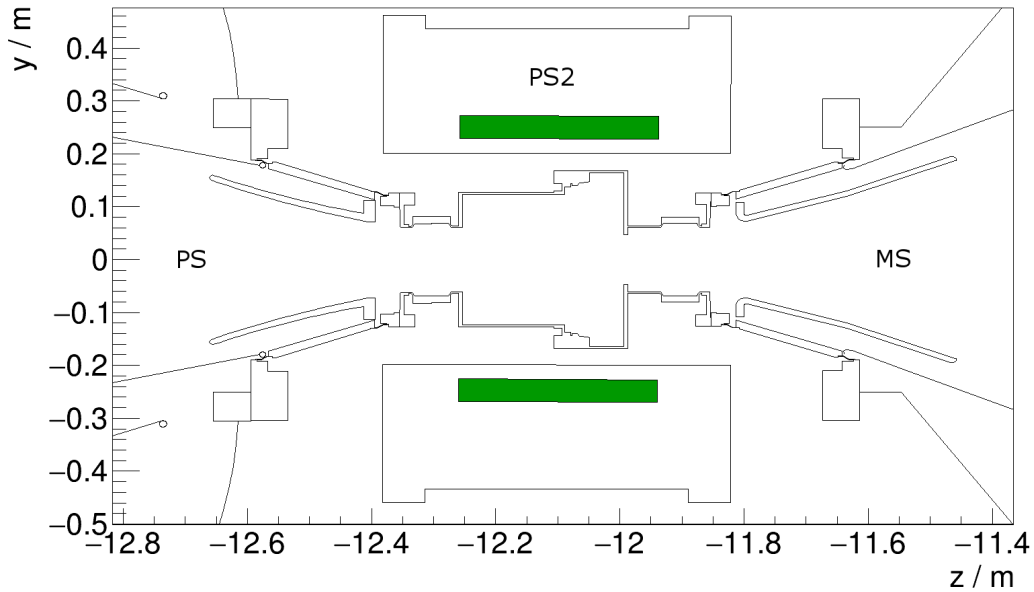


Figure 4.9.: Geometry of the new PS ILBV as implemented in Kassiopeia. This geometry was implemented for later use, since this hardware component exists and might be used in the future. It was not used for simulations in the context of this thesis.

MS

The MS geometry is shown in figure 4.10. The vessel is surrounded by the air coil system. Inside the vessel, an electrode system similar to the PS is installed. The MS ground electrodes at both ends and the wire electrodes can be seen. Here a simplified model with full electrodes is used, additionally a model with wires exists.

The MS defines the Kassiopeia coordinate system and can not be misaligned within Kassiopeia. The air coils were for simulations in context of this thesis only available as axial symmetric rings. M. Erhard implemented a corrected version with ideal rings, but effective ring radii and positions based on deformation and corrections [Erh16]. Additionally he did a full discretisation of the air coils. These implementations are now compatible with the global geometry.

FPD

Figure 4.11 shows the geometry of the detector system. The detector ILBV connects the MS with the detector system. The flapper of the detector-side ILBV is at the moment still simplified as an axial symmetric, conical frustum like object. Each component of the detector system (pinch magnet, detector magnet and vacuum chamber) can be tilted separately. Additionally the PAE can be tilted with respect to the surrounding vacuum chamber since a misalignment was found here experimentally.

4.2.3. Access to Alignment Data

To store all alignment data from different measurement campaigns, a new xml-file (“Non-AxialGlobalAlignment.xml”) was created. By including this file into the configuration file of a simulation, it is easy to access the required alignment data. Figure 4.12 shows a screenshot of a configuration with the current options. Components like the FPD or the DPS have several accessible sets of measured alignment values from different measurement campaigns that can be selected in the XML.

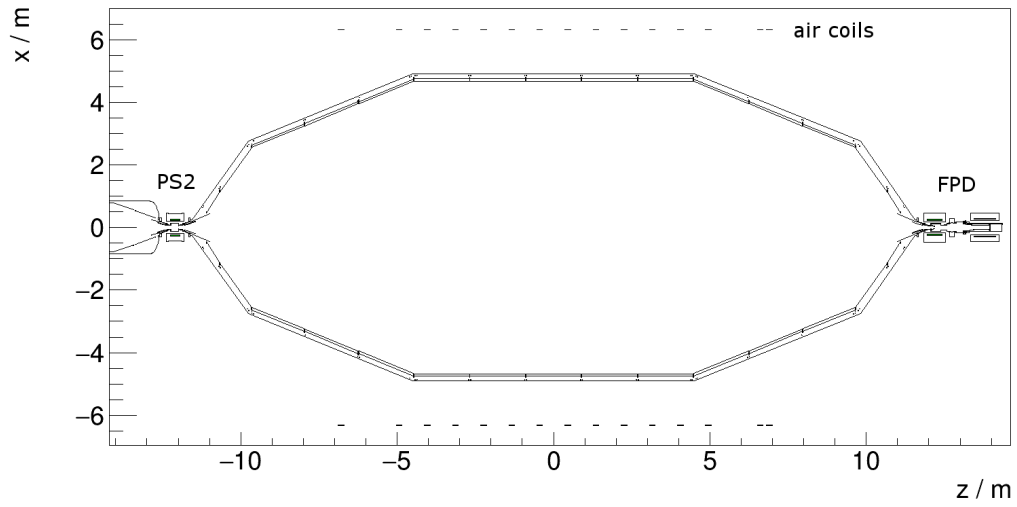


Figure 4.10.: MS geometry as implemented in Kassiopeia.

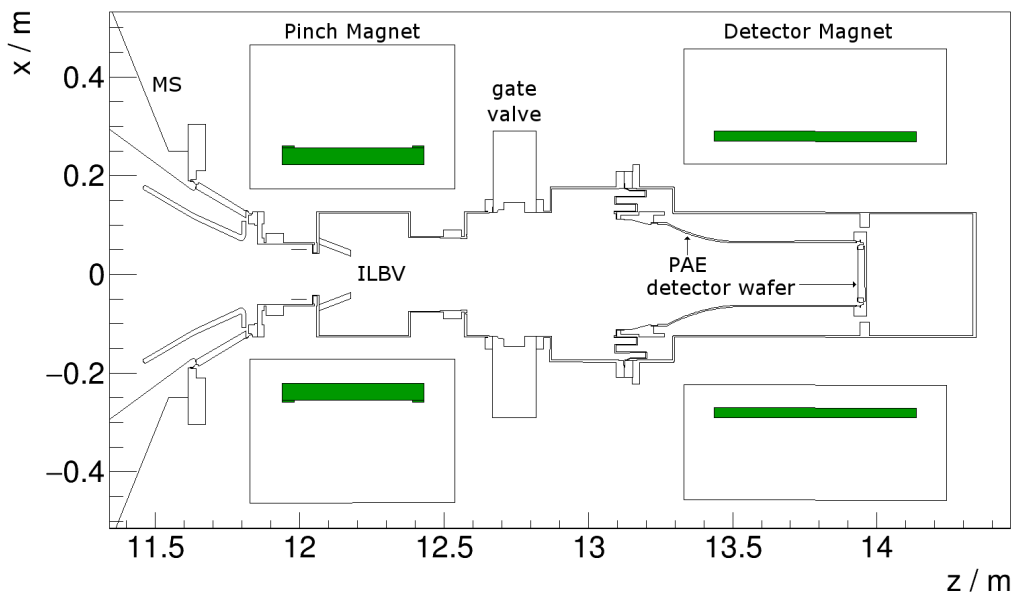


Figure 4.11.: FPD geometry as implemented in Kassiopeia.

```

<external_define name="fpd_tilted" value="4"/>
  <!-- 0: no tilts || 1: SDS-I tilts || 2: SDS-II tilts || 3: SDS-IIb tilts || 4: SDS-III tilts -->

<external_define name="fpd_phase" value="0"/>
  <!-- 0: standard detector ILBV || 1: SDS-I detector ILBV || 2: SDS-II replacement beam pipe -->

<external_define name="ps_tilted" value="1"/>
  <!-- 0: no tilts || 1: SDS-III tilts -->

<external_define name="ps_phase" value="0"/>
  <!-- 0: standard prespec ILBV || 1: new prespec ILBV (with tagger) -->

<external_define name="sds_magnets_tilted" value="5"/>
  <!-- 0: no tilts || 1: SDS-I tilts || 2: SDS-II tilts || 3: SDS-IIb tilts ||
      4: SDS-III tilts || 5: SDS-III tilts after PS adjustment-->

<external_define name="sds_magnets_phase" value="1"/>
  <!-- 0: old pinch magnet || 1: new pinch magnet -->

<external_define name="cps_tilted" value="1"/>
  <!-- 0: no tilts || 1: tilts -->

<external_define name="cps_use_as_built_coordinates" value="1"/>
  <!-- 0: as designed || 1 as built -->

<external_define name="dps_tilted" value="1"/>
  <!-- 0: no tilts || 1: tilts -->

<external_define name="dps_magnets_use_as_built_coordinates" value="1"/>
  <!-- 0: as designed || 1 as built -->

<external_define name="dps_magnets_tilted" value="3"/>
  <!-- 0: no tilts || 1: cryostat tilts (July 2015) || 2: after M3 cryostat tilt (September 2015) ||
      3: after M1 repair (November 2016)-->

<external_define name="wgts_tilted" value="1"/>
  <!-- 0: no tilts || 1: tilts -->

<external_define name="rs_tilted" value="1"/>
  <!-- 0: no tilts || 1: tilts -->

```

Figure 4.12.: Access to alignment data. By using external defines in the configuration file different sets of alignment data for each component and different geometries for exchanged components can be accessed.

Since the separation is not perfectly intuitive, some explanatory notes shall give additional information.

- Magnets and geometries of the SDS can be accessed separately, whereas on the STS side some components like the CPS or the WGTS can only be tilted as a whole.
- For the CPS there are two different options, one for tilting of the whole CPS cryostat (`cps_tilted`) and one for shifts and tilts of its inner geometries, like beamtube elements and magnets (`cps_use_as_built_coordinates`). The as-built geometry also includes corrections to sizes and turn numbers of coils.
- For the DPS magnets it is handled in a similar manner. The tilting of the magnet cryostats and beamtube elements (`dps_magnets_tilted`) is separated from the tilting of the coils inside the cryostats (`dps_magnets_use_as_built_coordinates`). Additionally the use the as-built geometry guarantees the as-built number of coil windings.
- For some components like the pinch magnet or the PS ILBV different geometries can be included due to the exchange of the particular component between different measurement campaigns.

Due to the extensive changes in all geometry XML files that were necessary to implement the global KATRIN beamline in the context of this thesis a new set of XML files for the global beamline has been set up in parallel to all old geometry files in Kassiopeia to guarantee backward compatibility.

- All geometry files of the global geometry are now stored in the directory `kasper/KSC/KGeoBag/GlobalXML` respectively `kasper/install/config/TheGlobalBag`.
- An exemplary configuration file can be found in `kasper/install/config/Kassiopeia/GlobalFirstLightSimulation.xml`.

4.2.4. Ongoing and Future Work

Some changes in the KATRIN beam line are planned, e.g. a fourth dipole electrode and new positions for the ring electrodes in the DPS. These plans are not yet taken into account in the Kassiopeia geometries but can easily be implemented.

For the rear section e-gun a geometry is implemented but not yet included in the global geometry, since it has to be modified for alignment data input.

Ongoing work restructures the access to the alignment data. The data will be stored in a database. By defining a date or run number, proper values for the alignment as well as values for magnet currents and voltages used in the measurement can be read out of the database. This will allow a very user friendly access to all available data.

For this thesis, no electrostatic models were included into the global geometry. Models for some components already exist, and only have to be adapted. For newly implemented geometries, models have to be built in order to allow for electric field calculations.

5. Preparatory Alignment Measurements

In October 2016 the first measurements were performed with the full KATRIN beamline during the First Light measurement campaign. To perform proper simulations with the global geometry as described in chapter 6 it was required to measure the alignment of all beamtube elements and all magnets. Different methods of preparatory alignment measurements will be described in this chapter.

5.1. Mechanical Beamline Alignment

Several different methods that were used to get alignment data for different components will be described in this section.

Uncertainties of the measurements will not be given, since they can not be taken into account within the implementations in Kassiopeia. However there are large uncertainties up to 300 % (cf. table 5.8 in [Gla15]).

5.1.1. FaroArm and Laser Tracker Measurements

FaroArm and Laser Tracker measurements allow a determination of beamtube element and magnet cryostat positions with a precision in the sub millimeter regime.

After calibrating the FaroArm respectively the Laser Tracker with four reference points located in stationary positions inside the hall, points on the surface of components can be measured.

With measured points rings and planes can be defined. For rings several points around circular beamtube elements or inside the circular holes of magnet cryostats are measured. Afterwards points at a flange or the planar end of the cryostat are measured to define a plane. The circle can then be projected on the plane to calculate the wanted center point of the object at the end of the element.

Positions of beamtube elements and magnet cryostats in the KATRIN hall were measured via laser tracker and FaroArm. From the center points of the upstream and downstream sides of the object, tilts and shifts relative to the nominal position and axis could be calculated.

Some components have been readjusted due to large deviations from nominal positions. For example the PS was originally placed 2.8 mm too high. This would have caused collisions of the fluxtube and the Penning electrodes of the PS and required a readjustment of the spectrometer. Table 5.1 shows the shifts and tilts for all components measured by FaroArm and Laser tracker measurements for the First Light measurement campaign.

Table 5.1.: Results of FaroArm and Laser Tracker measurements throughout the KATRIN beamline starting from the RS ending with the detector. The DPS beamtubes were not measured separately and are tilted together with the magnet cryostats.

Component	Δx in mm	Δy in mm	Δz in mm	α in $^\circ$	β in $^\circ$
RSCM	-0.0685	0.1185	-0.874	85.6749	0.0384
WGTS	0.612	-0.058	0.0005	29.0546	-0.0010
DPS M1 cryostat	0.050	-0.150	-0.700	143.7462	0.1199
DPS M2 cryostat	-0.026	-0.165	0.983	-31.9837	0.0354
DPS M3 cryostat	-0.688	-0.443	0.522	-1.4168	0.3675
DPS M4 cryostat	-0.125	-0.277	0.088	61.6933	0.2703
DPS M5 cryostat	-0.330	-0.003	1.098	6.6724	-0.0092
CPS cryostat	-0.170	0.084	0.509	15.9802	0.0022
PS1 cryostat	-0.050	0.325	-5.900	98.3151	0.1344
PS	0.600	-0.450	-0.450	63.4349	0.0109
PS2 cryostat	0.000	1.100	2.300	59.0362	0.1194
Pinch magnet cryostat	0.748	0.491	0.000	166.8908	0.0303
Detector system	0.048	1.611	8.3735	-131.6471	0.0625
Detector magnet cryostat	-0.477	1.226	2.406	-106.5476	0.0590

5.1.2. Magnetic Field Measurements

The position and alignment of magnet coils inside the cryostat can be determined by investigating the magnetic field on the upstream and downstream side of the cryostat.

A Hall effect magnetometer (*Lake Shore 460 3-Channel Gaussmeter*) was used to measure the magnetic field. To get reproducible results, an aluminum plate was screwed to each end of the cryostat. The aluminum plate has a 200 mm diameter hole, in which a rotatable PVC ring disc is embedded. Steps of 22.5° are labeled on the aluminum plate. The Hall effect magnetometer can be fixed at three adapted square holes with different radial displacements from the center. For this measurements only the square hole with the largest radius was used. A photography of the Hall effect magnetometer mounted to the holding structure is shown in figure 5.1.

To take possible systematic effects due to an asymmetry of the aluminum plate into account, the plate was mounted upside down for a second series of measurements. All values for the measurement at the Pinch magnet can be found in the appendix A.

In a perfectly aligned case, the magnetic field would be identical in all azimuthal positions. With a misalignment, a sine shaped variation of the measured field can be observed. Figure 5.2 shows an exemplary sine fit to the data measured on the upstream side of the Pinch magnet with the pinch magnet energized and the detector magnet switched off. A sine shape can be identified.

Due to the large uncertainties on the result of α , β , γ , Δx and Δy only a found Δz -shift of 2 mm of the Pinch magnet coil was implemented into the Kassiopeia geometries. For further analysis with smaller uncertainties of the other shifts and tilts a simulation based analysis would be required. For a detailed description of the measurement and analysis see [Mue14]. Values for the DPS coil position were taken from [Gla15], values for the PS1 and PS2 magnet from [Ada15].

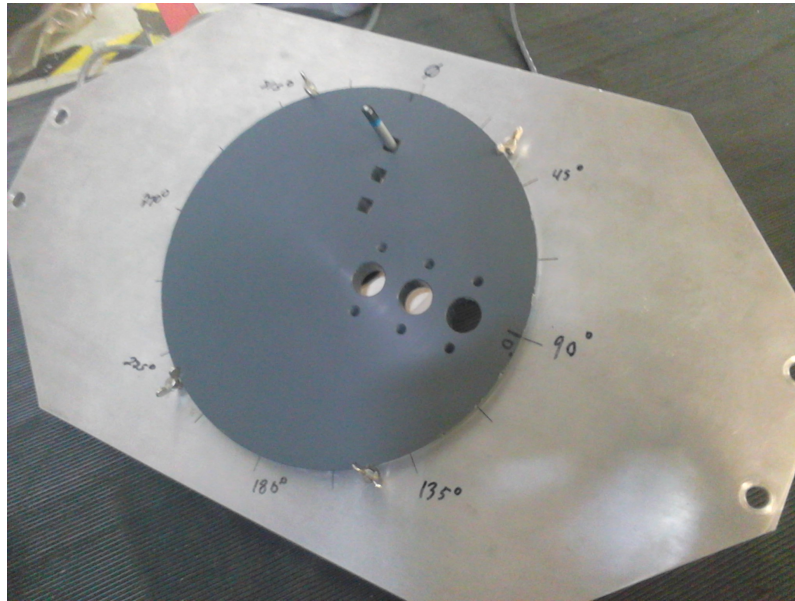


Figure 5.1.: Hall effect magnetometer of the *Lake Shore 460 3-Channel Gaussmeter* installed into an assembly of a rotatable PVC disk in an aluminum plate. The assembly is installed to the magnet cryostats to measure the alignment of the magnet coil inside the cryostat.

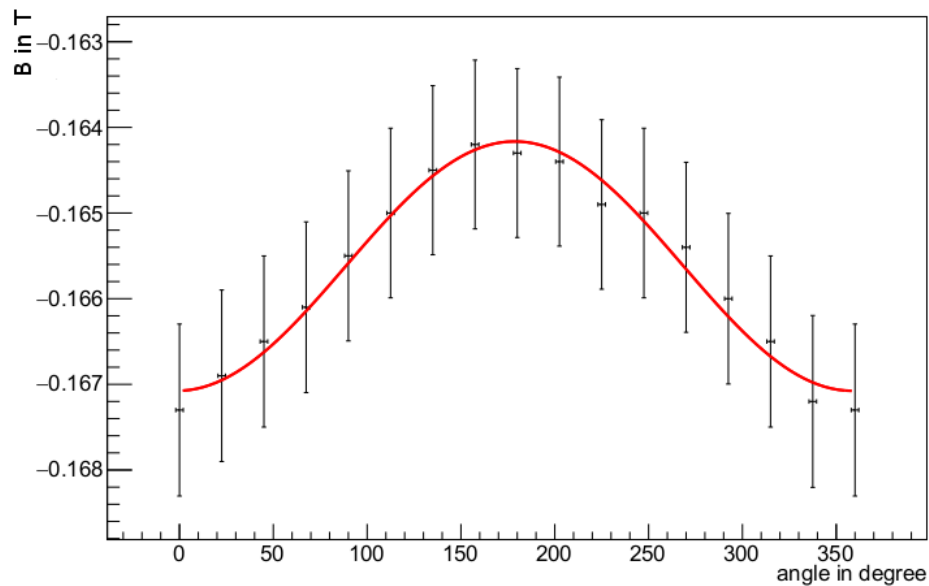


Figure 5.2.: Exemplary sine fit to pinch magnet alignment data for the measurement with $B_{\text{Pinch}} = 3 \text{ T}$ and $B_{\text{Det}} = 0 \text{ T}$ at the upstream side of the pinch magnet with the aluminum plate attached upside down. The uncertainty on the measured B -field specified by the manufacturer is 0.6% from the measured value, the angular was estimated at $\pm 2^\circ$

5.1.3. WGTS Beamtube Alignment

The WGTS beamtube alignment was measured with a measuring probe called “pig” that was pulled through the WGTS beamtube on a thread. The pig is a cylinder in which the ball with the mirror for laser tracker measurements was placed. Since the thread was pulled by hand, the movement was not constant and some spikes appear in the data. In addition the pig fell into the pump ports between the beamtubes which causes peaks as well.

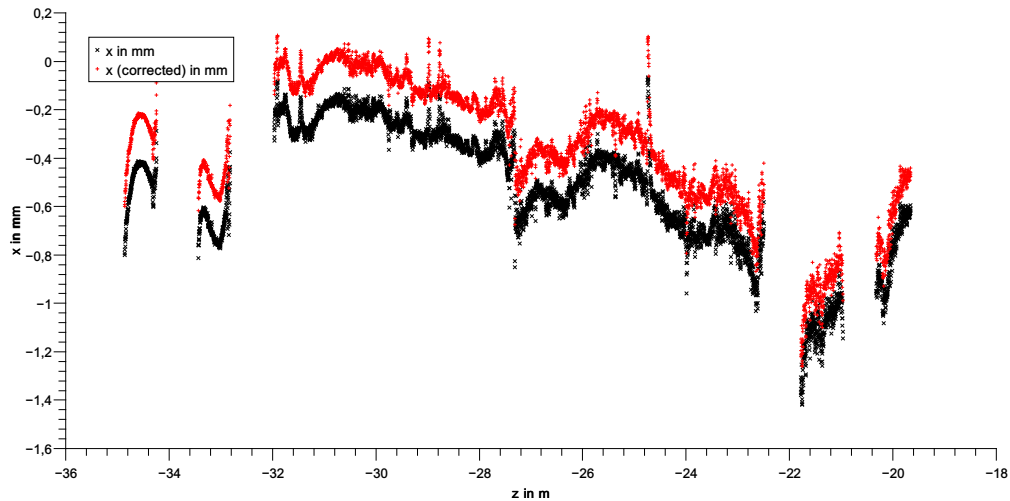


Figure 5.3.: WGTS alignment measurement data for the x-direction as measured with the pig system. For the correction, the tilt of the WGTS cryostat was relative to its nominal position was subtracted.

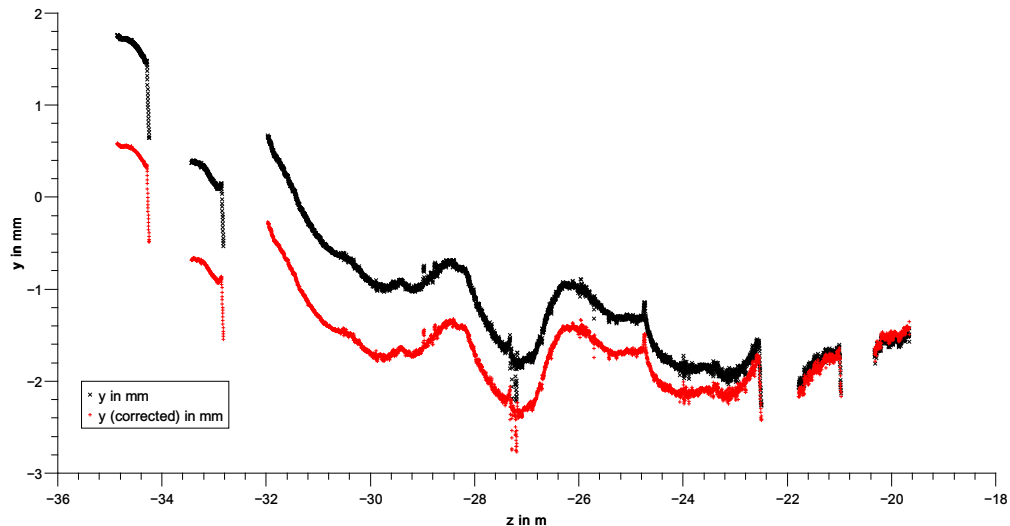


Figure 5.4.: WGTS alignment measurement data for the y-direction as measured with the pig system.

The data from this measurement is plotted in figure 5.3 for the x direction and figure 5.4 for y direction. To analyze the tilts the measured values were corrected by the tilt of the whole WGTS cryostat which was measured via Laser Tracker in advance. In addition the bad readings of the pig fell in regions of pump ports are not taken into account. From linear regressions for all beamtube elements separately the shifts and tilts could be calculated. Table 5.2 shows the results of these calculations.

5.2. FPD Alignment

The detector vacuum chamber is a more complex system that consists of two nested vacuum chambers, the PAE, the pinch magnet and the detector magnet. Based on FaroArm measurements the cryostats and the outer surfaces of the vacuum chambers, it was tried to align all components as good as possible. However, due to the nested setup and a cooldown of the PAE by $> 100^\circ$ the exact position of the detector wafer inside the chamber can not be measured directly.

Table 5.2.: WGTS beamtube alignment. Beamtubes from upstream to downstream side. Beamtubes 1, 2 and 3 are treated as one beamtube.

Beamtube	Δx in mm	Δy in mm	α in $^\circ$	β in $^\circ$
WGTS BT5	-0.2960	0.9866	42.1216	-0.0290
WGTS BT4	-0.5063	-0.2386	-25.3462	-0.0325
WGTS BT2	-0.2439	-1.1704	-33.4326	-0.0071
WGTS BT7	-0.9399	-1.3696	-31.5954	0.0357
WGTS BT6	-0.6298	-1.0194	-65.563	0.0393

To test the position of the detector wafer in reference to the detector system a radioactive americium ^{241}Am source can be mounted on a so-called alignment flange that is installed on the upstream end of the detector system when operated in stand-alone mode.

The alignment flange is made of stainless steel and has five boreholes, one in the middle and four on a circle in 90° steps. The ^{241}Am source can be installed into each hole. Figure 5.5 shows the combined pixel view for measurements with the source installed at all five positions. By fitting a ring to the outer four spots and calculating the center of the ring, the alignment can be tested. In the ideal case, the ring center would be at 0.0 mm in both x- and y-direction. In figure 5.6 (upper row) the results of the ring fit can be seen. It shows a misalignment of 1.25 mm in each x- and y-direction.

After moving the the detector chamber 1.2 mm horizontally along the x-axis and 1.0 mm (east) respectively 0.7 mm (west) upwards to correct for this misalignment, a second measurement was performed. Figure 5.6 (lower row) shows the ring fit after the adjustment. The misalignment could be decreased to -0.25 mm in x-direction and 0.25 mm in y-direction.

During these measurements, the detector system was fully assembled. However, to move the system towards the MS and to establish the connection of the beamline some parts of the system had to be removed. That means, that the results of this measurement are only in parts representative for the actual alignment of the detector system to the MS.

A second large uncertainty is the tilt of the PAE. Former measurements found a tilt of the PAE of $\alpha = -90.0^\circ$ and $\beta = -0.1542^\circ$ [Har15]. Another tilt can occur due to the cooling of the PAE and the detector wafer. Since the PAE is cooled by liquid nitrogen dropping down the cooling tower (cf. 3.8), the cooling is not homogeneous but stronger on its upper side. This causes the PAE to shrink more on the upper side leading to a deformation and a shift of the wafer position. This effect was not yet quantitatively examined.

5.3. MS-FPD Alignment

In strong electrostatic fields electrons from negatively charged surface can tunnel through the potential barrier into the vacuum. This effect is known as field electron emission [FN28]. The effect occurs at field strengths of 10^7 Vm^{-1} and gets dominant at about 10^8 Vm^{-1} depending on the geometry of the experimental setup. In the following, this effect will be used to map the inner surface of the MS (and later in section 5.4 of the PS) onto the detector to get information about the alignment of the detector to the MS.

5.3.1. MS-FPD Alignment Measurement

An asymmetric magnetic field setting as shown in figure 5.7 was used to map the inner surface of the MS with its electrode system onto the detector wafer. In this setting the Pinch magnet was set to $B_{\text{Pinch}} = 4.32 \text{ T}$ (72 %) and the detector magnet to $B_{\text{Det}} = 2.59 \text{ T}$

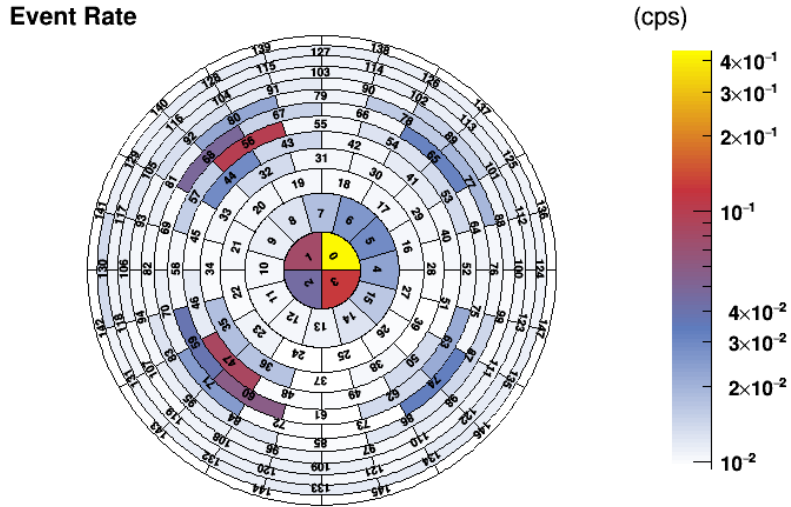


Figure 5.5.: Pixel view of the FPD alignment measurement with the americium source. Five spots corresponding to the five source positions on the alignment flange can be identified.

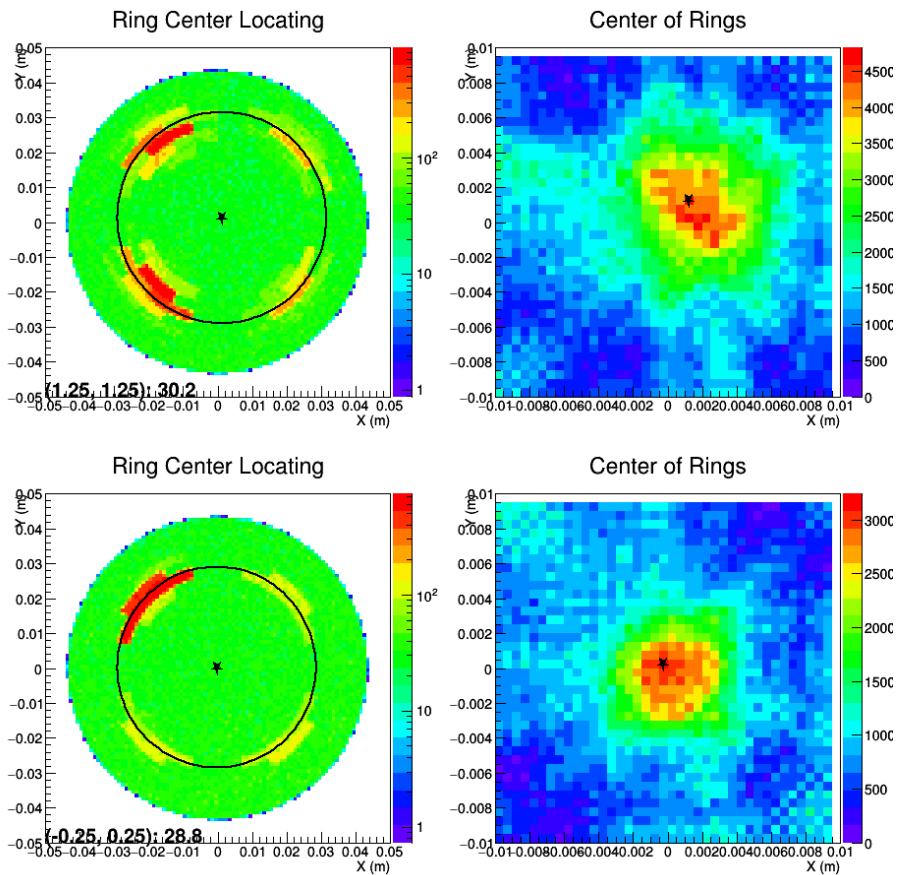


Figure 5.6.: Analysis of the FPD alignment measurement with the americium source. For each pixel, the number of events is spread randomly on the area of the pixel. The left column shows the ring fits. The numbers in the lower left corner give the ring center (x, y) and the radius of the ring. The right column shows for each pixel the goodness of a ring center calculated by a rms analysis. The upper row show the analysis of the measurement before the adjustment of the detector wafer, the lower row after the adjustment. The misalignment could be decreased by the adjustment.

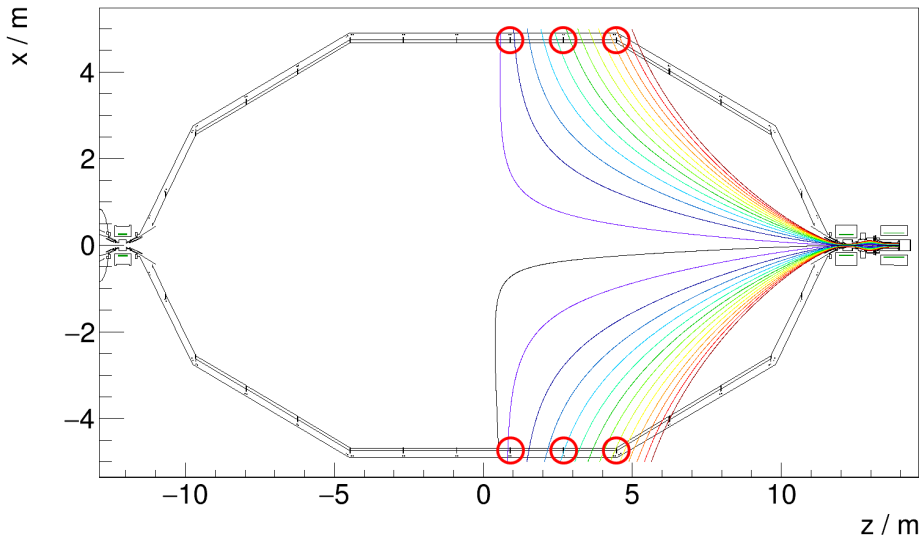


Figure 5.7.: Magnetic field configuration as used in the MS-FPD-alignment measurements. The field lines hit the inner electrode system of the MS. By measuring electrons emitted from the surface, the inner structures of the MS can be mapped on the detector and the alignment between MS and FPD can be tested. The red circles mark the holding structures, where electrons are started from in the simulation.

(72%), the PS magnets were switched off. Additionally three air coils were operated with switched polarity, AC2 at $I_{AC2} = -50$ A, AC3 at $I_{AC3} = -40$ A and AC4 at $I_{AC4} = -30$ A. All other air coils were switched off. The whole inner electrode system of the MS was set to -120 V. Due to their geometry, field electron emission takes place on the holding structures of the electrode system which are marked in figure 5.7. Therefore, rings corresponding to these holding structures are observed by the detector. A pixel view of the measurement is shown in figure 5.8. By analyzing the ring centers analog to figure 5.6, it is possible to make statements on the alignment of the detector wafer relative to the inner electrode system of the MS. In a situation with perfect alignment between the MS and the detector wafer the center of the rings should be located in the middle of the detector wafer. The measurement results indicate a slight shift of the rings of

$$\begin{aligned}\Delta x &= -0.25 \text{ mm} , \\ \Delta y &= -1.75 \text{ mm}\end{aligned}\tag{5.1}$$

from the center of the wafer.

5.3.2. MS-FPD Alignment Simulations

After including all data from mechanical alignment measurements in the Kassiopeia geometry, the simulation of the MS-FPD alignment and a comparison to the measurement results described in section 5.3 was possible.

Since the MS defines the coordinate system within Kassiopeia and is therefore not shifted, it was possible to start electrons in the simulation on rings with a radius of 4.67195 m at the z-positions of the electrode structures ($z_1 = 2.682$ m, $z_2 = 4.472$ m). The innermost ring was not simulated since this ring was only located on the innermost pixel ring at the wafer. Due to the large difference between the inner and outer radius of the inner pixel ring large uncertainties on the result are expected. For the simulation of the two rings 10^4 electrons were started per ring.

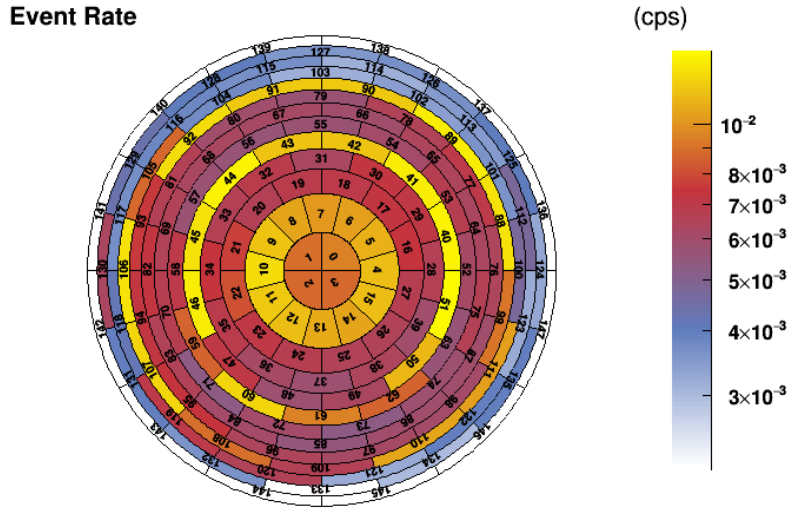


Figure 5.8.: Pixel view of the MS-FPD-alignment. The observed rings correspond field emission electrons emitted from the electrode structure of the MS.

Table 5.3.: MS-FPD-alignment results.

	ring center x in mm	ring center y in mm
inner ring	-2.125	-0.375
outer ring	-1.375	-0.625
mean	-1.75	-0.5
measurement	-0.25	-1.75
correction	-1.5	1.25

Figure 5.9 shows the results of the simulation with ring fits applied. The ring fits are only added for a better illustration. The analysis for the simulation is much more accurate when the information about the final position of the particles is used to calculate the center of mass rather than using the fit results.

Compared to the measurement, the rings in the simulation are shifted more to the left and less downwards. This discrepancy can be explained by the fact that the wafer position is not exactly known as mentioned in section 5.2. For upcoming simulations an effective correction shift of the wafer position in Kassiopeia are used. These shifts can be calculated by

$$x_{\text{correction}} = x_{\text{simulation}} - x_{\text{measurement}} \quad (5.2)$$

and

$$y_{\text{correction}} = y_{\text{simulation}} - y_{\text{measurement}} \cdot \quad (5.3)$$

The simulation's results and effective shifts are listed in table 5.3.

After the correction of the wafer position, the simulation was repeated. Figure 5.10 shows the pixel view of the simulation with the corrected wafer position. The ring center is now at

$$\begin{aligned} x &= -0.25 \text{ mm} , \\ y &= 2.13 \text{ mm} , \end{aligned} \quad (5.4)$$

which is in a better agreement with results of the measurement (see equation 5.1).

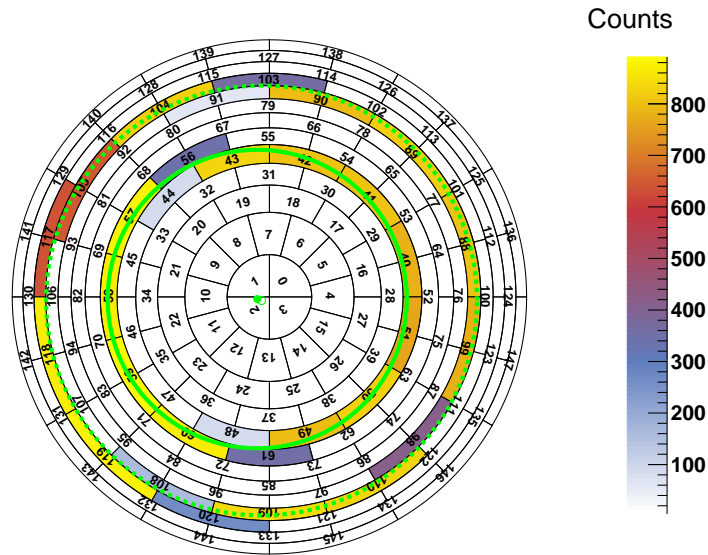


Figure 5.9.: Pixel view of the MS-FPD alignment simulation. The rings fitted to the pixel distribution are just an indicator for the shift, for the analysis the final positions were used. The filled marker belongs to the solid line, the empty marker to the dashed line.

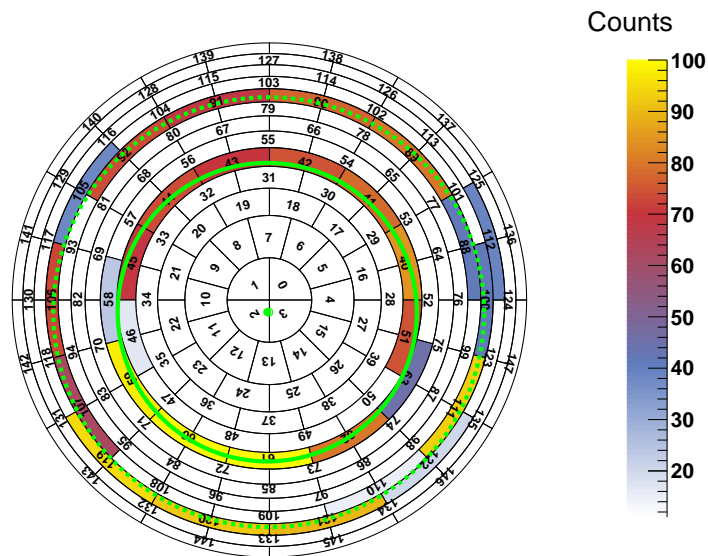


Figure 5.10.: MS-FPD-alignment simulation analysis after correction of the wafer position. The rings could be shifted to the right positions. The filled marker belongs to the solid line, the empty marker to the dashed line.

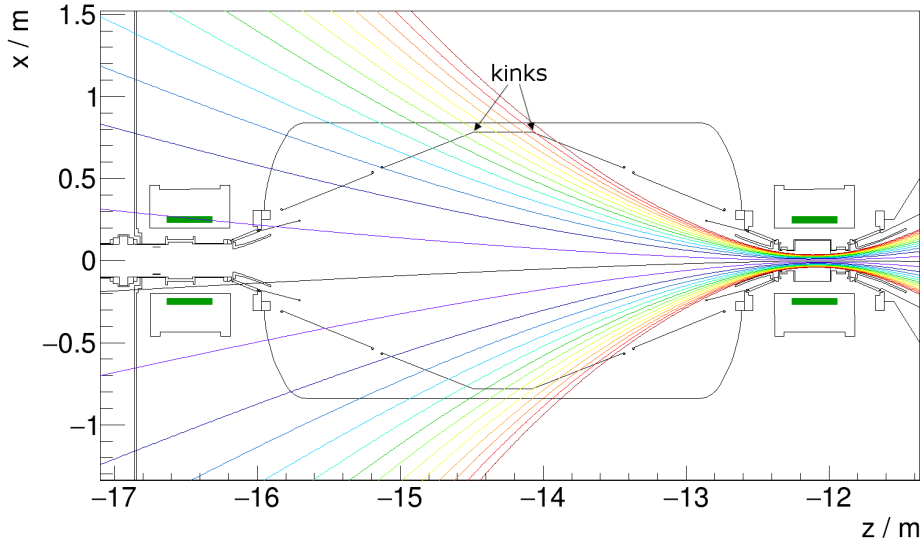


Figure 5.11.: Magnetic field configuration as used in the PS-FPD-alignment measurements. The field lines hit the inner electrode system of the PS. Analog to the MS, the inner structures of the PS can be mapped onto the detector and the alignment between PS and FPD can be tested by measuring electrons emitted from the surfaces.

5.4. PS-FPD Alignment

After analyzing the MS-FPD-alignment, the PS-FPD-alignment can be tested. The asymmetric magnetic field configuration that is used in these measurements is shown in figure 5.11.

5.4.1. PS-FPD Alignment Measurement

Analogous to the MS-FPD-alignment measurements, the electrodes inside the pre-spectrometer were set on a negative potential, and electrons emitted from specific parts of the electrode geometry by field electron emission are guided to the detector. The pixel view of the measurement is shown in figure 5.12. Here among ring shapes some hot spots on the pixels 79, 31, 37 and 109 originating from geometries in the gap between the wire electrodes can be identified (see figure 3.6). These pixels have to be excluded from the analysis to allow for correct ring fits.

The innermost ring originates from the solid cone electrode. This is made from full metal and therefore produces a high rate of electrons. However for alignment studies this ring is not a convenient indicator since the inner pixels have a large difference between the inner and outer radius. For this reason a ring fit would result in large uncertainties.

The outer two rings can be assigned to the holding structures at both ends of the cylindrical part of the wire electrode system. Only these rings were used for the analysis with ring fits.

Another noticeable effect is the in general lower rate on the lower part of the wafer. Investigations on the origin of this shadowing are still ongoing but it is assumed to come from an electrostatic charging of the flapper valve between the PS and the MS (see section 6.3).

In the PS-FPD case the analysis with ring fits appeared to be more difficult as in the MS-FPD case due to the shadow on the lower pixels. In some fits the loading of the pixel distribution produced a displacement of the fit towards the pixels with higher rate at the top of the wafer.

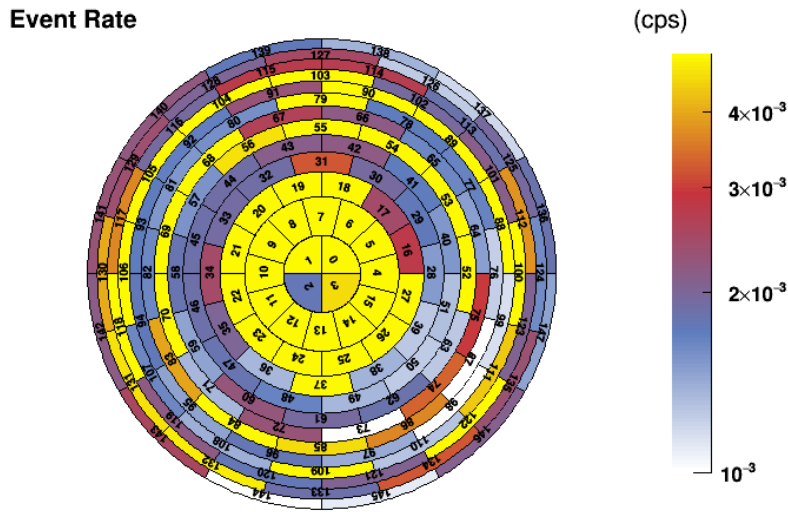


Figure 5.12.: Pixel view of the PS-FPD alignment. Three rings can be identified, the inner ring with higher rate corresponds to the cone electrode, the outer rings originate from the holding structures at both ends of the cylindrical part of the wire electrode system. The hot spots on the pixels 79, 31, 37 and 109 can be assigned to structures in the gap between the wire electrodes.

To crosscheck the results of the ring fits, the radius of the rings on the detector can be calculated by using the fact that the magnetic flux $\Phi = B \cdot A$ is constant. The value of Φ at the ends of the cylindrical part of the wire electrode system can be determined by simulations. Here no misalignments were used.

The resulting radii on the detector are:

$$\begin{aligned} r_{\text{inner,calculated}} &= 30.57 \text{ mm} , \\ r_{\text{outer,calculated}} &= 38.82 \text{ mm} . \end{aligned} \quad (5.5)$$

Figure 5.13 shows the ring fits for the measurement. Both rings show a shift to the bottom-left, with a mean of

$$\begin{aligned} \Delta x &= -1.25 \text{ mm} , \\ \Delta y &= -2.50 \text{ mm} . \end{aligned} \quad (5.6)$$

The radii of the ring fits are

$$\begin{aligned} r_{\text{inner,fit}} &= 30.8 \text{ mm} , \\ r_{\text{outer,fit}} &= 39.2 \text{ mm} \end{aligned} \quad (5.7)$$

which is in good agreement with the calculated radii in equation 5.5.

5.4.2. PS-FPD Alignment Simulations

To simulate the alignment between PS and FPD electrons were started at both ends of the cylindrical part of the wire electrode system of the PS. In this case it was not possible to use a fix radius around the z-axis since the PS is tilted within Kassiopia. Therefore a new geometry was added that can be used as a generator surface. It was decided to use two cylindrical surfaces with a radius of $r_{\text{generator}} = 0.7813 \text{ m}$, 0.1 mm smaller than the radius of the cylindrical part of the wire electrode system. In z-direction they were put at the position of the kink (see figure 5.11) with a distention of 0.1 mm towards the middle

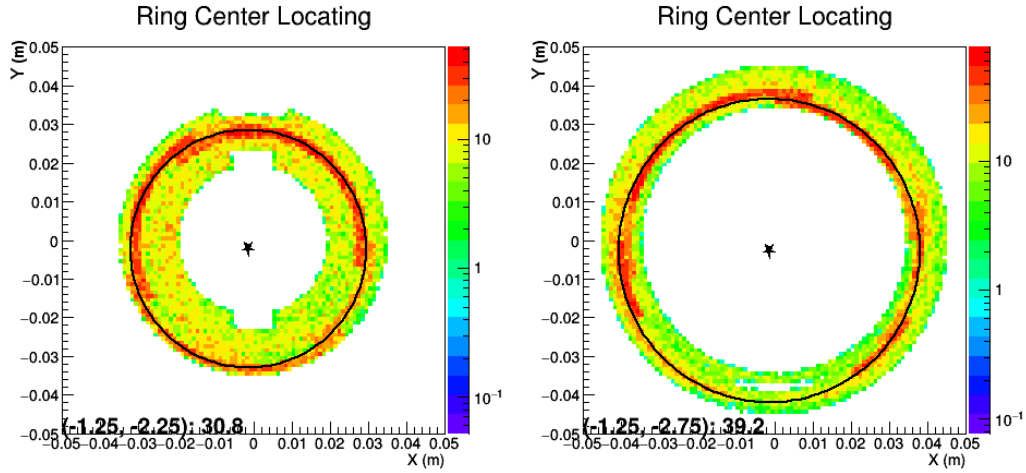


Figure 5.13.: Ring fits for the measurement of the PS-FPD-alignment for the inner ring (left) and the outer ring (right).

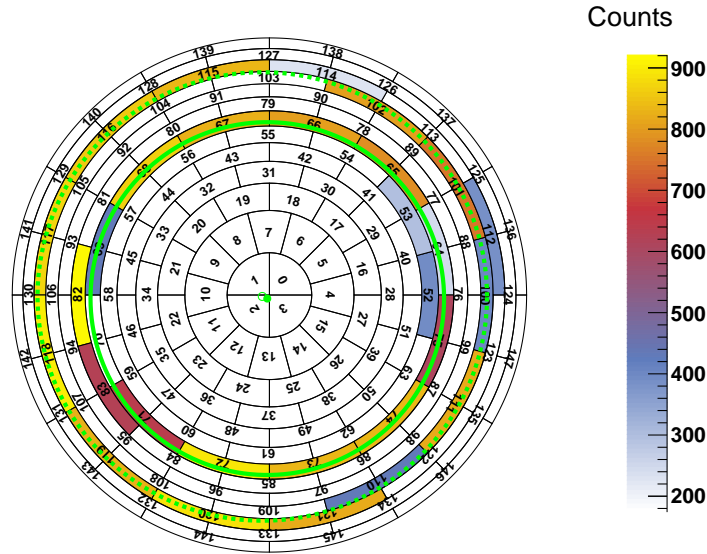


Figure 5.14.: PS-FPD-alignment simulation. The pixel distribution is in good agreement to the measurement. The analysis with ring fits again simply serves to illustrate the shift. The filled marker belongs to the solid line, the empty marker to the dashed line.

of the PS. The advantage of these generator surfaces is, that they can be shifted and tilted together with the PS geometry and therefore represent the positions of the holding structures of the wire electrode system quite well.

For this simulation the corrective shifts of the detector wafer calculated in section 5.3 were included.

Figure 5.14 shows the pixel view with a ring fit analysis of the simulation. Again the ring fits are only added for a better illustration, for the analysis the final positions of the tracks were used to calculate the center of mass.

The analysis provided a shift of

$$\begin{aligned}\Delta x_{\text{simulation}} &= 0.13 \text{ mm} , \\ \Delta y_{\text{simulation}} &= -1.50 \text{ mm} .\end{aligned}\tag{5.8}$$

These values deviate sharply from results of the measurement. One possible reason is the

Table 5.4.: PS-FPD alignment results.

	ring center x in mm	ring center y in mm
measurement	-1.25	-2.50
simulation with corrective wafer shift	+0.13	-1.50
simulation without corrective wafer shift	-1.76	-0.51

ring fitter used to analyze the measurement results. As described the lower rate on the lower pixels can influence the weighting of the fitting algorithm.

The corrective shifts of the detector wafer could be the cause of this discrepancy as well. A rough back calculation to the center without the corrective wafer shift gives results that are much closer to the measured ones. Thus, it was decided to repeat the simulation without the corrective detector wafer shift. In this case the shifts of the ring centers are

$$\begin{aligned}\Delta x_{\text{simulation, repeated}} &= -1.76 \text{ mm} , \\ \Delta y_{\text{simulation, repeated}} &= -0.51 \text{ mm} .\end{aligned}\tag{5.9}$$

Still these values do not match the results of the measurements in equation 5.6 perfectly.

Table 5.4 summarizes the results of the measurement and the simulations.

A possible reason for the discrepancies between measurement and simulation is the uncertainty of the PS2 magnet tilt. In this setting the magnetic field inside the PS is mainly defined by the PS2 magnet. A tilt of PS2 would affect the alignment of the field lines relative to the PS geometry. If the tilt in the simulation is different than in the measurement, the observed deviation could occur.

Another possible explanation could be an unknown misalignment of the electrode system inside the PS or the MS.

5.5. Discussion of Uncertainties

As mentioned before, uncertainties from mechanical alignment measurements can not be taken into account for simulations with Kassiopeia. However differences of shifts and tilts of magnets between measurement and simulation can cause deviations in the results.

Uncertainties of the FaroArm and laser tracker measurements are expected to be in the range of about 0.5 mm.

The hall probe has an uncertainty of 0.6% on the magnetic field and the angular position can be adjusted with an error of $\pm 2^\circ$. Results of shifts have an uncertainty ≤ 0.7 mm, tilts of 1° [Mue14]. However, the results for the alignment of the DPS magnet coils relative to the cryostats based on these magnetic field have uncertainties on the euler angle α of $\pm 25^\circ$. These errors propagate to the results of the simulation.

Results of the measurements and the simulations of the MS-FPD and the PS-FPD alignment are not in perfect agreement. But due to the large errors on the results of mechanical alignment measurements it is plausible that the deviation between measurement and simulation is covered by the uncertainties on the simulation. However, a quantitative analysis was not carried out in the context of this thesis.

6. Global Beamline Alignment

On October 14th the KATRIN experiment celebrated its “FirstLight” event when for the first time electrons were guided through the complete 70 m long experimental beamline. This FirstLight event was the starting point of a 7 weeks long measurement campaign with the full KATRIN beamline in which i.a. the global beamline alignment was tested. In this chapter first results of these alignment measurements will be presented as well as being compared to simulations with Kassiopeia.

6.1. First Light Measurement Campaign

During the First Light measurement campaign electrons were generated at the Rear Section of the experiment and guided along the beamline to the detector. To generate the electrons two different systems could be used. Firstly a UV illumination of the rear wall which is described in detail in section 6.1.1, and secondly an ion source which was alienated to use it as an electron gun as it is explained in section 6.1.2. In order to select different fieldlines along which the electrons are guided through the experiment two magnetic dipole coils located in the WGTS were used to shift the electron beam (see section 6.1.3).

6.1.1. Rear Wall Illumination

In order to generate low-energy photo electrons across the whole cross-sectional area of the magnetic fluxtube the gold plated rear wall was illuminated with ultra violet (UV) light.

Figure 6.1 shows the pixel view for a measurement with electrons from UV illumination of the rear wall. In this measurement all magnets were set to 20% of the nominal field, while the detector magnet was operated at 26 % (14.6A). In this way the whole fluxtube could be investigated. the low rate on pixels 72 and 85 comes from low energy blocking as described in section 6.3. On the right side an additional blocking is observed, which is a sign for collisions of the electrons with the wall of the beamtube. The resulting shifts from a center of mass analysis for this measurement are

$$\begin{aligned}\Delta x_{\text{measured}} &= 4.30 \text{ mm} , \\ \Delta y_{\text{measured}} &= 6.22 \text{ mm} .\end{aligned}\tag{6.1}$$

For these simulations the same magnetic field settings were used. With the global KATRIN beamline implemented in Kassiopeia (see chapter 4) and all known misalignments along the beamline taken into account it was possible to compare the measurement to the simulation. The pixel view of the simulation is shown in figure 6.2.

Except missing the shadow on the lower part of the detector, the pixel distribution of the simulation looks quite similar compared to the measurement result. In both cases the

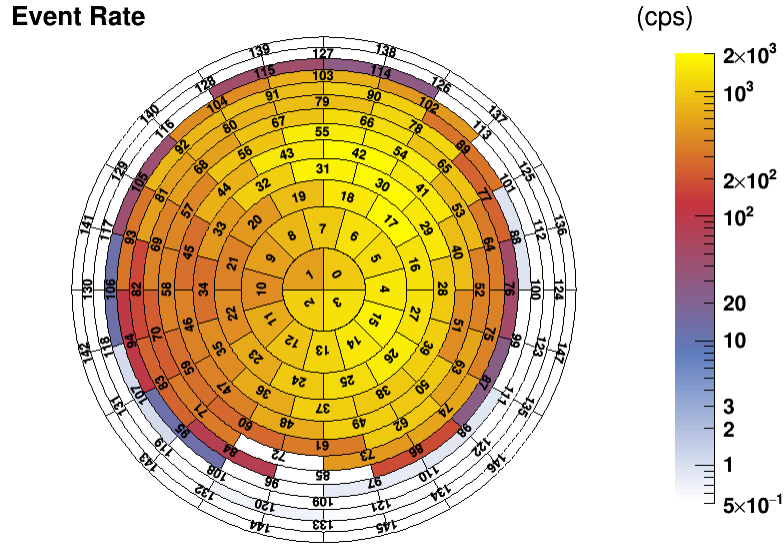


Figure 6.1.: Measurement of electrons from rear wall illumination. The shadow on the lower pixels comes again from low energy blocking (see section 6.3)

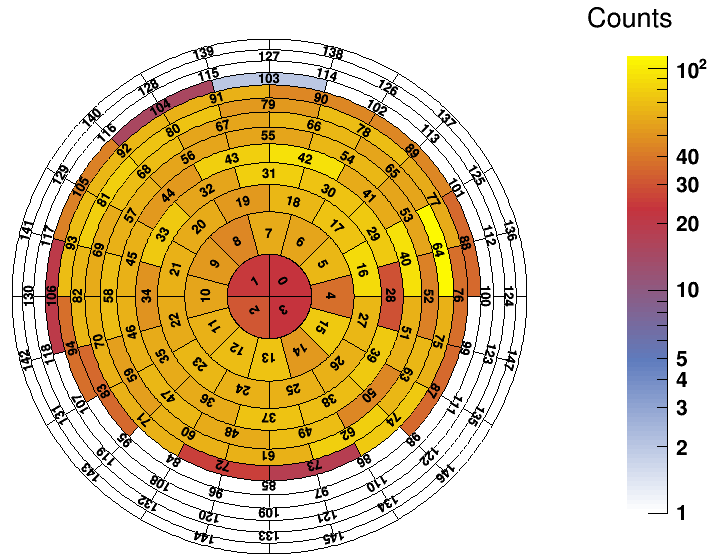


Figure 6.2.: Pixel view for the simulation of electrons generated on the rear wall. The lower part of the detector wafer indicates a blocking along the beamline. The lower rate on the bulls eye pixels occurs due to the rear wall hole.

illuminated area on the detector is shifted to the upper left. In the simulation the center of mass is at

$$\begin{aligned}\Delta x_{\text{simulated}} &= -0.85 \text{ mm} , \\ \Delta y_{\text{simulated}} &= 3.16 \text{ mm} .\end{aligned}\tag{6.2}$$

These shifts differ from the measured shifts in equation 6.1. This can be explained by the fact that in the measurement the rear wall might not have been illuminated homogeneously.

However on the bulls eye pixels a lower count rate can be observed. This can be explained by the rear wall hole, where no electrons were started. In the measurement this effect is not observed. A possible explanation is given by the geometry of the rear wall. UV light can

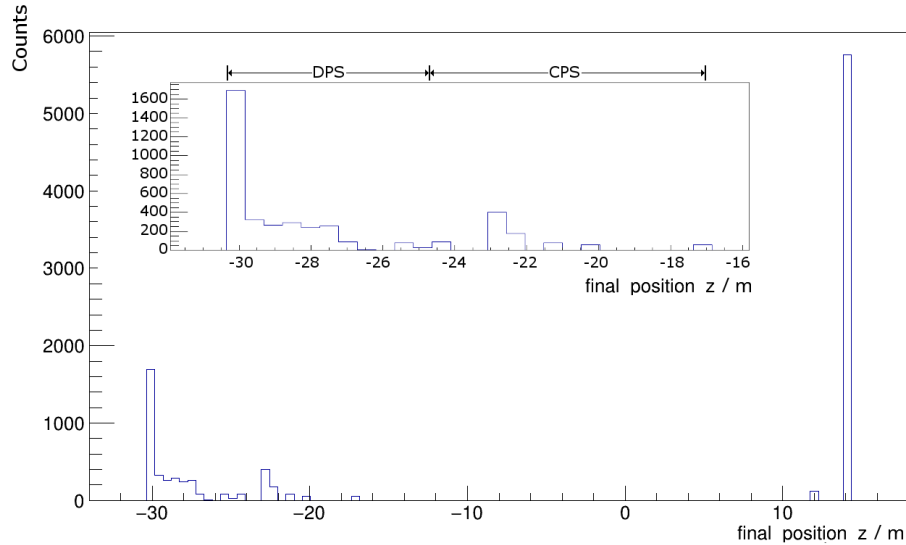


Figure 6.3.: Final z-positions of tracks from rear wall illumination simulation. Several collisions occur within the CPS and DPS.

Table 6.1.: Increasing count rates after ramping up CPS and DPS magnets from 20% to 30%. The CPS magnets can only be ramped up together.

magnet	count rate before ramping / cps	count rate after ramping / cps
CPS	62715 ± 112	64125 ± 113
DPS M5	65275 ± 81	65481 ± 85
DPS M4	65446 ± 81	66592 ± 86
DPS M3	66953 ± 86	67080 ± 82
DPS M2	67187 ± 86	68790 ± 83
DPS M1	68987 ± 88	69010 ± 88

penetrate the rear wall hole, where photo electrons are generated as well. In the simulation electrons were only started from the rear wall surface.

The simulation also provides data about the final z-position of the particle, when it was terminated and therefore about collision points throughout the beamline. Figure 6.3 shows a histogram with the final z-positions for the simulation of the rear wall illumination. The main peak located at $z \approx 14$ m represents the tracks that reached the detector. But additional collisions throughout the beamline can be observed. The first peak at $z \approx -30$ m is a sign for collisions in BT1 of the DPS. Additional collisions appear within all other DPS beamtubes, with a minimum in BT4, where only few (< 10) collisions are counted. Likewise collisions inside the CPS occur in beamtubes 1, 2, 3, 4 and 7. One more peak can be observed at $z \approx 12$ m, where the detector ILBV is located.

During a series of measurement the currents of the magnets throughout the beamline were increased starting at the detector side. During these measurements the count rate on the detector increased after ramping up the CPS and DPS magnets as shown in table 6.1. This indicated collisions inside the CPS and DPS as well. Thus, at this point measurement and simulation are in good agreement.

6.1.2. Elliott as an e-Gun

For the First Light measurement campaign the rear section electron gun was not ready for operation. Instead an ion source called ELIOTT (ELectron Impact IO n source To Test the

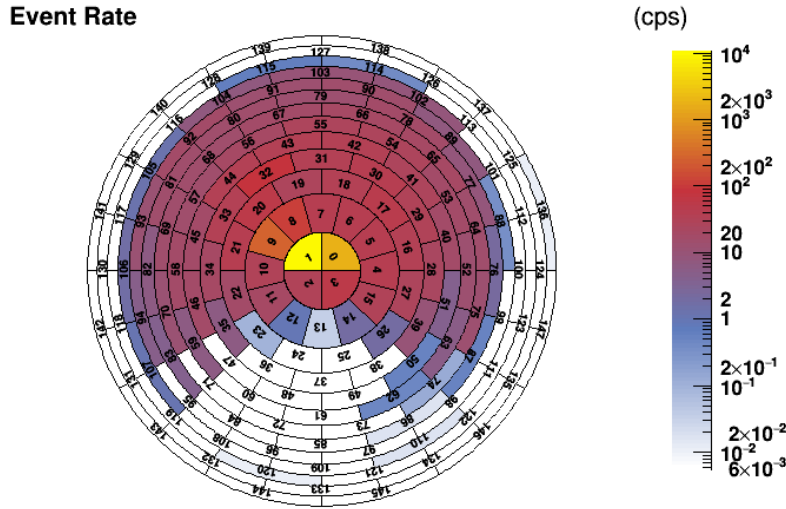


Figure 6.4.: Measurement of the electron pencil beam from ELIOTT. The hot spot on pixels 1 and 0 represent the true pin hole electrons. The halo occurs due to the fact that UV light originating from ionization processes can pass through the rear wall hole, get scattered back to the front side of the rear wall and produce photo electrons. The shadow on the lower pixels originates from a low energy blocking along the beamline (see section 6.3)

DPS) was installed behind the rear wall to shoot ions through the rear wall hole and to test the ion retention system along the beamline.

To generate the ions photons from a UV lamp (*Hamamatsu L10366*) are sent through a MgF_2 vacuum window. On this window a titanium and a gold layer are evaporated. In the gold layer UV photons get absorbed and photo electrons are emitted. The titanium/gold layer can be set on potential to accelerate the photo electrons. By sending these electrons through a gas, the gas atoms can get ionized. The produced ions are then accelerated by a negative potential while the negatively charged electrons are blocked at the same time. More detailed information about the ion mode of ELIOTT can be found in [Sac15].

During the First Light measurement campaign ELIOTT was also used as an electron gun. For this setup the photo electrons generated in the gold layer were accelerated towards the rear wall while no gas was injected into ELIOTT. In the following the electrons passing through the hole in the rear wall are called “pin hole electrons”, the resulting electron beam is called “pencil beam”.

In case of a perfectly aligned beamline the pin hole electrons should hit the four bulls eye pixels of the detector.

Figure 6.4 shows the results of the measurement with the pin hole electron beam from ELIOTT. As expected, the pixels in the bulls eye are hit by the beam. However the hot spot is shifted by

$$\begin{aligned}\Delta x_{\text{measured}} &= -1.8 \text{ mm} , \\ \Delta y_{\text{measured}} &= 3.3 \text{ mm}\end{aligned}\tag{6.3}$$

as determined by a center of mass analysis. Due to the fact that the electrons were guided through the full 70 m-long setup of the KATRIN experiment, this is a rather small deviation from the center of the detector wafer.

Again the implementations of the global KATRIN beamline and its misalignments in Kassiopia that were carried out in the context of this thesis (see chapter 5) were used to

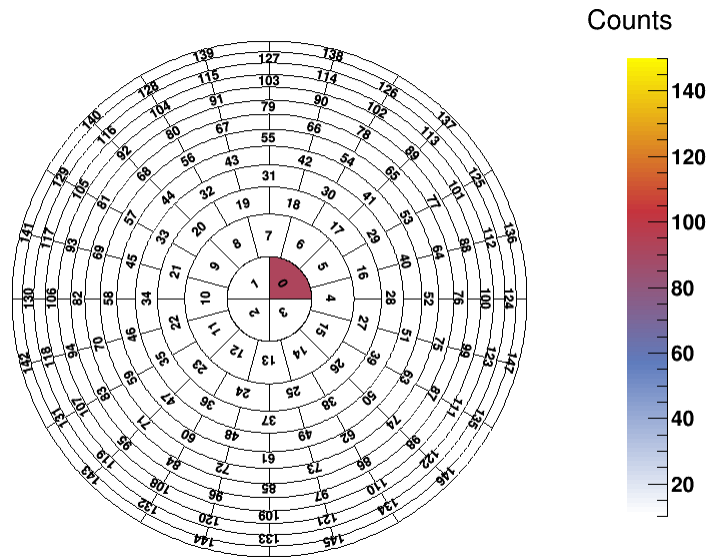


Figure 6.5.: Pixel view of the simulated pencil beam from ELIOTT.

simulate the electron pencil beam from ELIOTT with Kassiopeia. As a simplification the electrons were started on a circular plane behind the rear wall. The start radius was set in a range from 0 to 3 mm. Only electrons with radii small enough to pass through the hole in the rear wall were tracked to the detector while all others were terminated at the rear wall backside.

Figure 6.5 shows the result of the simulation. The center of mass on the wafer is at

$$\begin{aligned}\Delta x_{\text{simulated}} &= 3.1 \text{ mm} , \\ \Delta y_{\text{simulated}} &= 2.6 \text{ mm} .\end{aligned}\tag{6.4}$$

These values deviates significantly from the results of the measurement in equation 6.3.

This deviation can result from different tilts of the magnets in the simulation and in the experimental setup due to the large uncertainties of the alignment results reported in chapter 5. Especially a tilt or shift the RSCM cryostat and coil would have a large impact on the alignment results. The shifts and tilts of the RSCM coil relative to the cryostat have not been measured. Additionally the alignment of the rear wall relative to the rear wall chamber was unknown. A misalignment of the rear wall was found recently but could not be taken into account for simulations in context this thesis.

6.1.3. Dipole coils

During the First Light measurement campaign the dipole coils on the rear side the WGTS could be used to shift the magnetic fluxtube in x- and y-direction. With the implementations of the dipole coils in Kassiopeia the same is possible in simulations. Figure 6.6 shows an exemplary shift of the simulated electron pencil beam from ELIOTT by the dipole coils in x-direction.

In this measurement the beam was first shifted to hit all four bulls eye pixels. This was achieved with dipole currents of

$$\begin{aligned}I_x &= 0.6 \text{ A} , \\ I_y &= 2.0 \text{ A} .\end{aligned}\tag{6.5}$$

By varying one of the currents in steps of 2 A the beam was then shifted in x- or y-direction. During this measurement the WGTS magnets M2 and M3 were operated at 15 %, all other

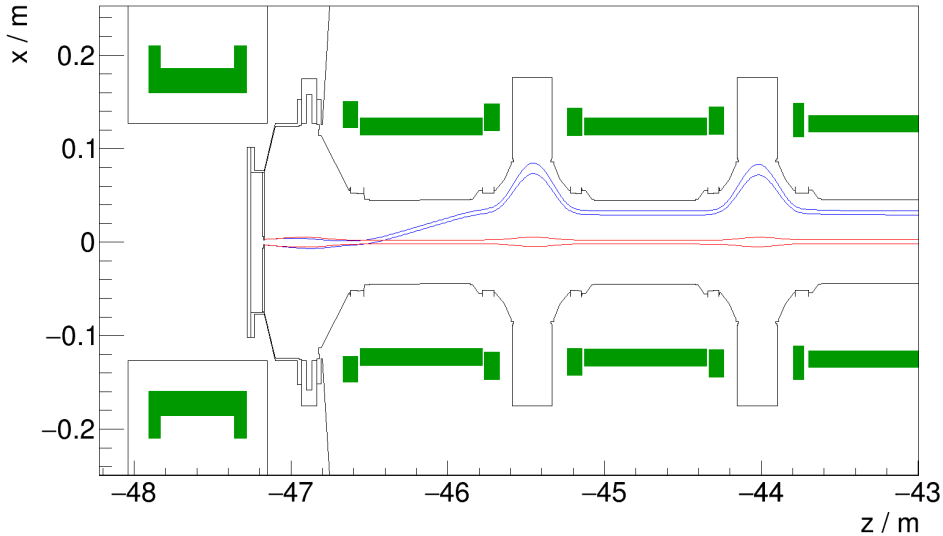


Figure 6.6.: Simulated fieldlines of shifted electron beam from pin hole. The red line shows the flux tube without shift, the blue line shows the fluxtube shifted by the DPS1-R dipole coil in x-direction.

magnets on 20 %. That creates a bottleneck inside the WGTS. When the pencil beam is shifted by the dipole coils, at some point it will hit the WGTS beamtube and disappear from the detector. Within the simulation the bottleneck was not considered.

The radius on the detector as a function of the dipole current was analyzed. The results of the measurements are shown in figure 6.7 for moving in x-direction from east to west and in figure 6.8 for moving the beam up and down. As expected linear behavior can be observed. The drop of values for higher absolute values of the current appears, since scattered electrons cause a halo when they hit the beamtube inside the WGTS and the pencil beam disappears from the detector. These values were excluded from the analysis.

This variation of the dipole current was also simulated to check the performance of the dipole coils in the simulation. The simulation was done twice, with and without including misalignments. The values for the dipole currents were set identical to the measurement. This causes an offset in the simulation without misalignments, since the beam is shifted out of the center. Figures 6.7 respectively 6.8 also show the analysis of the radii on the detector wafer in dependence of the dipole current for the simulations in x- and y-direction.

As in the measurement a linear behavior occurs. The equations of the linear regressions for measurement and simulations are listed in table 6.2.

A difference in the slopes for the x- and y-direction in the measured data is remarkable. It indicates a deviation of the as-built geometry from the design of the coils. In the simulation all coils have identical geometries. Also, compared to the measurement the slopes are bigger in the simulation. Simplifications in the dipole coil geometry are probably the cause for this discrepancy. It is recommended to use a corrective factor ξ for the dipole current with

$$\xi = \frac{a_{\text{measurement}}}{a_{\text{simulation}}} \quad (6.6)$$

where a_i is the slope of the linear regression and

$$I_{\text{simulation}} = \xi \cdot I_{\text{measurement}} \quad (6.7)$$

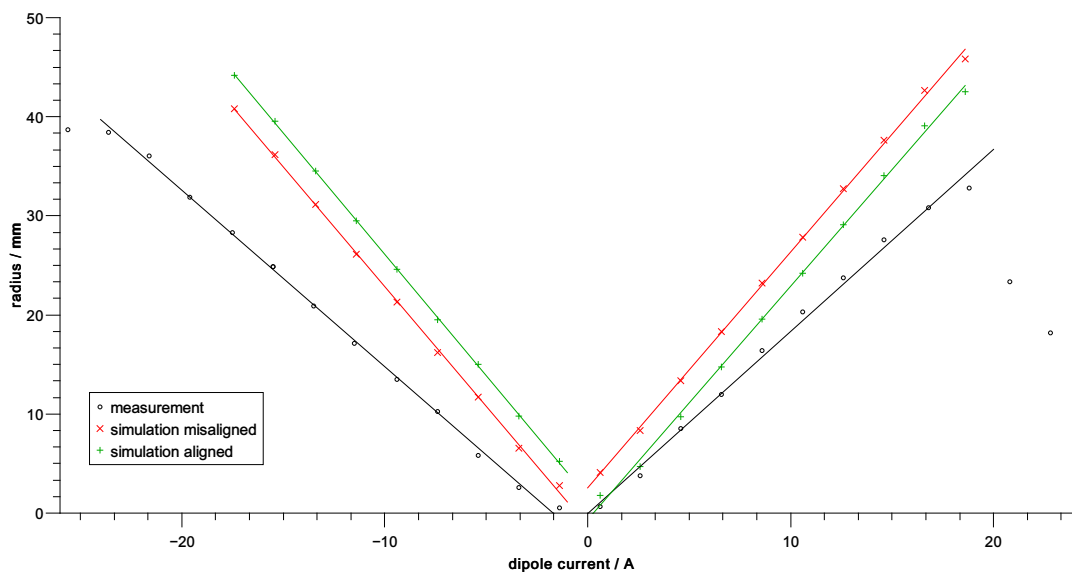


Figure 6.7.: Analysis of the shift of the pencil beam with dipole coil in x-direction. The current of the dipole coil in y-direction was set on 2.0 A to focus the beam on the center of the detector in the measurement. For the simulations the same current setting was used, causing an offset. For higher currents the radius drops, since the pencil beam disappears from the detector, but scattered electrons cause a halo. These values were excluded from the analysis.

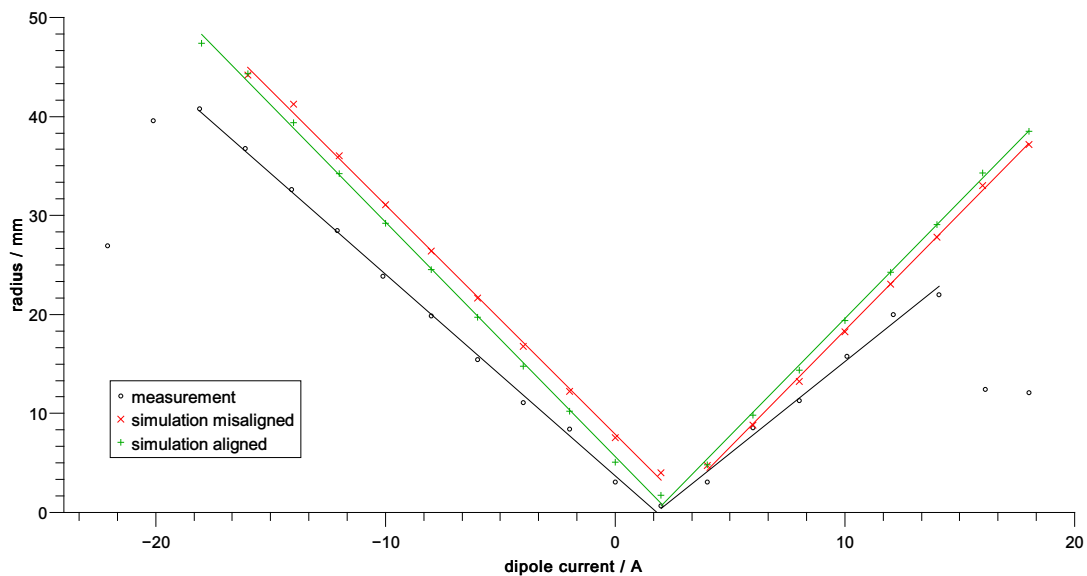


Figure 6.8.: Analysis of the shift of the pencil beam with dipole coil in y-direction. The current of the dipole coil in x-direction was set on 0.6 A to focus the beam on the center of the detector in the measurement. For the simulations the same current setting was used, causing an offset. For higher currents the radius drops, since the pencil beam disappears from the detector, but scattered electrons cause a halo. These values were excluded from the analysis.

Table 6.2.: Analysis of pencil beam movement east and west (x-direction) and up and down (y-direction) with DPS1-R dipole coils.

		negative current	positive current
x	measurement	$-1.8 \frac{\text{mm}}{\text{A}} \cdot I + 0.2 \text{ mm}$	$1.8 \frac{\text{mm}}{\text{A}} \cdot I$
	simulation without misalignment	$-2.4 \frac{\text{mm}}{\text{A}} \cdot I - 1.3 \text{ mm}$	$2.4 \frac{\text{mm}}{\text{A}} \cdot I + 2.5 \text{ mm}$
	simulation with misalignment	$-2.4 \frac{\text{mm}}{\text{A}} \cdot I + 2.1 \text{ mm}$	$2.4 \frac{\text{mm}}{\text{A}} \cdot I - 0.7 \text{ mm}$
y	measurement	$-2.1 \frac{\text{mm}}{\text{A}} \cdot I + 3.3 \text{ mm}$	$1.9 \frac{\text{mm}}{\text{A}} \cdot I - 3.6 \text{ mm}$
	simulation without misalignment	$-2.3 \frac{\text{mm}}{\text{A}} \cdot I - 7.9 \text{ mm}$	$2.4 \frac{\text{mm}}{\text{A}} \cdot I + 5.2 \text{ mm}$
	simulation with misalignment	$-2.4 \frac{\text{mm}}{\text{A}} \cdot I + 5.6 \text{ mm}$	$2.4 \frac{\text{mm}}{\text{A}} \cdot I - 4.1 \text{ mm}$

The values for corrective factors ξ_i for x- and y-direction calculated from the mean absolute values of the slopes from simulation and measurement are

$$\xi_x = 0.75 \quad (6.8)$$

and

$$\xi_y = 0.842 \quad (6.9)$$

By including these factors the simplifications in the geometries can be used and differences of the coils in x- and y-direction are compensated.

6.2. Global Alignment

To reach the goal of the KATRIN experiment in terms of sensitivity, β electrons from the source within a 191 Tm^2 fluxtube have to be guided to the spectrometer. Additionally the positions inside the source where the β decay takes place defined the retarding potential. Hence for a later simulation based analysis of the experimental data from neutrino mass measurements a well understood alignment between the source and the detector is necessary. Therefore the alignment between the rear wall, the WGTS and the detector wafer was tested during the First Light measurement campaign.

6.2.1. RS-FPD Alignment

The alignment between the rear wall and the detector wafer was tested by analyzing the position of the pencil beam from ELIOTT on the detector wafer, as already described in section 6.1.2. The results of the analysis are shown in equations 6.3 for the measurement and in equation 6.4 for the simulation.

6.2.2. RS-WGTS Alignment

The alignment between RS and WGTS can be tested by analyzing the dipole currents at which the collisions inside the WGTS occurred (see sec. 6.1.3) during the measurement with the bottleneck. From the measured currents

$$\begin{aligned} I_{+x} &= 18.0 \text{ A} , & I_{-x} &= 19.4 \text{ A} , \\ I_{+y} &= 16.6 \text{ A} , & I_{-y} &= 21.2 \text{ A} , \end{aligned} \quad (6.10)$$

a shift of

$$\begin{aligned} \Delta x &= 0.8 \text{ mm} , \\ \Delta y &= 1.7 \text{ mm} \end{aligned} \quad (6.11)$$

was calculated [Hac17]. Since the bottleneck has not been simulated, a comparison of the simulation to the measurement is not possible. A repetition of the simulation was not performed, since the inclusion of the rear wall misalignment is recommended to get reliable results, but not possible yet.

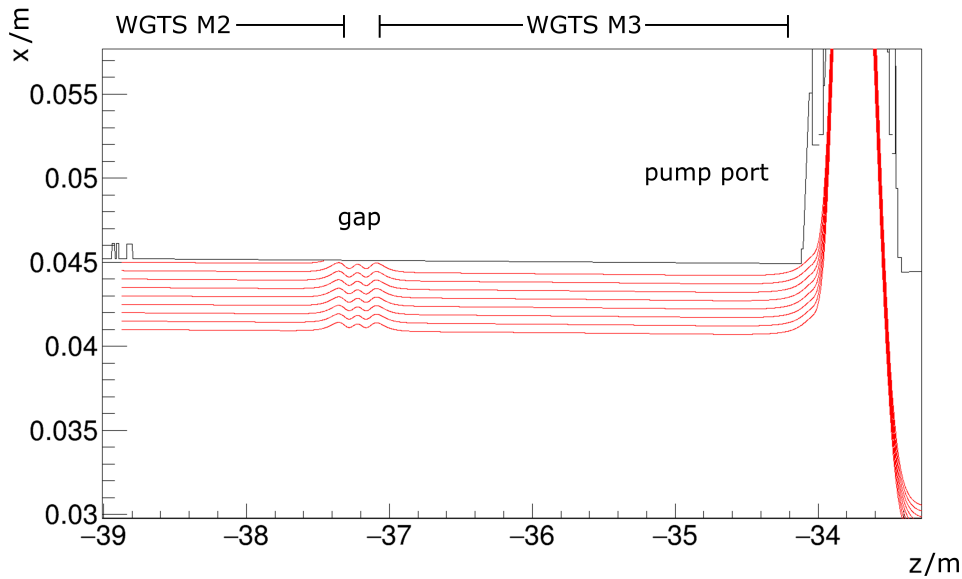


Figure 6.9.: Field lines inside the WGTS to investigate the narrow points at the gap between the WGTS magnets M2 and M3, and the pump port. The field lines shown in red represent different starting radii. For the analysis simulations with smaller distances between the starting radii were used.

6.2.3. WGTS-FPD Alignment

The WGTS-FPD alignment can be tested by analyzing the last illuminated pixels before the beam disappeared when the pencil beam was shifted by the dipole coils (see sec. 6.1.3). A misalignment between the WGTS center and detector center of

$$\begin{aligned}\Delta x &= 0.11 \text{ mm} , \\ \Delta y &= -1.61 \text{ mm} .\end{aligned}\tag{6.12}$$

was found [Hac17]. Just as in section 6.2.2 a comparison to the simulation is not possible and a reliable simulation can only be performed after including the rear wall alignment.

6.2.4. WGTS alignment simulations

The fluxtube inside the WGTS has a narrow point in the gap between WGTS M2 and WGTS M3 and at the pump port between M3 and M4. To investigate the fluxtube radius, for which collisions within the misaligned WGTS appear, simulations were run.

For these simulations, the currents of WGTS M2 and WGTS M3 were set on 15 %, all other magnets on 20 %. Electrons were started in the middle of WGTS M2 at $z = -38.87076$ m with different starting radii. Figure 6.9 shows a fieldline simulation illustrating the narrow points for several starting radii. For the analysis, 70 simulations were run each in positive and negative x-direction with starting radii in a range from $41 \text{ mm} \leq r \leq 48 \text{ mm}$ and 100 each in positive and negative y-direction with $41 \text{ mm} \leq r \leq 50 \text{ mm}$.

The simulations showed no collisions for start radii for

$$-43.75 \text{ mm} < r < 44.6 \text{ mm}\tag{6.13}$$

in x-direction and for

$$-45.4 \text{ mm} < r < 42.9 \text{ mm}\tag{6.14}$$

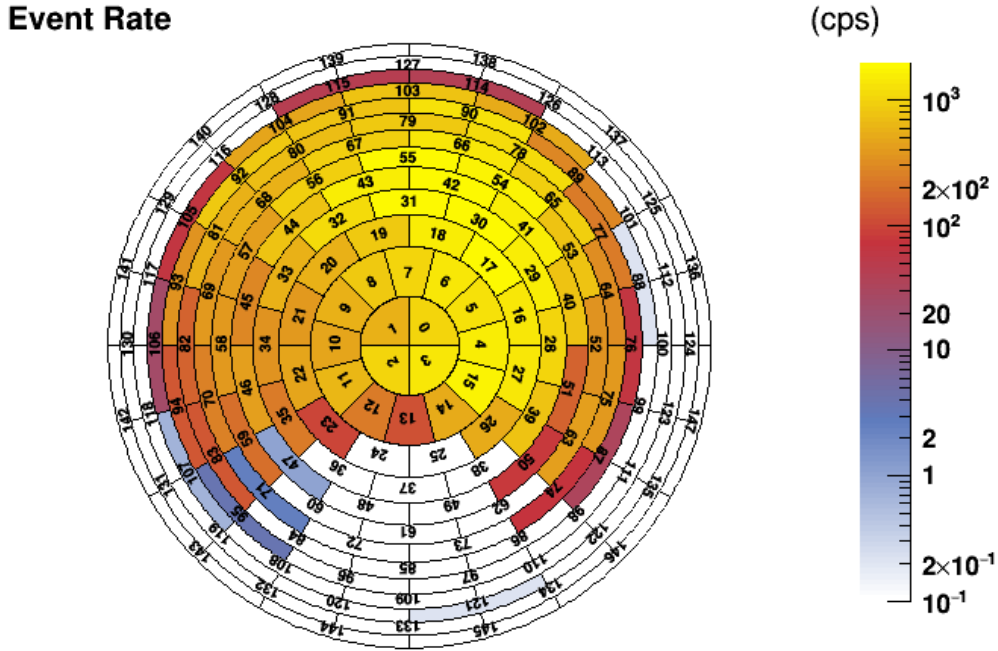


Figure 6.10.: Pixel view with low energy electrons from UV illumination of the rear wall. In this measurement the rear wall potential of -50 V. Compared to figure 6.1, where the same settings except the rear wall potential (-110 V) were used, a shadow appears.

in y -direction. That means that there are no collisions for a fluxtube with a radius of 42.2 mm, what corresponds to a 221 Tm² fluxtube. For the nominal 191 Tm² fluxtube, no collisions inside the WGTS are expected.

The center of the fluxtube area that has no collisions is at

$$\begin{aligned} x &= 0.425 \text{ mm} , \\ y &= -1.25 \text{ mm} . \end{aligned} \tag{6.15}$$

6.3. Low-Energy Blocking

As mentioned before, a shadow appeared on the detector wafer during the First Light measurement campaign.

At first a mechanical blocking was considered. If the PS ILBV was not completely open, it could reach into the fluxtube. This would fit the position of the shadow. But after a disassembly it turned out not to be the case.

A test with different rear wall potentials and therefore varying electron energies showed, that the shadow got smaller with increasing electron energy. An exemplary pixel view for a measurement with electrons from the UV illumination of rear wall is shown in figure 6.10. For this measurement the same settings were used except the rear wall potential of -50 V. A shadow on the lower part of the detector wafer is observed. At a rear wall potential of -110 V the shadow was almost disappeared as shown in figure 6.1. This behavior suggests an electrostatic effect.

To localize the position of the blocking the PS ILBV was set on different potential, while the rear wall potential was held constant. The shadow got smaller for increasing positive voltage, and bigger for increasing negative voltage. At a rear wall potential of -20 V and the ILBV on $+110$ V the shadow is no longer visible. The position of the shadow on the lower pixels was the same. That confirms the PS ILBV as source of the shadow.

However, a measurement of voltages inside the grounded ILBV showed, that all components were grounded. So the reason for the blocking is still not finally solved. A theory sees a magnetization of materials inside the ILBV as the cause of the blocking.

Simulations with Kassiopeia can offer valuable clues to the source of the blocking. At the moment electrostatic modeling of the ILBV is under way, and thereby simulation are in preparation.

Fortunately this low energy blocking will have no appreciable effect on the neutrino mass measurements since the energy of the electrons near the endpoint energy of $E_0 = 18.6$ keV that will be measured is much higher than the observed potential barrier.

7. Summary and Outlook

The Karlsruhe TRItium Neutrino (KATRIN) experiment aims to determine the effective mass of the electron anti-neutrino $m_{\bar{\nu}_e}$ in a model-independent way with a sensitivity of

$$m_{\nu} = 0.2 \text{ eV}/c^2 \text{ (90 \% C.L.)} . \quad (7.1)$$

After celebrating the KATRIN First Light event on October 14th 2016 an extended measurement campaign was carried out with the full 70 m long beamline. In this context the alignment of the global beamline was studied in detail. The alignment of the beamline is important the transport of β electrons from the tritium source to the spectrometer is essential to reach the goal in terms of sensitivity. Additionally simulations need to be compared to the measurements to study the positions of the decay inside the source. This is necessary to determine the retarding potential. The implementation of a full geometric model of the KATRIN beamline into the simulation software package Kassiopeia was the main focus of the thesis.

The implemented geometry model contains all beamtube and magnet elements of the full KATRIN beamline. A feature of the new geometry structure is the ability to perform shifts and tilts for each element. This allows to include alignment data from different measurement techniques like mechanical alignment and magnetic field measurements to the simulation. The user access to the alignment data is made as user friendly as possible. By defining the phase of the measurement that is to be simulated, matching data for each component can be accessed. This will be important to get information from later simulations about the source in the experiment.

During the First Light measurement campaign several alignment measurements were carried out. For this purpose two electron sources were available on the rear side of the experimental beamline: Firstly low-energy electrons could be generated across the full magnetic flux tube via the photoelectric effect on ultraviolet (UV) illuminated the rear wall of the source. Secondly an ion source called ELIOTT could be alienated to generate an electron pencil beam. The latter could be moved across the flux tube by two magnetic dipole coils located at the rear part of the source cryostat. In this thesis, both types of electron sources were simulated with comparable settings and by using the full KATRIN beamline model as implemented in Kassiopeia. For the simulation of the UV illumination the pixel distributions on the detector was in good agreement with the measurement. However, a center of mass analysis delivered different results due to a inhomogeneous UV illumination in the experiment. In the simulation the shift of the pencil beam on the detector wafer differed from the measurement:

$$\begin{aligned} \Delta x_{\text{measured}} &= -1.8 \text{ mm} , & \Delta x_{\text{simulated}} &= 3.1 \text{ mm} , \\ \Delta y_{\text{measured}} &= 3.3 \text{ mm} , & \Delta y_{\text{simulated}} &= 2.6 \text{ mm} . \end{aligned} \quad (7.2)$$

This deviation most likely occurs due to uncertainties on the alignment of magnet and beamtube elements along the beamline, that can not be taken into account within the simulations.

Global alignment measurements were performed during the First Light measurement campaign showing misalignments between the rear end of the experiment, the source and the detector. Reliable simulation were not yet possible due to a recently found misalignment of the rear wall, that could not be taken into account for this thesis. Further simulations are recommended after this misalignment is included within Kassiopeia.

The geometry model also needs to be extended to cover electrostatic calculations. This is for instance important to study an electrostatic blocking that was observed during First Light. Future simulation based studies are prepared to solve it. However this blocking will not have an influence on neutrino mass measurements since the blocking only appears for much lower electron energies.

In a next step the storage of the alignment data will be moved to a database. In this way, only a timestamp or run number will be needed to access the proper geometries for a simulation.

Appendix

A. Pinch Magnet Field Measurements

On the next pages, the measured values for the pinch magnet coil alignment are listed. Different magnetic fields in the pinch magnet and the detector magnet were set:

- pinch magnet on 0 T and detector magnet on 1.8 T,
- pinch magnet on 3 T and detector magnet on 1.8 T,
- pinch magnet on 3 T and detector magnet on 0 T and
- pinch magnet on 0 T and detector magnet on 0 T.

For each setting the magnetic field was measured on the upstream and the downstream side of the cryostat with top and bottom orientation of the hall probe.

Table A.1.: Pinch Magnet: 0 T; Detector Magnet: 1.8 T; upstream side of the pinch magnet cryostat

ϕ in $^\circ$	top			bottom		
	B_x in T	B_y in mT	B_z in T	B_x in T	B_y in mT	B_z in T
0.0	-0.0002	-0.0026	-0.0077	-0.00010	-0.0082	-0.0077
22.5	-0.0002	-0.0217	-0.0077	-0.00015	-0.0261	-0.0077
45.0	-0.0002	-0.0446	-0.0077	-0.00015	-0.0481	-0.0077
67.5	-0.0002	-0.0640	-0.0077	-0.00020	-0.0648	-0.0077
90.0	-0.0002	-0.0733	-0.0077	-0.00020	-0.0733	-0.0077
112.5	-0.0002	-0.0738	-0.0077	-0.00020	-0.0728	-0.0077
135.0	-0.0002	-0.0662	-0.0077	-0.00030	-0.0635	-0.0077
157.5	-0.0002	-0.0501	-0.0077	-0.00030	-0.4580	-0.0077
180.0	-0.0003	-0.0222	-0.0077	-0.00030	-0.0205	-0.0077
202.5	-0.0003	-0.0073	-0.0077	-0.00030	-0.0073	-0.0077
225.0	-0.0003	0.0274	-0.0077	-0.00030	0.0261	-0.0077
247.5	-0.0002	0.0391	-0.0077	-0.00020	0.0379	-0.0077
270.0	-0.0002	0.0464	-0.0077	-0.00020	0.0433	-0.0077
292.5	-0.0002	0.0454	-0.0077	-0.00020	0.0389	-0.0077
315.0	-0.0002	0.0352	-0.0077	-0.00020	0.0266	-0.0077
337.5	-0.0002	0.0172	-0.0077	-0.00015	0.0088	-0.0077
360.0	-0.0002	0.0022	-0.0077	-0.00015	0.0085	-0.0077

Table A.2.: Pinch Magnet: 0 T; Detector Magnet: 1.8 T; downstream side of the pinch magnet cryostat

ϕ in $^\circ$	top			bottom		
	B_x in T	B_y in mT	B_z in T	B_x in T	B_y in mT	B_z in T
0.0	-0.0049	0.5882	0.0394	-0.0046	0.5835	0.03950
22.5	-0.0050	0.6925	0.0394	-0.0047	0.6915	0.03940
45.0	-0.0050	0.7765	0.0394	-0.0046	0.7724	0.03940
67.5	-0.0049	0.8150	0.0394	-0.0046	0.8002	0.03950
90.0	-0.0049	0.8171	0.0395	-0.0046	0.8085	0.03950
112.5	-0.0049	0.8386	0.0395	-0.0046	0.8191	0.03950
135.0	-0.0049	0.8697	0.0395	-0.0046	0.8384	0.03955
157.5	-0.0049	0.9402	0.0396	-0.0046	0.9079	0.03960
180.0	-0.0048	0.9270	0.0396	-0.0045	0.9066	0.03960
202.5	-0.0047	0.9015	0.0396	-0.0044	0.8941	0.03960
225.0	-0.0047	0.8668	0.0396	-0.0044	0.8623	0.03970
247.5	-0.0046	0.7718	0.0397	-0.0043	0.7793	0.03970
270.0	-0.0045	0.6830	0.0397	-0.0043	0.6632	0.03970
292.5	-0.0046	0.4891	0.0396	-0.0044	0.5579	0.03960
315.0	-0.0051	0.4786	0.0395	-0.0045	0.5069	0.03960
337.5	-0.0051	0.5265	0.0398	-0.0046	0.5302	0.03950
360.0	-0.0051	0.6175	0.0394	-0.0046	0.6602	0.03950

Table A.3.: Pinch Magnet: 3 T; Detector Magnet: 1.8 T; upstream side of the pinch magnet cryostat

	top			bottom		
ϕ in $^\circ$	B_x in T	B_y in mT	B_z in T	B_x in T	B_y in mT	B_z in T
0.0	-0.1647	21.257	-0.7096	-0.1644	20.633	-0.7096
22.5	-0.1641	22.202	-0.7099	-0.1638	21.394	-0.7099
45.0	-0.1633	22.585	-0.7105	-0.1633	21.841	-0.7103
67.5	-0.1628	22.599	-0.7108	-0.1631	21.949	-0.7105
90.0	-0.1623	22.160	-0.7111	-0.1625	21.942	-0.7109
112.5	-0.1619	21.615	-0.7114	-0.1621	21.659	-0.7112
135.0	-0.1614	21.210	-0.7118	-0.1615	21.325	-0.7117
157.5	-0.1615	20.650	-0.7116	-0.1615	20.854	-0.7116
180.0	-0.1613	20.109	-0.7118	-0.1612	20.660	-0.7118
202.5	-0.1616	19.501	-0.7114	-0.1613	20.343	-0.7116
225.0	-0.1618	19.254	-0.7112	-0.1619	19.899	-0.7111
247.5	-0.1629	18.910	-0.7105	-0.1629	19.267	-0.7106
270.0	-0.1634	18.776	-0.7101	-0.1635	19.024	-0.7102
292.5	-0.1639	18.899	-0.7100	-0.1639	18.617	-0.7100
315.0	-0.1647	19.303	-0.7095	-0.1648	19.288	-0.7096
337.5	-0.1647	20.090	-0.7096	-0.1652	19.985	-0.7095
360.0	-0.1646	21.234	-0.7097	-0.1653	21.059	-0.7095

Table A.4.: Pinch Magnet: 3 T; Detector Magnet: 1.8 T; downstream side of the pinch magnet cryostat

	top			bottom		
ϕ in $^\circ$	B_x in T	B_y in mT	B_z in T	B_x in T	B_y in mT	B_z in T
0.00	0.1662	-14.345	0.7534	0.1666	-12.915	0.7534
22.5	0.1666	-15.005	0.7535	0.1670	-13.910	0.7534
45.0	0.1663	-15.765	0.7537	0.1668	-14.523	0.7537
67.5	0.1662	-16.668	0.7539	0.1662	-15.371	0.7540
90.0	0.1653	-17.365	0.7541	0.1653	-15.931	0.7542
112.5	0.1635	-17.207	0.7545	0.1646	-16.200	0.7544
135.0	0.1630	-16.713	0.7546	0.1637	-15.857	0.7547
157.5	0.1629	-16.152	0.7548	0.1633	-14.982	0.7547
180.0	0.1628	-15.487	0.7548	0.1630	-14.374	0.7550
202.5	0.1625	-14.969	0.7550	0.1624	-14.145	0.7550
225.0	0.1625	-14.142	0.7550	0.1628	-13.092	0.7550
247.5	0.1634	-13.715	0.7546	0.1635	-12.693	0.7547
270.0	0.1639	-13.444	0.7543	0.1640	-12.377	0.7544
292.5	0.1648	-12.837	0.7536	0.1642	-12.190	0.7542
315.0	0.1650	-13.430	0.7538	0.1645	-12.071	0.7539
337.5	0.1653	-13.587	0.7536	0.1656	-12.264	0.7571
360.0	0.1663	-14.046	0.7534	0.1663	-12.824	0.7535

Table A.5.: Pinch Magnet: 3 T; Detector Magnet: 0 T; upstream side of the pinch magnet cryostat

	top			bottom		
ϕ in $^\circ$	B_x in T	B_y in mT	B_z in T	B_x in T	B_y in mT	B_z in T
0.00	-0.1659	21.302	-0.7016	-0.1673	20.859	-0.7013
22.5	-0.1653	22.204	-0.7020	-0.1669	21.688	-0.7016
45.0	-0.1649	22.571	-0.7024	-0.1665	22.034	-0.7018
67.5	-0.1644	22.564	-0.7027	-0.1661	22.228	-0.7022
90.0	-0.1638	22.328	-0.7031	-0.1655	22.149	-0.7026
112.5	-0.1634	21.770	-0.7035	-0.1650	21.767	-0.7030
135.0	-0.1630	21.100	-0.7037	-0.1645	21.398	-0.7033
157.5	-0.1631	20.650	-0.7036	-0.1642	21.069	-0.7034
180.0	-0.1633	20.568	-0.7034	-0.1643	20.804	-0.7033
202.5	-0.1633	20.211	-0.7033	-0.1644	20.410	-0.7032
225.0	-0.1633	19.562	-0.7031	-0.1649	19.779	-0.7026
247.5	-0.1643	19.167	-0.7025	-0.1650	19.349	-0.7025
270.0	-0.1649	19.048	-0.7020	-0.1654	19.001	-0.7022
292.5	-0.1655	19.087	-0.7017	-0.1660	18.833	-0.7019
315.0	-0.1661	19.646	-0.7015	-0.1665	18.994	-0.7016
337.5	-0.1660	20.336	-0.7015	-0.1672	19.645	-0.7013
360.0	-0.1661	21.370	-0.7016	-0.1673	20.892	-0.7013

Table A.6.: Pinch Magnet: 3 T; Detector Magnet: 0 T; downstream side of the pinch magnet cryostat

	top			bottom		
ϕ in $^\circ$	B_x in T	B_y in mT	B_z in T	B_x in T	B_y in mT	B_z in T
0.00	0.1658	-13.057	0.7137	0.1686	-12.788	0.7131
22.5	0.1658	-14.200	0.7140	0.1689	-13.511	0.7132
45.0	0.1660	-15.028	0.7142	0.1687	-14.446	0.7134
67.5	0.1655	-16.031	0.7143	0.1679	-15.294	0.7136
90.0	0.1649	-16.643	0.7145	0.1679	-15.869	0.7138
112.5	0.1637	-16.700	0.7147	0.1668	-16.005	0.7140
135.0	0.1628	-16.235	0.7149	0.1660	-15.707	0.7142
157.5	0.1620	-15.370	0.7150	0.1649	-14.303	0.7142
180.0	0.1622	-14.970	0.7150	0.1651	-13.734	0.7140
202.5	0.1622	-14.695	0.7149	0.1648	-13.982	0.7144
225.0	0.1634	-14.173	0.7147	0.1650	-13.109	0.7144
247.5	0.1642	-13.551	0.7144	0.1655	-12.580	0.7141
270.0	0.1647	-13.273	0.7141	0.1662	-12.196	0.7137
292.5	0.1652	-13.040	0.7139	0.1669	-11.895	0.7134
315.0	0.1651	-12.912	0.7138	0.1652	-11.673	0.7138
337.5	0.1655	-12.690	0.7138	0.1662	-11.778	0.7134
360.0	0.1664	-13.115	0.7136	0.1667	-12.792	0.7135

Table A.7.: Pinch Magnet: 0 T; Detector Magnet: 0 T; upstream side of the pinch magnet cryostat

	top			bottom		
ϕ in $^\circ$	B_x in μT	B_y in μT	B_z in μT	B_x in μT	B_y in μT	B_z in μT
0.00	19	153	-20	17	153	-19
22.5	28	153	-19	26	153	-20
45.0	39	150	-19	37	152	-20
67.5	50	143	-19	48	144	-20
90.0	58	130	-19	56	132	-20
112.5	60	114	-20	58	114	-19
135.0	54	97	-20	53	98	-19
157.5	42	83	-20	41	84	-19
180.0	23	75	-20	23	76	-19
202.5	2	78	-20	2	78	-19
225.0	-14	91	-21	-15	91	-20
247.5	-21	108	-22	-21	108	-21
270.0	-21	125	-22	-22	124	-21
292.5	-14	139	-21	-15	139	-21
315.0	-4	148	-20	-5	148	-20
337.5	8	152	-20	6	153	-19
360.0	18	153	-19	16	153	-19

Table A.8.: Pinch Magnet: 0 T; Detector Magnet: 0 T; downstream side of the pinch magnet cryostat

	top			bottom		
ϕ in $^\circ$	B_x in μT	B_y in μT	B_z in μT	B_x in μT	B_y in μT	B_z in μT
0.00	-45	-54	307	-55	-55	307
22.5	15	-72	301	16	-72	302
45.0	53	-111	294	54	-112	293
67.5	68	-158	287	68	-158	287
90.0	64	-205	280	64	-205	282
112.5	45	-239	277	44	-240	277
135.0	15	-262	275	15	-262	275
157.5	-11	-273	273	-14	-275	274
180.0	-30	-277	267	-35	-278	268
202.5	-58	-277	257	-59	-276	259
225.0	-83	-269	252	-85	-267	254
247.5	-109	-256	250	-110	-255	250
270.0	-139	-230	251	-140	-230	254
292.5	-160	-187	263	-161	-188	263
315.0	-157	-126	283	-158	-131	283
337.5	-115	-74	301	-116	-81	301
360.0	-50	-54	306	-50	-62	307

Bibliography

- [AAA16a] R. Adam, P. A. R. Ade, N. Aghanim et al., “Planck2015 results: I. Overview of products and scientific results”, *Astronomy & Astrophysics*, vol. 594, 2016, DOI: <http://dx.doi.org/10.1051/0004-6361/201527101>.
- [AAA16b] R. Adam, P. A. R. Ade, N. Aghanim et al., “Planck 2015 results: XIII. Cosmological parameters”, *Astronomy & Astrophysics*, vol. 594, 2016, DOI: <http://dx.doi.org/10.1051/0004-6361/201525830>.
- [AAB17] M. Agostini, M. Allardt, A. M. Bakalyarov et al. (The GERDA Collaboration), “Background-free search for neutrinoless double- β decay of ^{76}Ge with GERDA”, *Nature*, vol. 544, pp. 47–52, 2017, doi:10.1038/nature21717.
- [ABB16] M. Arenz, M. Babutzka, M. Bahr et al., “Commissioning of the vacuum system of the KATRIN Main Spectrometer”, *J. Inst.*, 11(04):P04011–P04011, 2016, DOI: <http://dx.doi.org/10.1088/1748-0221/11/04/P04011>.
- [Abe08] S. Abe et al. (The KamLAND Collaboration), “Precision Measurement of Neutrino Oscillation Parameters with KamLAND”, *Phys. Rev. Lett.*, vol. 100, p. 221803, 2008, DOI: 10.1103/PhysRevLett.100.221803.
- [Abe11] K. Abe et al. (T2K Collaboration), “Indication of Electron Neutrino Appearance from an Accelerator-Produced Off-Axis Muon Neutrino Beam”, *Phys. Rev. Lett.*, vol. 107, p. 041801, 2011, DOI: 10.1103/PhysRevLett.107.041801.
- [Abe12] Y. Abe et al. (Double Chooz Collaboration), “Reactor ν_e disappearance in the Double Chooz experiment”, *Phys. Rev. D*, vol. 86, p. 052008, 2012, DOI: 10.1103/PhysRevD.86.052008.
- [Ack13] K. Ackermann et al. (GERDA Collaboration), “The Gerda experiment for the search of $0\nu\beta\beta$ decay in ^{76}Ge ”, *The European Physical Journal C*, vol. 73, p. 2330, 2013, DOI: 10.1140/epjc/s10052-013-2330-0.
- [Ada15] Birgit Adams, “Untersuchung magnetischer Materialien und Inbetriebnahme der Magnetfeldüberwachung am KATRIN-Hauptspektrometer”, *Karlsruhe Institute of Technology*, master thesis, 2015.
- [Ahn02] Q. R. Ahmad, “Direct Evidence for Neutrino Flavor Transformation from Neutral Current Interactions in the Sudbury Neutrino Observatory”, *Phys. Rev. Lett.*, vol. 89, no.1, 2002, DOI: 10.1103/PhysRevLett.89.011301.
- [Ahn12] J. K. Ahn et al. (RENO Collaboration), “Observation of Reactor Electron Antineutrinos Disappearance in the RENO Experiment”, *Phys. Rev. Lett.*, vol. 108, p. 191802, 2012, DOI: 10.1103/PhysRevLett.108.191802.
- [Ams15] J. F. Amsbaugh et al., “Focal-plane detector system for the KATRIN experiment”, arXiv:1404.2925 [physics.ins-det], 2015. DOI: 10.1016/j.nima.2014.12.116.

- [An 13] F. P. An et al. (Daya Bay Collaboration), “Improved measurement of electron antineutrino disappearance at Daya Bay”, *Chinese Physics C*, vol. 37, no. 1, p. 011001, 2013, DOI: 10.1088/1674-1137/37/1/011001.
- [Ang05] J. Angrik et al., “KATRIN Design Report 2005”, *FZKA Scientific Report 7090*, 2005.
- [Ase11] V. N. Aseev et al., “Upper limit on electron antineutrino mass from Troitsk experiment”, *Phys. Rev. D*, vol 84, no. 11, p 112003, 2011, DOI: 10.1103/PhysRevD.84.112003.
- [Bab12] Martin Babutzka et al., “Monitoring of the operating parameters of the KATRIN Windowless Gaseous Tritium Source”, *New Journal of Physics*, vol. 14, p. 103046, 2012, DOI: 10.1088/1367-2630/14/10/103046.
- [Bah64a] John N. Bahcall, “Solar Neutrino Cross Sections and Nuclear Beta Decay”, *Phys. Rev. Lett.*, vol. 135, no. 1B, pp. B137 - B146, 1964, DOI: 10.1103/PhysRevLett.135.B137.
- [Bah64b] John N. Bahcall, “Solar Neutrinos. I. Theoretical”, *Phys. Rev. Lett.*, vol. 12, no.11, pp. 300 - 302, 1964, DOI: 10.1103/PhysRevLett.12.300.
- [Bah05] John N. Bahcall et al., “New Solar Opacities, Abundances, Helioseismology, and Neutrino Fluxes”, *The Astrophysical Journal Letters*, vol. 621, no. 1, p. 621, 2005, DOI: 10.1086/428929.
- [BD76] John N. Bahcall, Raymond Davis, Jr., “Solar Neutrinos: A Scientific Puzzle”, *Science*, vol. 191, pp. 264 - 267, 1976. [Online]. Available: <https://www.bnl.gov/bnlweb/raydavis/Science-01-23-76.pdf>.
- [BDP87] John N. Bahcall, Arnon Dar, Tsvi Piran, “Neutrinos and neutrino mass from a supernova”, *Nature*, vol. 326, pp. 135 - 136, 1987. [Online]. Available: <http://www.nature.com/physics/looking-back/bahcall/Bahcall.pdf>
- [Ber13] Juerg Beringer et al., (Particle Data Group), “010001 (2012) and 2013 partial update for the 2014 edition”, *Phys. Rev. D.*, vol. 86, no. 010001, 2013. [Online]. Available: <http://pdg.lbl.gov>
- [BG06] Lars Bergström and Ariel Goobar, “Cosmology and Particle Astrophysics”, *Springer*, 2006.
- [Bio87] R. M. Bionta et al., “Observation of a Neutrino Burst in Coincidence with Supernova 1987A in Large Magellanic Cloud”, *Phys. Rev. Lett.*, vol. 58, p. 1494, 1987, DOI: 10.1103/PhysRevLett.58.1494.
- [BPT80] G. Beamson, H. Q. Porter and D. W. Turner, “The collimating and magnifying properties of a superconducting field photoelectron spectrometer”, *Journal of Physics E: Scientific Instruments*, vol. 13, no. 1, p. 64, 1980, DOI: 10.1038/133532a0.
- [BR96] Rene Brun and Fons Rademakers, “ROOT - An Object Oriented Data Analysis Framework”, Proceedings AIHENP’96 Workshop, Lausanne, Sep. 1996, *Nucl. Inst. & Meth. in Phys. Res. A* 389 (1997) 81-86. See also <http://root.cern.ch/>.
- [Cha14] James Chadwick, “Intensitätsverteilung im magnetischen Spektrum der β -Strahlen von Radium B + C / The Intensity Distribution in Magnetic Spectrum of β -Rays of Radium B + C”, *Verhandl. Dtsch. phy. Ges.*, vol 16, p. 383, 1914.
- [Cow56] Clyde L. Cowan, Frederic B. Harrison, Herald W. Kruse, A. D. McGuire, “Detection of the Free Neutrino: a Confirmation”, *Science*, vol. 124, no. 3212, pp. 103 - 104, 1956, DOI: 10.1126/science.124.3212.103.

- [Dan62] Gordon T. Danby, Jean-Marie Gaillard, Konstantin A. Goulianos, Leon Max Lederman, Nari B. Mistry, Melvin Schwartz, Jack Steinberger, “Observation of High-Energy Neutrino Reactions and the Existence of Two Kinds of Neutrinos”, *Phys. Rev. Lett.*, vol. 9, no. 1, pp. 36 - 44, 1962, DOI: 10.1103/PhysRevLett.9.36.
- [Dav64] Raymond Davis, Jr., “Solar Neutrinos. II. Experimental”, *Phys. Rev. Lett.*, vol. 12, no.11, pp. 303 - 305, 1964, DOI: 10.1103/PhysRevLett.12.303.
- [DEC79] Raymond Davis, Jr., J. C. Evans, B. T. Cleveland, “The Solar Neutrino Problem”, *AIP Conf. Proc.*, vol. 52, no. 17, 1979, DOI: 10.1063/1.31802.
- [DHH68] Raymond Davis, Jr., Don S. Harmer, Kenneth C. Hoffman, “Search for Neutrinos from the Sun”, *Phys. Rev. Lett.*, vol. 20, no. 21, pp. 1205 - 1209, 1968, DOI: 10.1103/PhysRevLett.20.1205.
- [DKT85] M. Doi, T. Kotani, and E. Takasugi, “Double Beta Decay and Majorana Neutrino”, *Progress of Theoretical Physics Supp*, vol. 83, pp. 1 - 175, 1985, DOI: 10.1143/PTPS.83.1.
- [DON01] DONUT Collaboration, “Observation of Tau Neutrino Interactions”, *Phys. Lett. B*, vol. 594, no. 3, pp. 218 - 224, 2001, DOI: 10.1016/S0370-2693(01)00307-0.
- [Dre13] Guido Drexlin, V. Hannen, S. Mertens, C. Weinheimer, “Current Direct Neutrino Mass Experiments”, *Advances in High Energy Physics*, p. 293986, 2013, DOI: 10.1155/2013/293986.
- [Erh16] Moritz Erhard, “Influence of the magnetic field on the transmission characteristics and the neutrino mass systematic of the KATRIN experiment”, *Karlsruhe Institute of Technology*, Ph.D. thesis, 2016.
- [EV02] Steven R. Elliott, Petr Vogel, “Double Beta Decay”, *Annual Review of Nuclear and Particle Science*, vol. 52, pp. 115 - 151, 2002, DOI: 10.1146/annurev.nucl.52.050102.090641.
- [Fer34] Enrico Fermi, “Versuch einer Theorie der β -Strahlen. I”, *Zeitschrift für Physik*, vol. 88, no. 3 - 4, pp. 161 - 177, 1934, DOI: 10.1007/BF01351864.
- [FGT17] Daniel Furse, Stefan Groh, Nikolaus Trost et al., “Kassiopeia: A modern, extensible C++ particle tracking package”, *New Journal of Physics*, 2017, DOI: <https://doi.org/10.1088/1367-2630/aa6950>.
- [FN28] Ralph Howard Fowler and Lothar Nordheim, “Electron Emission in Intense Electric Fields”, *Proc. R. Soc. Lond. A*, vol. 119, no. 781, pp. 173 - 181, 1928, DOI: 10.1098/rspa.1928.0091.
- [Fra10] Florian Fränkle, “Background Investigations of the KATRIN Pre-Spectrometer”, *Karlsruhe Institute of Technology*, Ph.D. thesis, 2010.
- [Fuk96] Y. Fukuda et al. (Kamikande Collaboration), “Solar Neutrino Data Covering Solar Cycle 22”, *Phys. Rev. Lett.*, vol.77, pp. 1683 - 1686, 1996, DOI: 10.1103/PhysRevLett.77.1683.
- [Fuk98] Y. Fukuda et al. (Super-Kamikande Collaboration), “Measurements of the Solar Neutrino Flux from Super-Kamiokande’s First 300 Days”, *Phys. Rev. Lett.*, vol. 81, p. 1158, 1998, DOI: 10.1103/PhysRevLett.81.1158.
- [Fuk01] S. Fukuda et al. (Super-Kamiokande Collaboration), “Solar 8 B and hep Neutrino Measurements from 1258 Days of Super-Kamiokande Data”, *Phys. Rev. Lett.*, vol. 86, p. 5651, 2001, DOI: 10.1103/PhysRevLett.86.5651.

- [Gal12] M. Galeazzi, F. Gatti, M. Lusignoli, A. Nucciotti, S. Ragazzi, M. R. Gomes, “The Electron Capture Decay of ^{163}Ho to Measure the Electron Neutrino Mass with sub-eV Accuracy (and Beyond)”, 2012, arXiv:1202.4763v3.
- [Gas14] L. Gastaldo et al., “The Electron Capture ^{163}Ho Experiment ECHO”, *Journal of Low Temperature Physics*, vol. May 2014, 2014, DOI: 10.1007/s10909-014-1187-4.
- [Gat99] F. Gatti et al., “Detection of environmental fine structure in the low-energy beta-decay spectrum of Re-187”, *Nature* 397 (1999) 137.
- [Gil10] Woosik Gil et al., “The Cryogenic Pumping Section of the KATRIN Experiment”, *Applied Superconductivity, IEEE Transactions*, vol. 20, no. 3, pp. 316-319, 2010, DOI: 10.1109/TASC.2009.2038581.
- [Giu12] A. Giuliani, “Neutrino Physics with Low-Temperature Detectors”, *J. Low Temp. Phys.* (2012) 167: 991. doi:10.1007/s10909-012-0576-9.
- [Gla15] Irina Glasner. ‘Magnetfeldmessungen an der differentiellen Pumpstrecke am KATRIN-Experiment’, *Karlsruhe Institute of Technology*, master thesis, Nov. 2015.
- [Gro15] Stefan Groh, “Modeling of the response function and measurement of transmission properties of the KATRIN experiment”, *Karlsruhe Institute of Technology*, Ph.D. thesis, 2015.
- [Hac17] Motitz Hackenjos, “Commissioning and Modelling of the KATRIN Experimental Beam Line”, *Karlsruhe Institute of Technology*, Ph.D. thesis in preparation, 2017.
- [Har15] Fabian Harms, “Characterization and Minimization of Background Processes in the KATRIN Main Spectrometer”, *Karlsruhe Institute of Technology*, Ph.D. thesis, 2015.
- [HH31] Edwin Hubble and Milton L. Humason, “The Velocity-Distance Relation among Extra-Galactic Nuclae”, *Astrophysical Journal*, vol.74, pp. 43 - 80, 1931.
- [Hir88] K. S. Hirata et al., “Observation in the Kamiokande-II detector of the neutrino burst from supernova SN1987A”, *Phys. Rev. D*, vol. 38, p. 448, 1988, DOI: 10.1103/PhysRevD.38.448.
- [HLK13] Hinshaw, G., D. Larson, E. Komatsu et al., “Nine-year Wilkinson Microwave Anisotropy Probe (WMAP) observations: cosmological parameter results”, *Astrophysical Journal Supplement*, vol. 208(2), 2013.
- [Hoe12] Markus Hötzel, “Simulation and analysis of source-related effects for KATRIN”, *Karlsruhe Institute of Technology*, Ph.D. thesis, 2012.
- [Hug10] Karen Hugenberg, “An angular resolved pulsed UV LED photoelectron source for KATRIN”, *Progress in Particle and Nuclear Physics*, vol 64, no. 2, pp. 288 - 290, 2010, DOI: 10.1016/j.physrep.2007.02.002.
- [Jan07] Hans-Thomas Janka et al., “Theory of core-collapse supernovae”, *Physics Reports*, vol. 442, pp. 38 - 74, 2007, DOI: 10.1016/j.physrep.2007.02.002.
- [Jan15] Alexander Jansen, “The cryogenic pumping section of the KATRIN Experiment - Design studies and Experiments for the commissioning”, *Karlsruhe Institute of Technology*, Ph.D. thesis, 2015.
- [KL13] Stephen F. King, Christoph Luhn, “Neutrino Mass and Mixing with Discrete Symmetry”, *Report on Progress Physics*, vol. 76, no. 5, p. 056201, 2013, DOI: 10.1088/0034-4885/76/5/05620.

- [Kop07] Sacha E. Kopp, “Accelerator Neutrino Beams”, *Phys. Rept.*, vol. 439, pp. 101 - 159, 2007, DOI: 10.1016/0012-821X(69)90167-8.
- [KR83] P. Kruit and F. H. Read, “Magnetic field paralleliser for 2π electron-spectrometer and electron-image magnifier”, *Journal of Physics E: Scientific Instruments*, vol. 16, no. 4, p. 313, 1983, DOI: 10.1088/0022-3735/16/4/016.
- [Kra05] Christine Kraus et al., “Final results from phase II of the Mainz neutrino mass search in tritium β decay”, *The European Physical Journal C*, vol. 40, no. 4, pp. 447 - 468, 2005, DOI: 10.1140/epjc/s2005-02139-7.
- [Lid03] Andrew Liddle, “An Introduction to Modern Cosmology”, *Wiley*, 2003.
- [LL02] T. J. Loredo, D. Q. Lamb, “Bayesian analysis of neutrinos observed from supernova SN 1987A”, *Phys. Rev. D*, vol 65, p. 063002, 2002, DOI: 10.1103/PhysRevD.65.063002.
- [Lob85] V. M. Lobashev, “A method for measuring the electron antineutrino rest mass”, *Nucl. Instr. Meth. A*, vol. 240, no. 2, pp. 305 - 310, 1985. DOI: 10.1016/0168-9002(85)90640-0.
- [LP12] Julien Lesgourges and Sergio Pastor, “Neutrino Mass from Cosmology”, *Advances in High Energy Physics*, vo. 2012, no. 608515, 2012, DOI: 10.1155/2012/608515.
- [Luk12] Strahinja Lukić, Beate Bornschein, Lutz Bornschein, Guido Drexlin, Andreas Kosmider, Klaus Schlösser, Alexander Windberger, “Measurement of the gas-flow reduction factor of the KATRIN DPS2-F differential pumping section”, *Vacuum*, vol. 86, no. 8, pp. 1126 - 1133, 2012, DOI: 10.1016/j.vacuum.2012.10.017.
- [Lun24] Knut Lundmark, “The determination of the curvature of space-time in de Sitter’s world”, *Monthly Notices of the Royal Astronomy Society*, vol. 84, pp. 747 - 770, 1924.
- [Mau09] Detlef Maurel, “Designstudien zur Messung der Aktivität der Tritiumquelle im KATRIN-Experiment mit Röntgenstrahlung”, *Karlsruhe Institute of Technology*, diploma thesis, 2009.
- [MNS62] Ziro Maki, Masami Nakagawa, Shoichi Sakata, “Remarks on the Unified Model of Elementary Particles”, *Progress of Theoretical Physics*, vol. 28, no. 5, pp. 870 - 880, 1962, DOI: 10.1143/PTP.28.870.
- [Mue14] Axel Müller, “Field Alignment Studies at the KATRIN Pinch Magnet”, *Karlsruhe Institute of Technology*, bachelor thesis, 2014.
- [Nuc08] A. Nucciotti, “The MARE Project”, *J. of Low Temp. Phys.* (2008) 151: 597. doi:10.1007/s10909-008-9718-5.
- [Oli14] K.A. Olive et al. (Particle Data Group), “REVIEW OF PARTICLE PHYSICS”, *Chinese Physics C*, vol. 38, no. 9, p. 247, 2014, DOI: 10.1088/1674-1137/38/9/090001.
- [Osi01] Alexander Osipowicz, “KATRIN: A Next generation tritium beta decay experiment with sub-eV sensitivity for the electron neutrino mass. Letter of intent”, *KATRIN Collaboration*, p. 10, 2001, arXiv:hep-ex/0109033.
- [Pat16] C. Patrignani et al. (Particle Data Group), *Chin. Phys. C*, 40, 100001, 2016.
- [Pau30] Wolfgang Pauli, “Offener Brief an die Gruppe der Radioaktiven bei der Gauvereins-Tagung zu Tübingen”, 1930.
- [Per75] Martin L. Perl et al., “Evidence for Anomalous Lepton Production in $e^+ - e^-$ Annihilation”, *Phys. Rev. Lett.*, vol. 35, no. 22, pp. 1489 - 1492, 1975, DOI: 10.1103/PhysRevLett.35.1489.

- [Pic92] A. Picard et al., “A solenoid retarding spectrometer with high resolution and transmission for keV electrons”, *Nuclear Instruments and Methods in Physics Research Section B: Beam Interactions with Materials and Atoms*, vol. 63, pp. 345 - 358, 1992. DOI: 10.1016/0168-583X(92)95119-C.
- [Pon57a] Bruno Pontecorvo, “Inverse beta processes and nonconservation of lepton charge”, *Zh. Eksp. Teor. Fiz.*, vol. 34, p. 247, 1957.
- [Pon57b] Bruno Pontecorvo, “Mesonium and anti-mesonium”, *Zh. Eksp. Teor. Fiz.*, vol. 33, pp. 249 - 551, 1957.
- [Pon67] Bruno Pontecorvo, “Neutrino Experiments and the Problem of Conservation of Leptonic Charge”, *Zh. Eksp. Teor. Fiz.*, vol. 53, pp. 1717 - 1725, 1967.
- [Rei09] Stefan Reimer, “Ein elektrostatisches Dipolsystem zur Eliminierung von Ionen in der DPS2-F des KATRIN Experiments”, *Karlsruhe Institute of Technology*, diploma thesis, 2009.
- [Ren11] P. Renschler, “A new Monte Carlo simulation code for low-energy electron interactions in silicon detectors”, *Karlsruhe Institute of Technology*, Ph.D. thesis, 2011.
- [Roe11] Marco Roellig, Studien zu einem Röntgendetektorsystem zur Überwachung der KATRIN Tritiumquelle”, *Karlsruhe Institute of Technology*, diploma thesis, 2011.
- [Roe16] Carsten Röttele, ”Simulationen zu den Inbetriebnahmemessungen mit der kryogenen Pumpstrecke CPS des KATRIN Experiments”, *Karlsruhe Institute of Technology*, master thesis, 2016.
- [RP13] Marco Roellig and Florian Priester et al., “Activity monitoring of a gaseous tritium source by beta induced E-ray spectrometry”, *Fusion Engineering and Design*, vol. 88, no. 6 - 8, pp. 1263 - 1266, 2013, DOI: 10.1016/j.fusengdes.2012.11.001.
- [Sac15] Rudolf Sack, “Aufbau einer Ionenquelle und Simulation der Transporteigenschaften der DPS und CPS am KATRIN Experiment”, *Karlsruhe Institute of Technology*, master thesis, 2015.
- [Sch14] Johannes S. Schwarz, “The Detector System of the KATRIN Experiment - Implementation and First Measurements with the Spectrometer”, *Karlsruhe Institute of Technology*, Ph.D. thesis, 2014.
- [Sco35] F. A. Scott, “Energy Spectrum of the Beta-Rays of Radium E”, *Phys. Rev.*, vol. 48, no. 5, pp. 391 - 395, 1935, DOI: 10.1103/PhysRev.48.391.
- [Sis04] M. Sisti et al., “New limits from the Milano neutrino mass experiment with thermal microcalorimeters”, *Nucl. Inst. and Meth. A* 520 (2004) 125-131.
- [Sli15] Vesto Melvin Slipher, “Spectrographic Observations of Nebolae”, *Popular Astronomy*, vol. 23, pp. 21-24, 1915.
- [UDRL09] Ubieto-Díaz, M., D. Rodríguez, S. Lukic et al., “A broad-band FT-ICR Penning trap system for KATRIN”, *International Journal of Mass Spectrometry*, vol. 288, issues 1-3, pp. 1-5, Nov. 2009, DOI: <http://dx.doi.org/10.1016/j.ijms.2009.07.003>.
- [Val11] Kathrin Valerius et. al, “Prototype of an angular-selective photoelectron calibration source for the KATRIN experiment”, *Journal of Instrumentation*, vol. 6, p. P01002, 2011, DOI: 10.1088/1748-0221/6/01/P01002.
- [Wal13] B. L. Wall, “Karlsruhe Tritium Experiment: Detector System Comissioning an In-Situ PIN-Diode Array Dead-Layer Measurement”, *University of Washington*, Ph.D. thesis, 2013.

-
- [WJ05] Stan Woosley, Hans-Thomas Janka, “The physics of core-collapse supernovae”, *The physics of core-collapse supernovae*, vol. 1, pp. 147 - 154, 2005, DOI: 10.1038/nphys172.
- [Zac09] Michael Zacher, “Electromagnetic design and field emission studies for the inner electrode system of the KATRIN main spectrometer”, *Univ. Münster*, diploma thesis, 2009.
- [Zub11] Kai Zuber, “Neutrino Physics”, *CRC Press*, vol. 2, 2011.

Danksagung

Ich möchte zum Abschluss noch einigen Menschen danken, die mich bei meiner Arbeit begleitet und unterstützt haben. Ich danke

- Prof. Dr. Guido Drexlin der diese Arbeit ermöglicht hat,
- Prof. Dr. Ulrich Husemann, der sich freundlicherweise bereiterklärt hat, die Zweitkorrektur zu übernehmen,
- Dr. Fabian Harms dafür, dass er mir als Betreuer immer mit Rat und Tat zur Seite stand, mir bei fast allen Problemen helfen konnte und für das gründliche Korrekturlesen,
- Dr. Florian Fränkle, mit dem ich die Messungen mit zum Detector-Waver-Alignment durchgeführt habe,
- Hans-Werner Ortjohann für die Bedienung des FaroArms bei vielen Messungen,
- Axel Müller, der mit mir gemeinsam Messungen des Magnetfeldes des Pinch-Magneten durchgeführt hat,
- den unzählige Menschen, die bei Fragen zum Alignment und bei der Suche nach Zahlenwerten geholfen haben, darunter Klaus Müller, Steffen Lichter und Carsten Röttele,
- Dr. Ferenc Glück und Momin Ahmad, die sich mit mir ein Büro teilen mussten, für die gute Stimmung im Büro,
- Hendrik Seitz-Moskaliuk für die Leitung des DiDoBaMa-Seminars, sowie all denen, die uns dort mit Vorträgen zu den unterschiedlichsten Themen weiter gebildet oder unterhalten haben,
- allen Kollegen für die angenehme Arbeitsatmosphäre,
- meinen Großeltern Paul und Anna Lehmann, die mich die längste Zeit des Studiums bei sich aufgenommen und finanziell unterstützt haben, sowie
- meiner Freundin Anika Müller, für die moralische Unterstützung bei Hochs und Tiefs nicht nur im Studium und ihre grenzenlose Geduld!